8-2007

Wireless Passive Surface Acoustic Wave (SAW) Sensing System

Sridevi Krishnamurthy
Western Michigan University

WIRELESS PASSIVE SURFACE ACOUSTIC WAVE (SAW) SENSING SYSTEM

by

Sridevi Krishnamurthy

A Dissertation
Submitted to the
Faculty of The Graduate College
in partial fulfillment of the
requirements for the
Degree of Doctor of Philosophy
Department of Electrical and Computer Engineering
Dr. Massood Z. Atashbar, Advisor

Western Michigan University
Kalamazoo, Michigan
August 2007

WIRELESS PASSIVE SURFACE ACOUSTIC WAVE (SAW) SENSING SYSTEM

Sridevi Krishnamurthy, Ph.D.

Western Michigan University, 2007

Due to their small size and ruggedness, Surface Acoustic Wave (SAW) devices have been widely used as part of wireless sensing or identification system especially in inaccessible and inhospitable environments. In addition, SAW devices find widespread applications as filters in communication systems and also as physical, chemical and bio-sensors and ID tags. The passive wireless SAW sensing system mainly consists of a passive SAW sensor and an interrogation unit which sends a burst signal to the SAW sensor and processes the sensor response. The main objectives of this work were designing, prototyping and fabricating the interrogation unit on a PCB and also designing modeling, simulating and fabricating SAW devices. Significant results obtained from the burst transceiver and simulation as well as measurement results of SAW devices will be presented together with some of the challenges faced.

The interrogation unit is a burst transceiver operating in the Industrial, Scientific and Medical (ISM) band at 433 MHz. The prototype was built using connectorized modules and manufacturer demonstration boards. Once the prototype burst transceiver was tested for its functionality, a miniaturized version was designed and fabricated on a PCB. The PCB layout was prepared using FreePCB^{TM} software

and manufactured at Cirexx International, CA. Both the prototype and the PCB burst transceiver is characterized using a cascaded gain and noise figure analysis performed for both the transmit and the receive sections.

SAW delay lines and resonators operating at 100 MHz were first designed and then fabricated at the University of Michigan's Micro/Nano fabrication facility in Ann Arbor, MI. Simulation of the frequency response of SAW devices were performed in MATLAB™, PSpice Capture™ and CoventorWare™. The design aspects of SAW devices and details of modeling the SAW devices in each of the above software packages are presented. Simulation results obtained from all the three software packages are compared with measured responses and the relative merits and demerits of each method will be presented.

ACKNOWLEDGEMENTS

I would like to express my deepest appreciation and gratitude to my dissertation Committee Chair and advisor Dr. Massood Atashbar for his continuous guidance throughout my dissertation work and his constant support and encouragement. I would like to thank my advisor Dr. Bradley Bazuin for this invaluable guidance and persistent help every step of the way. I would like to thank Dr. John Gesink, ECE Chair for agreeing to be on my Committee and being kind enough to patiently read through my dissertation. Special thanks are due to Dr. Azim Houshyar for being on my Committee and reading through my dissertation. I would like to thank the Graduate College at Western Michigan University and the National Science Foundation for their financial support.

In addition, I would like to thank Mr. David Florida of the Department of Electrical and Computer Engineering and Mr. Glenn Hall of the Department of Mechanical and Aeronautical Engineering for providing technical support throughout the course of this dissertation work. I would also like express my gratitude to Ms. Janet Liebendorfer and Ms. Sheryl Todd for their assistance with all the associated paper work. Special thanks to Dr. Karlis Kaugars and the CAE staff for being kind enough to let me run simulations on their computers night after night.

I would like to thank my parents and sister for all the sacrifices they have made over the years in order to provide me the finest education possible. Without their support, this dissertation work would have been impossible. I also wish to thank my in-laws for their constant support and encouragement and for truly believing in me. I would like to thank my friend Mr. Srikanth Singamaneni for being a great source of inspiration and motivation throughout course of my dissertation. I would

also like to thank my dear friend Ms. Aarthi Sridharan for always being there and encouraging me in all my endeavours. Last but not least, this section would be incomplete without expressing my heartfelt thanks and appreciation to my husband for all the sacrifices that he has made and for constantly encouraging me. Without his support, I would not have been able to complete this dissertation work.

Sridevi Krishnamurthy

TABLE OF CONTENTS

Table of Contents-Continued

CHAPTER

Table of Contents-Continued

CHAPTER

Table of Contents-Continued

CHAPTER

LIST OF TABLES

LIST OF FIGURES

List of Figures-Continued

List of Figures-Continued

CHAPTER I

INTRODUCTION

1.1 Background

This section provides a brief historical background for SAW devices. Lord Rayleigh first discovered the existence of SAW in 1885[1]. The main feature of these devices that attracted interest was the propagation path since it can be used to generate, receive and change the characteristics of the wave[2]. They have been in use since the late 1960s and their initial applications were as pulse compression filters, bandpass filters, resonators, duplexers, oscillators, convolvers, and matched filters for spread spectrum[2]. SAW devices found much of interest due to the requirements in radar applications. Radar was established during World War II and it was shown that the range of radar can be improved by lengthening the radiated pulse for a constant power level. This was done using chirp pulses. SAW devices have been used in these applications where a chirp pulse was transmitted and received via a matched filter. These matched filters should delay the different frequencies of the chirp so that they all arrive at the receiver at the same time. Dispersive L-C circuits were bulky and hence SAW dispersive delay lines were considered. The delay line shown in Figure 1.1 was used for this purpose. It consists of transducers fabricated on both faces of a quartz crystal block such that the high frequency waves are strongest near the surface with shorter propagation path and lower loss, whereas the low frequency waves are generated away from the surface. Thus different frequencies have different delays[3]. In 1963, Rowen and Mortley proposed the use of planar surfaces for defining transducers so that surface waves can be generated instead of bulk waves[4, 5]. The first engineering application of SAW devices on planar substrates was introduced by White and Voltmer in 1965[6]. White experimentally showed

that SAW can be generated and detected by placing Interdigital Transducers (IDTs) on a piezoelectric substrate. The IDT consisted of metal electrodes and the alternate electrodes were connected to the same busbar (see Figure 1.2)[6]. In 1969, Tancrell et al. obtained results from a dispersive transducer on $LiNbO_3$ substrate[7] and also suggested varying overlap of the IDT fingers, which is known as apodization, to reduce the side lobe levels in the frequency response of these devices. The first pulse compression filters were developed in 1969 by Tancrell et al., and research on these devices continued in the 1970s. Double electrode transducers were used instead of single electrode transducers to minimize the reflections from the electrodes and hence minimize distortion[2]. Also in 1969, it was proved that apodization could be used to alter the frequency response of SAW devices, allowing these devices to be used as bandpass filters[2]. If the required frequency response is translated to time domain, this can be used to determine the weight of the IDT fingers[8, 9]. Bandpass filters used in TV normally use Multi-Strip Couplers (MSC) on YZ-$LiNbO_3$ to minimize bulk wave interference[10, 11]. To reduce the device area, later 128° YX-$LiNbO_3$ was sometimes used. This minimized bulk wave excitation and hence eliminated the need for an MSC[2]. Also, Hartmann demonstrated withdrawal weighting which can be used instead of apodization[12]. In withdrawal weighting, selected electrodes were removed from the IDT, which gave better device responses.

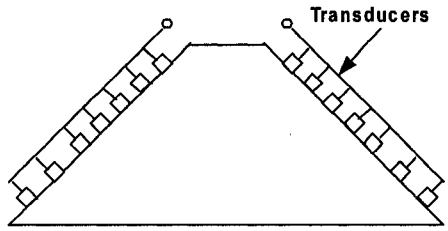

Figure 1.1: SAW delay line

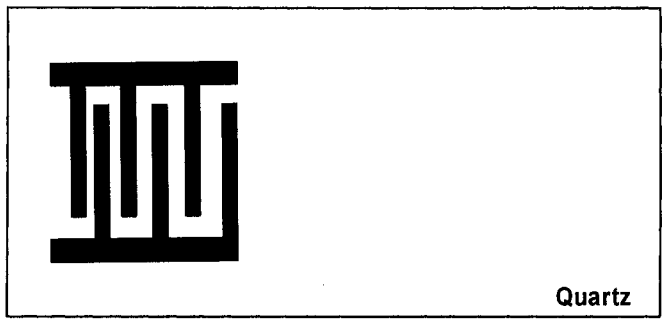

Figure 1.2: SAW IDT

In the 1970s, SAW resonators were used which consisted of reflectors to get better reflectivity. A great deal of research was done to study the effect of gratings and transducer positions on the velocity shifts. The effects of grooves or electrodes on velocity were also investigated[2]. In 1969, Maines et al. produced the first SAW oscillator using a delay line with an amplifier as the feedback element[13]. Staples et al. first described one-port and two-port resonators in 1974[14]. In addition to delay lines, resonators were also used as the controlling element in SAW oscillators. In 1971, Luukkala and Kino proposed the use of SAW devices as convolvers (Figure 1.3)[15]. In this structure, the SAW that is generated by the two input IDTs overlap in the center and produce an output wave at the uniform electrode placed in the center. The output waveform thus obtained is the convolution of the two input waveforms[2].

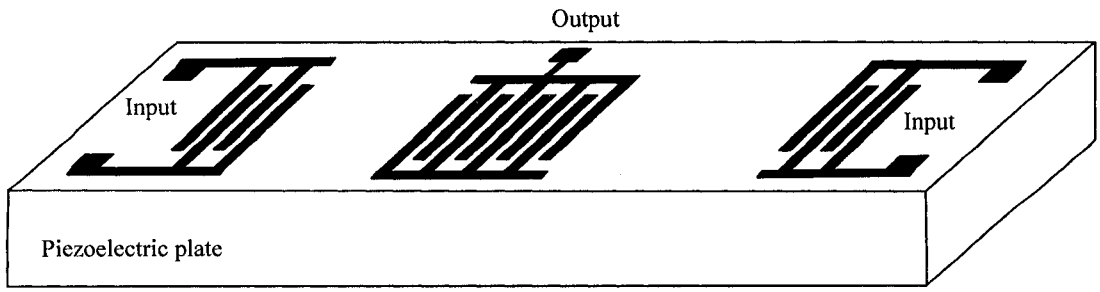

Figure 1.3: SAW convolver

Different techniques were developed to analyze SAW transducers during 1965-1985. The Delta function model, proposed by Tancrell and Holland, assumed a localized source was present at each edge of the electrode[16]. The limitation of this method was that the transducer impedance cannot be obtained hence the insertion loss cannot be estimated[16]. To overcome this disadvantage, Smith et al. developed the equivalent circuit model in 1969[17]. Since equivalent circuits of bulk wave transducers were known, the IDT were simulated as an array of these bulk wave transducers[17]. In addition to the different types of devices, different models were used to analyze the behavior of these devices. The Coupling of Modes (COM) theory is one of the techniques used for this purpose. This method uses coupled differential equations to represent the forward and backward traveling waves. Using this method, expressions can be obtained for scattering properties of uniform transducers such as transduction, reflection and admittance[18]. This method has been successfully used earlier to simulate the frequency response of SAW devices[19]. Also, Green's functions were used to analyze the propagation of the different acoustic waves in different structures. It also allows analysis of devices with up to a few hundred electrodes[20, 21]. Basically, Green's function gives the voltage due to a line source of charge parallel to the length of the electrodes. Once the Green's function is determined, the power carried by the surface acoustic waves in the positive and negative directions, and the power associated with the bulk waves can be determined at both the input and the output transducers[20].

1.2 Motivation

Sensors are widely used in numerous industrial applications and in our day-to-day activities. Sensors provide us with real-time information that helps us make important decisions in various industrial disciplines. Sensors and sensor systems make electronic control of today's technical systems easier. Sensors can make industrial processes and

applications more cost effective, reliable, and safe[22]. Sensors play a key role in consumer electronics and communication systems because of their reliability and versatility. In many industrial applications, the sensor and data collection and processing must be distributed and placed in inhospitable or inaccessible environments. Distributed measurement and control capability is a primary goal for military and civil transportation, manufacturing, biomedical, environmental management, safety and security systems and many other industrial processes and applications[23]. The need for small and reliable sensors capable of monitoring multiple environmental, physical, chemical and biological parameters is on the rise[24]. The development of smart sensors can be very useful to the energy industries, the military and other industrial organizations[25, 26]. To facilitate sensing in such inhospitable or inaccessible environments, the sensor system must be self-contained and preferably accessed using wireless communication techniques. Designing reliable, cost effective, and small sized wireless sensors poses significant challenges to the scientific community. Advanced concepts and techniques exist that can address this challenge.

A new generation of micro sensors based on SAW technologies promise to provide measurements of a wide range of physical and chemical parameters, including temperature, pressure, gas concentrations, etc using wireless communications. SAW devices were discovered many years ago, and since then researchers have investigated their properties and applications. Due to their compact size and integrated circuit (IC) compatibility, SAW devices are used in various analog and digital communication and sensing applications[27]. Thus, we have seen the commercial use of acoustic wave devices for many decades[28]. The basic principle of the SAW sensor is based on the changes in propagation of a wave along the sensor surface. The main advantage of using SAW devices as sensors is that the velocity of these waves is five orders of magnitude smaller than the velocity of electromagnetic waves. Therefore, SAW sensors are much smaller in size when compared to their electromagnetic counterpart. Due to their lower velocity, the

propagation path can be used as the active sensing area to expose the sensor to the measurand. The substrate is piezoelectric such as quartz, $LiNbO_3$, $LiTaO_3$ and $La_3Ga_5SiO_{14}$. When a voltage waveform is imposed on a transducer, a surface wave is propagated on and within SAW devices. The resulting waveform has been modified based on the physical property chosen to be measured, and this change in waveform can be used to quantify the measurand, thereby providing a useful measurement. The small size, flexible measurement capability and mass producibility of SAW devices provides a tremendous incentive for developing a range of small, low-power sensors for a broad range of applications. In addition to their application as sensors these devices are also used as filters, duplexers and oscillators.

The main objective of this work was to perform a comprehensive study of the passive wireless SAW sensing system consisting of the interrogation unit and the SAW sensor. A great deal of research is being conducted on the modeling and simulation of SAW devices for use as sensors. This work presents a comparison between transmission matrix approach using MATLAB™, equivalent circuit approach using PSpice Capture™ and finite element modeling and analysis using CoventorWare™ stating the relative merits and demerits of each method. It also provides a comparison between simulated and measured SAW device responses obtained from fabricated SAW devices. The architecture of the interrogation unit which is a burst transceiver is discussed together with significant results obtained from the burst transceiver fabricated on a PCB.

1.3 Author's contributions

The present work has led to several publications including 3 book chapters, 2 journal papers, and 7 conference presentations as given in the List of Publications in Appendix D. In addition, another manuscript has been accepted for presentation at the IEEE Sensors 2007 Conference to be held in Atlanta, GA.

1.4 Organization of the dissertation

The rest of this dissertation is divided into six chapters. Chapter 2 provides an introduction to SAW sensors. Chapter 3 discusses the architecture of the burst transceiver and the results obtained. Chapter 4 presents a detailed description of the design, modeling and simulation of SAW devices using MATLAB™, PSpice Capture™ and CoventorWare™. Chapter 5 discusses the fabrication and measurement results obtained from SAW devices and also provides a comparison with simulated responses. Chapter 6 presents results obtained from a passive wireless SAW sensing system. Chapter 7 deals with conclusions for this work and also suggestions for future work.

CHAPTER II

INTRODUCTION TO SURFACE ACOUSTIC WAVE (SAW) SENSORS

2.1 Introduction

The main application of Surface acoustic wave (SAW) devices is as sensors as part of a wireless passive sensing system. The schematic of the wireless passive SAW sensing system is shown in Figure 2.1. It consists of an interrogation unit, radio link and the SAW sensor. The interrogation unit sends a burst signal to the SAW sensor and the response from the sensor is processed in the interrogation unit to obtain information about the parameter being sensed. SAW devices are discussed in detail in this chapter. The details of the interrogation unit will be described at length in chapter 3.

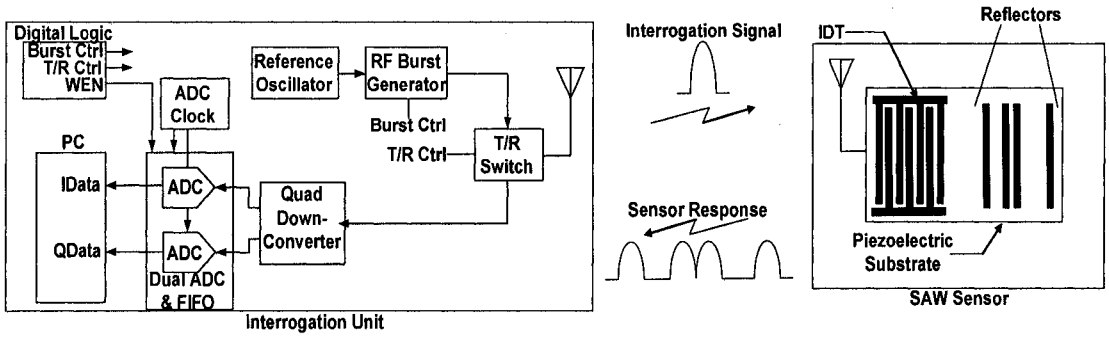

Figure 2.1: Schematic of a passive wireless SAW sensing system

Surface acoustic waves (SAW) are generated on the surface of a piezoelectric substrate when an electrical signal is applied to the Inter-digital Transducer (IDT) deposited on the surface. The thickness of the piezoelectric material and the substrate orientation determine the type of acoustic wave and the wave velocity. The piezoelectric substrates that are commonly used are Quartz, $LiNbO_3$, $LiTaO_3$ and Langasite ($La_3Ga_5SiO_{14}$). One of the parameters used in the selection of the particular piezoelectric

substrate is the electromechanical coupling coefficient (K^2). This is a measure of how effectively a given piezoelectric substrate can convert an applied electric signal into an acoustic wave and vice versa[29]. These values are normally specified as percentages. K^2 can be expressed either in terms of piezoelectric parameters as $K^2=e^2/\varepsilon c$, or can be determined experimentally using the relation[29]

$$K^2 = \frac{-2\Delta v}{v_o} \qquad \textbf{Equation 2-1}$$

In the above equations, e is the piezoelectric coefficient, c is the elastic constant, ε is the dielectric permittivity, Δv is the change in SAW velocity when the surface of the piezoelectric substrate is shorted by a thin conducting metal film and v is the SAW velocity in the absence of the conducting film[29]. Another important parameter characterizing a piezoelectric substrate is the Temperature Coefficient of Delay (TCD). This parameter denotes the stability of the SAW device against changes in temperature and is given by[29]

$$\alpha_T = \frac{1}{\tau}\frac{d\tau}{T} = \frac{1}{L}\frac{dL}{dT} - \frac{1}{v_o}\frac{dv}{dT} \qquad \textbf{Equation 2-2}$$

where τ is the acoustic wave propagation time over a distance L on a piezoelectric substrate and v_o is the SAW velocity. The first term in the above equation gives the effect of thermal expansion, and the second term shows the effect of change in velocity as a result of change in temperature. For a SAW device to be stable with respect to changes in temperature, α_T must be as small as possible[29]. Quartz is the most temperature stable substrate. However, $LiNbO_3$ is used when higher electromechanical coupling coefficients are required.

SAW devices usually consist of IDTs deposited on the surface of a piezoelectric surface as shown in Figure 2.2. The IDTs consists of finger pairs with alternate fingers connected to the same comb. These fingers are normally made of Au/Cr or Al. In the

case of Au/Cr, Cr serves as an adhesive and Au is used since it is inert compared to most metals. Al has good adhesion with the substrate and therefore an adhesive layer like Cr is not required for Al electrodes. The device configuration in Figure 2.2 is commonly known as SAW delay line since it creates a delay equal to the propagation time of the SAW between the input and output IDTs. When a voltage is applied to the IDT, due to the piezoelectricity of the substrate, surface acoustic waves are generated that travel in both the directions away form the IDT. The wave propagates along the x-direction and particle displacements are in both x- and y- directions giving rise to an elliptical motion. These waves propagate along the surface and 90% of the energy of these waves is concentrated to within one wavelength depth of the substrate. The wave is thus not uniform in the y direction. Since only half of the acoustic energy is converted into useful electrical energy, the minimum loss of this device is 6 dB. Some of the second order effects that occur in SAW devices contribute to additional losses and therefore the loss of a typical SAW device is around 15-30 dB. Sometimes, Single Phase Unidirectional Transducers (SPUDT) are used instead of the bidirectional IDTs to minimize the loss of these devices. SPUDTs have reflectors placed in between the IDT fingers, which redirect the acoustic energy back into the device. The loss of a SAW device with SPUDT is around 5-12 dB since the second order effects still prevail. Some of these second order effects are presented in the following paragraph.

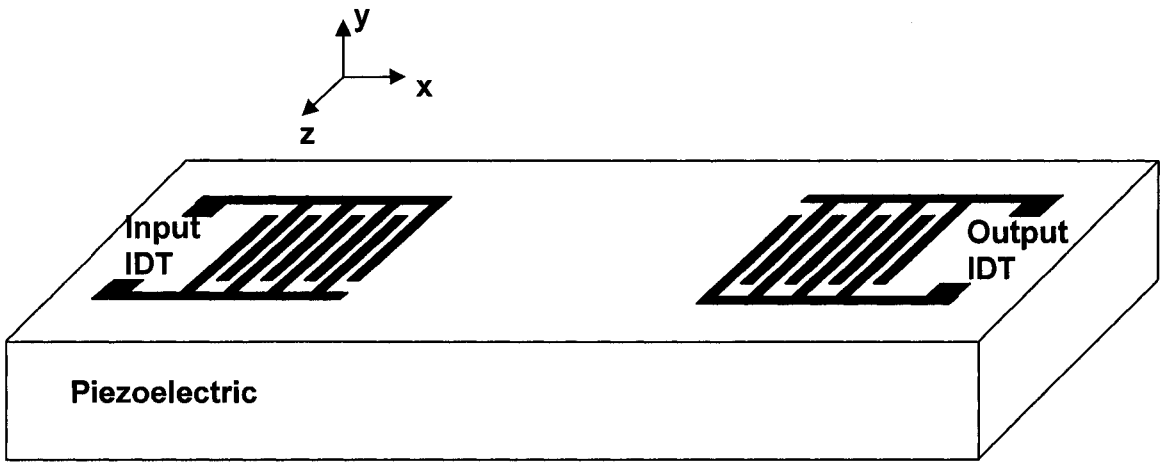

Figure 2.2: SAW device with IDTs defined on a piezoelectric substrate

Electromagnetic feed through causes direct coupling of the signal from the input to the output IDTs. Since the two IDTs act as a capacitor, the amount of feed through increases at higher frequencies giving rise to ripples in the amplitude and phase response of these devices. Careful packaging of structure and placing ground strips between the input and the output IDTs can reduce electromagnetic feed through[29]. Triple Transit Interference resulting from multiple reflections which give rise to additional voltages at the output IDT also creates ripples in the response of the filter. This can be reduced using SPUDTs or Split finger transducers which launch the acoustic waves in a single direction thus eliminating the bidirectional loss [30, 31, 32]. In addition to the above non linear effects, the IDT also generates bulk waves when excited. These bulk waves also reach the output IDT and interfere with the surface waves affecting the performance of acoustic wave devices. Detailed discussions of the effects of bulk waves in surface acoustic wave devices together with some methods that can be used to eliminate the bulk wave effects can be found in Mitchell[33]. Some of the techniques used to mitigate bulk wave effects include using very thin piezoelectric substrates, adhesive materials placed at the bottom to absorb the bulk waves, Multi-Strip Couplers (MSC) and roughening substrate bottoms to scatter the bulk waves. MSCs redirect the bulk waves and surface waves in different

directions so that only the surface waves reach the output IDT[34]. The IDTs also generate harmonic frequencies in addition to the fundamental, and the relative amplitudes depend upon the width of the IDT fingers with respect to their separation, as well as the geometry of the IDT. This may lead to additional harmonic signals interfering with the main signal[35, 36, 37]. Harmonic modes generated depend on the IDT geometry as well as the metallization ratio. Using the harmonic frequencies can be advantageous in the sense that the propagating bulk waves will not affect the passband response. Also, operating in the harmonic modes helps us to obtain higher frequency ranges which will otherwise be impossible due to lithographic resolution limitations. Proper care should be taken to reduce the second order effects while designing a SAW device depending on the application requirements. In the following section, we will take a brief look at the commonly used configurations of SAW Devices.

2.2 SAW device configurations

2.2.1 SAW delay line

In a delay-line, the SAW launched by the applied electrical signal at the input IDT travels towards the output IDT and is converted back to electrical signal at the output port. Figure 2.2 shows a SAW delay line. The delay time, τ, can be calculated using the relation $\tau=L/v_o$, where L is the distance between the input and output IDTs and v_o is the SAW velocity. The space in between the adjacent fingers is maintained at a quarter wavelength so the acoustic waves generated by the adjacent finger pairs add in phase. The important design parameters of the delay line are number of finger pairs in the IDTs, acoustic aperture, IDT center-to-center distance and transducer periodicity. In designing a delay line for a specific application, the frequency response that is required is first converted to impulse response, which is then used to determine the relative weights of the IDT fingers[38]. Delay lines normally have a sinc frequency response. IDT fingers are

sometimes apodized to suppress the sidelobe levels in the response of the delay line. Thus, the finger width, spacing between the fingers, and the acoustic aperture determine the frequency response of the delay line. Another configuration of a delay line is the reflective delay line where the SAW propagating from the IDT is reflected by each of the reflectors back to the originating IDT, thereby achieving the same delay as the delay line at half the chip size (Figure 2.3). Reflective delay lines are commonly used for SAW ID-tags and in passive wireless SAW sensing systems[39].

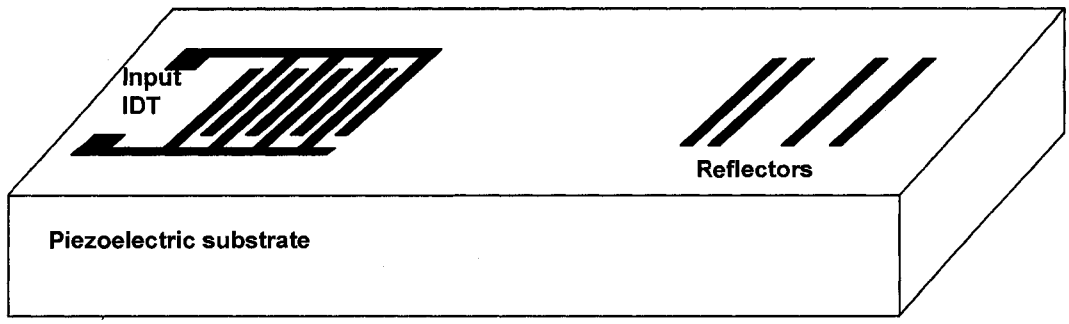

Figure 2.3: Reflective SAW delay line

2.2.2 One-port SAW resonator

A one-port resonator consists of one IDT with reflective gratings on either side. Figure 2.4 shows the schematic diagram of the one-port SAW Resonator.

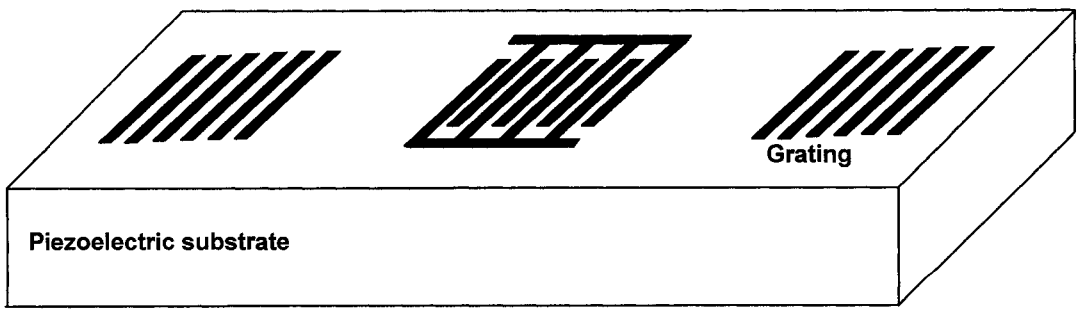

Figure 2.4: One-port SAW resonator

The SAW resonator is similar to the crystal resonators except that only one of the surfaces has the acoustic energy. The resonant cavity is confined to the region between the reflector gratings placed on either side of the IDT. Since SAW devices are inherently small and rugged due to their reduced speed in comparison to the electromagnetic wave, these devices can be used at high frequencies. The highest allowable frequency is limited to the minimum line widths attainable with today's microfabrication facilities. The Quality factor, Q, of the SAW resonator depends on the various types of losses in the resonator including damping loss as well as loss due to energy radiated into the air near the surface of the substrate[40]. The loss due to radiation of energy into air can be minimized by placing the resonator in an evacuated package. Thus the Q now only depends on the propagation loss. This Q is sometimes referred to as material Q or Q_m. Resonators can be used as frequency control elements in oscillators, as sensors, and also as filters in communication systems[41]. The following parameters should be considered while designing a SAW one-port resonator: number of finger pairs in the IDT, acoustic aperture, effective cavity length, number of reflectors in the grating, transducer periodicity, and reflector spacing.

2.2.3 Two-port SAW resonator

A two-port resonator works in the same way as the one-port resonator except that there are separate input and output IDTs. Figure 2.5 shows the schematic diagram of a two-port SAW resonator. Without the reflector gratings, the response of the device will be the same as that of two IDTs in cascade. But in the presence of reflector gratings, the frequency response of the resonator around the center frequency will be superimposed on the response of the IDTs[29]. Thus, the frequency response of the two port resonator is the same sinc response of the delay line except that there is an additional resonant peak at the IDT center frequency. The parameters that influence the response of two-port resonators are the number of IDT fingers, the separation between the grating and the IDT, the

grating reflectivity, the metallization height, and the substrate properties[29].

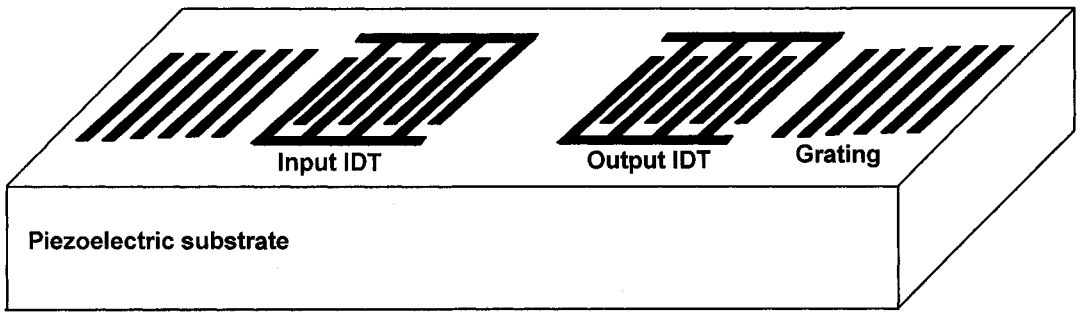

Figure 2.5: Schematic diagram of a two-port SAW resonator

2.3 Acoustic wave sensors

Acoustic wave based sensors include devices such as the Thickness Shear Mode (TSM), SAW, the Shear Horizontal Surface Acoustic Wave (SH-SAW), the Shear Horizontal Acoustic Plate Mode (SH-APM), the Flexural Plate Wave (FPW) or Lamb wave and the Love wave mode. These devices are based on various acoustic wave propagation modes, determined by the substrate material, the crystal cut, and the direction of particle displacement relative to the direction of wave propagation and the sensing surface. The electrode structure used to facilitate the acoustic wave propagation is also an important factor. The waves may travel through the bulk of the substrate material, be guided by one surface as a surface wave, or be guided by reflections from multiple surfaces[42]. Depending on the type of acoustic wave, they can be used in liquid or gaseous media or both. The sensing mechanism is classified based on the parameter that influences the propagation characteristics of the acoustic wave. A comparative study of the different type of acoustic wave sensors is briefly reviewed in this section, together with different sensing applications for each device. A summary of the sensing mechanisms common to the family of acoustic wave devices is presented next.

2.3.1 Thickness shear mode based sensor

The acoustic waves in TSM devices are bulk transverse waves that travel parallel to the depth of the piezoelectric substrate. Most TSM devices are fabricated on quartz wafers and are commonly known as quartz crystal microbalances (QCMs). These devices were the first piezoelectric devices used in sensing and detection applications. Figure 2.6 illustrates the QCM structure, which consists of a thin vibrating quartz wafer, located between two metal electrodes.

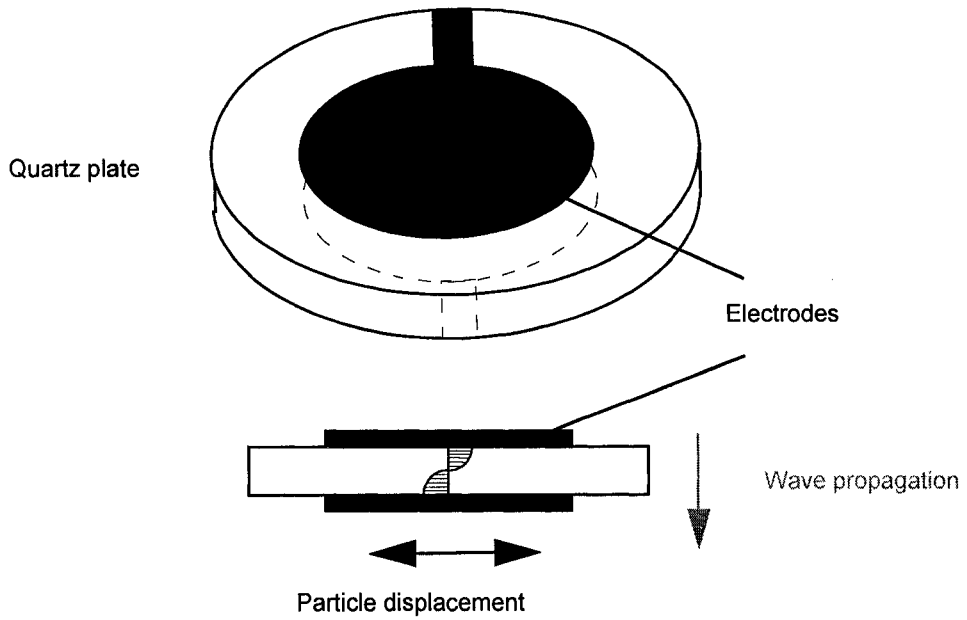

Figure 2.6: QCM device structure

The particle displacements are parallel to the surface. The wafer thickness d determines the wavelengths λ of the fundamental resonance and its harmonics. The fundamental resonance frequency is $f_o=v/2d$, where v is bulk acoustic wave velocity. Therefore, as the plate thickness decreases, the frequency increases. Typical resonant frequencies of the fundamental mode are between 5 and 20 MHz. Any material that comes into contact with the Quartz surface perturbs the resonant frequency of the Quartz crystal. If the mass adsorbed on the surface is negligible compared to the mass of the

crystal and is evenly distributed on the surface, the frequency of the crystal decreases proportionally. The change in the resonant frequency of the crystal with changing mass is given by the Sauerbrey equation as[43]

$$\Delta f = \frac{-2 f_o^2 \Delta m}{A\sqrt{\rho_q \mu_q}} \qquad \textbf{Equation 2-3}$$

where f_o is the fundamental resonant frequency, A is the piezoelectrically active area defined by the two gold electrodes, ρ_q is the density of the quartz (2.648 g/cm^3) and μ_q is the shear modulus (2.947×10^{11} dyn/cm^2).

QCM sensing applications in the gas phase include thickness monitoring in metal evaporation and selective film coated chemical sensors. Applications of QCM sensor arrays for the quantification of various gases and odors have also been reported. Some more recent applications have focused on the development of taste sensors and electronic noses[44, 45, 46]. Recent developments in QCM technology have led to their application in liquid environment. Some excellent reports presenting advanced oscillator circuitry and modelling of the QCM/liquid interface[47, 48, 49, 50, 51, 52, 53, 54, 55] have led to their application in biosensing[56, 57, 58, 59, 60, 61, 62].

2.3.2 Rayleigh mode SAW based sensor

Most of the acoustic wave devices use IDTs to launch the acoustic wave as well as to convert it back to electrical signal (see Figure 2.7). Rayleigh mode SAW based sensors have two predominant components of particle displacement, one of which is parallel to the direction of wave propagation and the other normal to the sensing surface. Therefore, the particles in Rayleigh mode SAW devices travel in elliptical paths. Most of the energy of the Rayleigh waves is confined within a few wavelengths depth of the substrate. The velocity of these devices is determined by the piezoelectric substrate used and the specific orientation. The periodicity of the IDT fingers determines the frequency of operation of the devices. Rayleigh wave devices cannot be used in liquid media since

the Rayleigh wave is attenuated in liquids[63]. So the application of these devices is restricted to gaseous media.

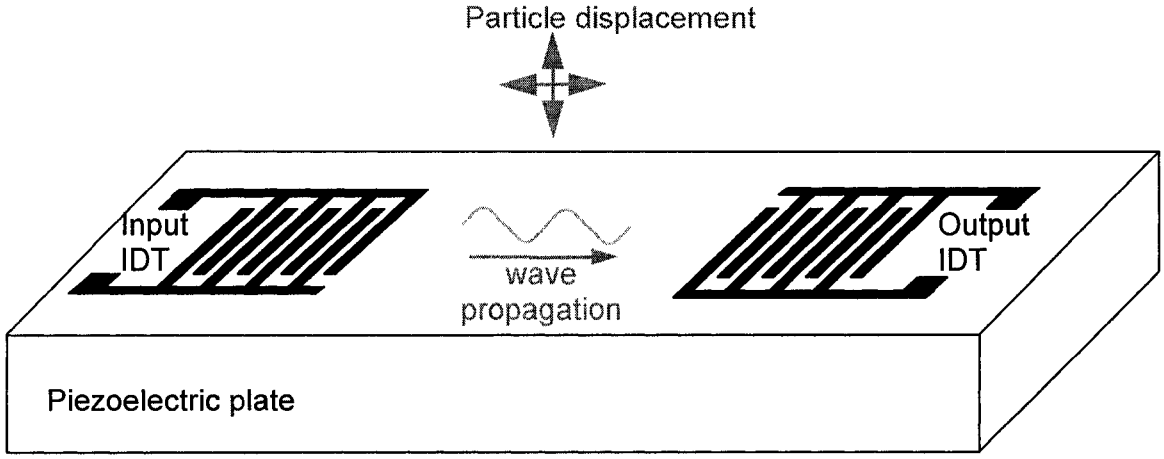

Figure 2.7: Rayleigh mode SAW delay line device structure

Some excellent papers describing the application of SAW sensors for the measurement of parameters such as temperature, pressure, electrical conductivity, mass and visco-elastic changes of thin films have been reported in a number of reviews[42, 64, 65, 66, 67, 68, 69, 70].

2.3.3 Shear horizontal SAW based sensor

SH-SAW devices are very similar to Rayleigh Wave devices in configuration, but the particle displacements in this case are parallel to the sensing surface and normal to the wave propagation direction. The surface normal component of the Rayleigh wave is not present in this case. The main reason for this difference in wave propagation characteristics when compared to the Rayleigh wave is the orientation of the piezoelectric crystal (Figure 2.8)[42]. In SH-SAW device, a thin solid film (called Love Wave Devices) or grating (called Surface Transverse Wave (STW) Devices) is sometimes added to prevent wave diffraction into the bulk. The frequency of operation is determined by the IDT finger spacing and the substrate orientation. An example piezoelectric substrate is

36° rotated Y-cut, X propagating lithium tantalate ($LiTaO_3$). The acoustic wave propagation is not severely attenuated when the surface is loaded with a liquid and hence these sensors can be operated in liquid media[71, 72, 73]. For measurements such as viscosity, electrical properties, and mass loading of an adjacent liquid a sensing function is achieved through the perturbation of the SH-SAW.

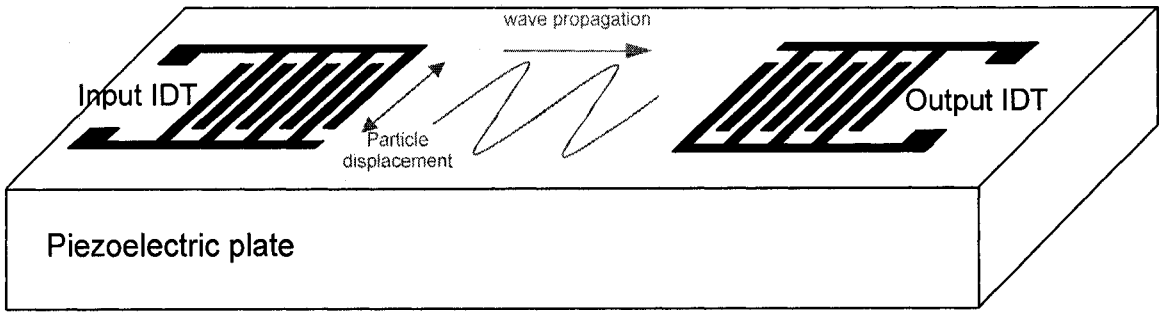

Figure 2.8: SH-SAW device structure

2.3.4 Shear horizontal acoustic plate mode based sensor

SH-APM devices also have a similar configuration to the Rayleigh SAW devices, but the wafer is thinner, typically a few acoustic wavelengths (Figure 2.9). The IDTs generate shear horizontal waves that propagate into the bulk of the device at certain angles to the surface. The corresponding particle displacement of the waves is transverse to the wave propagation direction. These waves reach the output IDT after a series of reflections at the ends of the plate. The superposition of these waves gives rise to a series of modes each having a different velocity. Rayleigh waves are also generated, but typically propagate at much lower velocities than those of the SH-APM modes. The frequency of operation is determined by the material properties, the thickness to wavelength ratio of the substrate, and the IDT finger spacing.

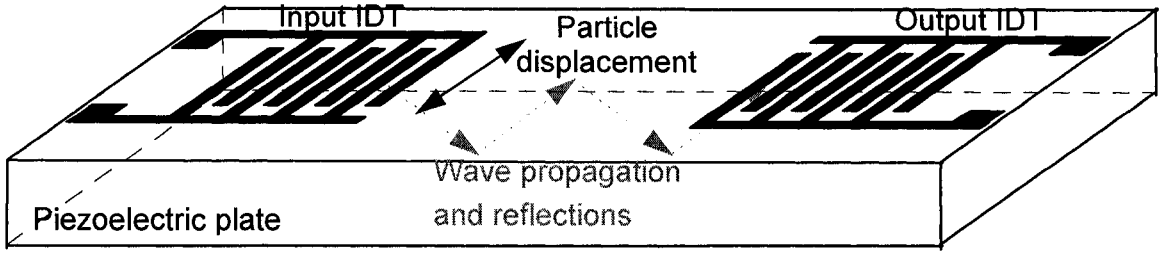

Figure 2.9: SH-APM device structure

Fabrication of APM devices requires additional design procedures for the fabrication of the thin plates with respect to the IDT periodicity. For this purpose, bulk piezoelectric materials are used, which can be either Quartz[74, 75] or $LiNbO_3$ sliced in thin plates[76]. Most of the SH-APM devices are based on this design because of the ability to choose the appropriate crystallographic orientation for the generation of the shear waves. According to the restrictions of the fabrication process, the minimum thickness is limited.

SH-APM devices are mainly used in liquid sensing and offer the advantage of using the back surface of the plate as the active sensing area. Consequently, the IDTs can be isolated from the liquid media, thereby preventing a direct chemical attack on the IDTs. The interfaces where the wave interacts with liquid and air should be polished and smooth since any irregularities will produce additional noise signals[77]. Considerable attention has been paid in developing different sensing applications by many groups. Applications such as viscosity measurement[75, 78, 79, 80], liquid identification via the electrical surface perturbation[76, 81, 82] and biosensing[83, 84, 85, 86] have been reported. Interesting applications for the APM sensor concerns the investigation of aqueous mercury for pollution monitoring of water[87] and for the on-line detection of organic pollutants in water[88].

2.3.5 Lamb wave based sensor

Lamb wave devices, or Flexural Plate wave (FPW) devices, have acoustic waves

that propagate along thin membranes of a piezoelectric material (Figure 2.10). These waves are similar to Rayleigh waves with surface parallel and surface normal components. The surface normal component is transverse to the wave propagation direction. Similar to the SH-APM device, the frequency of operation of the FPW device is determined by the material properties, ratio of the thickness of the plate to the wavelength, and the IDT finger spacing. Thickness of the piezoelectric membranes are typically less than one acoustic wavelength and their development has been achieved by means of micromachining technology based on IC-process, piezoelectric thin film deposition and silicon etching[89]. Although Flexural Plate Waves have a surface normal component, the wave velocity is slower than the compressional velocity of sound in liquids and hence they are not attenuated in liquid media. Therefore, FPW sensors find application in both liquid and gaseous media[42, 90].

These devices find applications as chemical gas sensors[91, 92], pressure sensors[93, 94, 95] and for the determination of liquid properties[89, 96]. Development of a FPW based biosensor has also been investigated[97, 98].

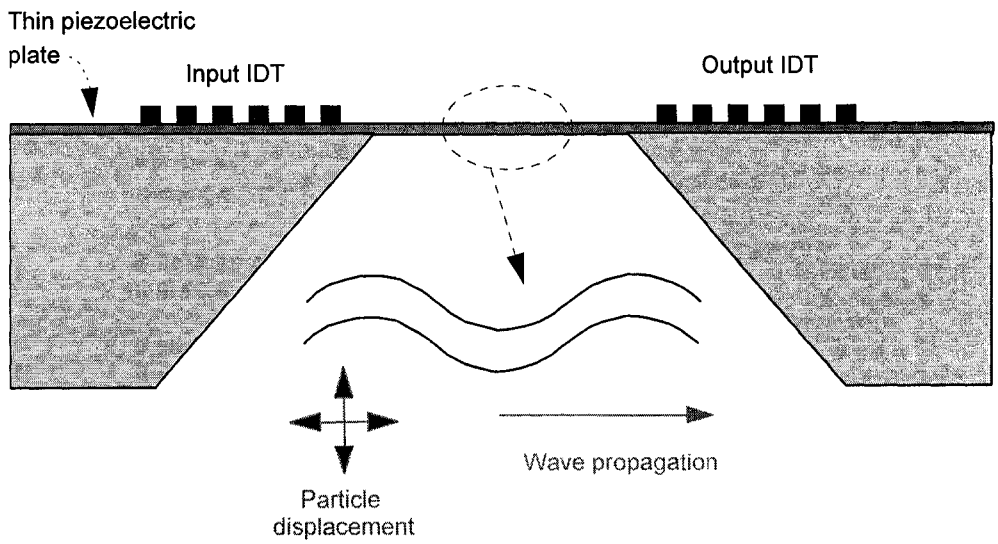

Figure 2.10: Lamb wave mode device structure

2.3.6 Love wave based sensor

Love wave devices are characterized by acoustic waves that propagate in a layered structure consisting of a piezoelectric substrate and a guiding layer (Figure 2.11) [99, 100, 101, 102]. They have a pure shear polarization with the particle displacements being perpendicular to the normal of the surface plane. A guiding layer confines and guides the wave over the top layer of the device. A Love wave can only exist if the shear velocity in the layer is less than the shear velocity in the substrate[103]. This results in slowing down the acoustic wave in the substrate, thus confining the acoustic wave energy to the surface layer. The particle velocity at the sensor surface is thus very high due to this energy concentration in the guiding layer. Also, the deposition process for the guiding layer should be such that a fairly uniform film with constant density over the entire thickness can be obtained. The mass sensitivity of the device is mainly determined by the thickness of the guiding layer (normalized to the acoustic wavelength). For increased layer thicknesses, wave guiding becomes more efficient, causing the mass sensitivity to increase. The sensing area in these devices is the same as the surface of the device. Applications have been predominantly reported for biosensor development[104, 105], due to the devices' high mass sensitivity in liquid media[106, 107].

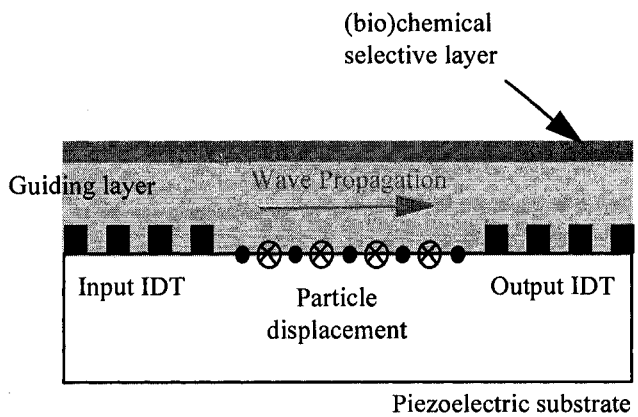

Figure 2.11: Love wave mode device structure

2.4 Summary of sensing mechanisms

The basic principle underlying acoustic wave sensors is the perturbation of the acoustic wave propagation characteristics by the measurand. This perturbation can be measured as a shift in the center frequency of the device or a change in the insertion loss. The various factors that can perturb the acoustic wave propagation characteristics namely mass (m), stiffness (c), conductivity (σ), dielectric coefficient (ε), temperature (T), pressure (p) is described by the following equation[108]

$$\frac{\Delta v}{v_o} = \frac{1}{v_o}\left(\frac{\partial v}{\partial m}\Delta m + \frac{\partial v}{\partial c}\Delta c + \frac{\partial v}{\partial \sigma}\Delta \sigma + \frac{\partial v}{\partial \varepsilon}\Delta \varepsilon + \frac{\partial v}{\partial T}\Delta T + \frac{\partial v}{\partial p}\Delta p + \ldots\right) \qquad \textbf{Equation 2-4}$$

Since a change in the velocity can be caused due to any of the above effects, it is important to take into account the sensitivity to other parameters. Compensation for overlapping sensitivities is normally achieved using differential configuration where only one of the two devices are used as sensor and the other as reference.

The use of an array of sensors for the analysis of multi-component measurands is therefore essential for gaining a better understanding of the sensing mechanisms[109, 110, 111]. Early investigations by groups including D'Amico and Verona[68], Ballantine and Wohltjen[65] and Grate et al.[111], reported that through the use of an array of sensors, together with the careful selection of the type of sensor system implemented (according to the working environment), the selectivity, sensitivity, and reproducibility of the overall sensing system may be enhanced. Pattern recognition techniques are commonly used to enhance the information extraction of the sensor array through intelligent data processing[111, 112, 113, 114, 115, 116]. Detailed discussions of the SAW sensor structures and the results obtained for parameters like temperature, pressure, mass loading, viscoelasticity and conductivity is given in Hoummady et al[117]. In this section, a brief introduction to the different acoustic wave sensing mechanisms will be provided. The most common

parameters that are sensed using acoustic wave devices are discussed in further detail in the following paragraphs.

2.4.1 Temperature

Temperature can change the velocity of the acoustic wave either by changing the mechanical properties of the substrate or by influencing dimensional changes in the substrate. In cases where temperature effects interfere with useful measurements while sensing other parameters, Quartz is normally used due to its zero temperature coefficient. Also, using materials with opposite temperature coefficients can be used[93]. SAW based temperature sensors have been extensively studied by Hauden et al.[118], Bao et al.[119], Puccio et al.[120] to name a few.

2.4.2 Pressure

Acoustic sensors detect pressure changes mainly by the induced strain. Examples of acoustic wave pressure sensors include those studied by Talbi et al.[121], Schimetta et al.[122] and Vlassov et al[123]. To compensate for the effects of pressure or other interfering parameters on the response of an acoustic wave sensor, differential arrangement is used where one sensor acts as reference and hence compensates the effect of interfering parameters[124].

2.4.3 Mass loading

Acoustic wave devices are sensitive to mass loading on the surface and hence find applications in areas such monitoring the thickness of films and also chemical and biosensing. The theoretical and experimental values of the mass sensitivity of different acoustic wave devices are given in Table 2.1[42]. However, it should be noted that the mass sensitivity values are highly dependent on the center frequency of the SAW devices.

The mass sensitivities of the different acoustic devices are related to the structure geometry, resonant center frequency, properties of the substrate and the nature of the acoustic wave. A mass sensitivity factor, S_m, can be defined as[42]:

$$S_m = \lim_{\Delta m \to 0} \frac{(\Delta v / v_o)}{\Delta m} = \lim_{\Delta m \to 0} \frac{(\Delta f / F_o)}{\Delta m} \qquad \textbf{Equation 2-5}$$

where Δm is the uniformly distributed mass per unit area added to the surface of the device, v_o and F_o are the unperturbed acoustic wave velocity and device frequency and Δv and Δf are the changes in the acoustic wave velocity and hence the device frequency due to the mass loading. The other parameters in the table are as follows: ρ is the density of the plate material, d is the thickness of the plate, K(s,r) is a factor dependent on the piezoelectric properties of the substrate and the guiding layer, J_n is constant which is equal to ½ for n=0 and 1 if n>0. From the Table, it is clear that the Love Wave and FPW devices exhibit the highest mass sensitivities. This is due to the fact that the guiding layer in these devices effectively traps most of the acoustic wave energy at the top of the device[103, 104, 105].

Table 2.1: Comparison of example mass sensitivities for different acoustic wave devices

Sensor Type	Equation for Mass Sensitivity	Frequency (MHz)	Theoretical comparisons of mass sensitivities		Experimental	Ref
			Mass Sensitivity (Hz/MHz)/ (ng/cm^2)	MDL (ng/cm^2)	Mass Sensitivity (Hz/MHz)/ (ng/cm^2)	
TSM	$S_m = -\frac{1}{\rho d}$	20		32.5	0.038	60
Love-Mode Acoustic Wave		124	0.38	0.172		106
SH-APM	$S_m = -\frac{J_n}{\rho d}$	104	0.0186	2.5	0.0194	125
FPW	$S_m = -\frac{1}{2\rho d}$	3.2	0.19			126

The acoustic sensor response to mass loading requires careful interpretation to

identify the sensing mechanism. The problem of overlapping sensitivities to a number of parameters (such as temperature, pressure, viscosity, etc.) may inhibit the understanding of the process. Acoustic wave based gas sensors and biosensors are especially prone to this problem, and a great deal of research has been focused towards the development of arrays and smart sensor systems to address this, as outlined in the discussion above.

2.4.4 Viscoelasticity

Measurement of viscosity using acoustic wave sensors requires as little as a single droplet of the liquid and can be observed as a change in the insertion loss of the device or a change in the phase[74, 75]. However, since the phase change is largely influenced by temperature effects, it is required that the liquid be brought to the same temperature as the device in order to use phase change for viscosity measurements. Also, beyond a certain value of viscosity, the liquid relaxation time exceeds the acoustic wave period and the insertion loss saturates limiting the dynamic range of the sensor. The change in viscosity affects the propagation of acoustic wave in all applications involving liquid media. Hence, careful consideration should be given to applications where viscosity effects interfere with the desired sensing parameter under investigation. SH-APM and SH-SAW devices are mostly used for viscosity sensing due to the absence of the surface normal component of the wave. Therefore, the shear horizontal wave is not attenuated in liquid media.

2.4.5 Conductivity

The influence of electrical conductivity of a thin surface film on the surface wave velocity and attenuation is given by the following equations[108]:

$$\frac{\Delta v}{v_o} = -\frac{K^2}{2}\frac{\sigma_{sh}^2}{\sigma_{sh}^2 + v_o^2 C_S^2} \qquad \textbf{Equation 2-6}$$

$$\frac{\alpha}{k} = \frac{K^2}{2}\frac{v_o C_S \sigma_{sh}}{\sigma_{sh}^2 + v_o^2 C_S^2} \qquad \textbf{Equation 2-7}$$

where K^2 is the electromechanical coupling coefficient of the substrate, σ_{sh} is the sheet conductivity of the film and C_s is the capacitance per unit length of the surface. Acoustic wave sensors can be used to detect gas if these gases influence the conductivity of a thin surface film deposited on the piezoelectric substrate. From Equation 2-6 and Equation 2-7, it can be seen that the sensitivity of the conductivity based SAW sensors can be improved by using higher K^2 substrates. Therefore, Lithium Niobate is commonly used in conductivity based gas sensors due to its high K^2 and also lower mechanical coupling thereby eliminating the effects of mass changes. When SAW conductivity based sensors are used for detecting electrolytes, care should be taken to ensure that the buffer solution has the same viscosity and density as the electrolyte. Therefore, any observed frequency shifts will be then be solely due to changes in conductivity. Both SHSAW[73] and SHAPM[76] devices have been reported for use as conductivity based SAW sensors.

2.5 Summary

This chapter serves as an introduction to SAW devices and their sensing applications. It provided an overview of the different SAW device configurations that are suitable for a wide variety of applications ranging from sensors and ID-tags to filters in communication systems. A brief discussion about the different types of acoustic waves together with a summary of sensing mechanisms such as temperature, pressure, mass loading, viscoelasticity and conductivity was then presented. The following chapter deals with the burst transceiver that was designed and fabricated to communicate with SAW sensors.

CHAPTER III

BURST TRANSCEIVER: ARCHITECTURE AND RESULTS

3.1 Introduction

This chapter discusses in detail the interrogation unit which was introduced as part of the wireless passive sensing system in Chapter 2. Both the prototype burst transceiver and the miniaturized PCB versions were designed to provide power, interrogate, and receive responses for a range of SAW sensors. The system architecture capable of transmitting a burst of RF energy, receiving the RF sensor response, and then quadrature downconverting, digitizing, and collecting the data for processing will be described. The general design requirements for a wireless sensor transceiver will be defined and the useful operating range based on the signal power levels will then be discussed. It consists of transmit and receive sections. The transmit path sends the interrogation burst to the SAW sensor and the receive path then receives and processes the sensor response. The interrogation unit typically functions based on TDD (Time Division Duplexing) between the transmit and receive path[127, 128, 129]. This chapter describes the prototype burst transceiver and the miniaturized PCB version that was designed to provide power, interrogate, and receive responses for a range of SAW sensors. The system architecture capable of transmitting a burst of RF energy, receiving the RF sensor response, and then quadrature downconverting, digitizing, and collecting the data for processing will be described. The general design requirements for a wireless sensor transceiver will be defined and the useful operating range based on the signal power levels will then be discussed.

The simplified block diagram of the burst transceiver subsystem to interrogate a SAW sensor is shown in Figure 3.1. This transceiver was specifically designed to operate

in the 433 MHz instrumentation, scientific, and medical (ISM) frequency band. A brief operational description of the transceiver is given below.

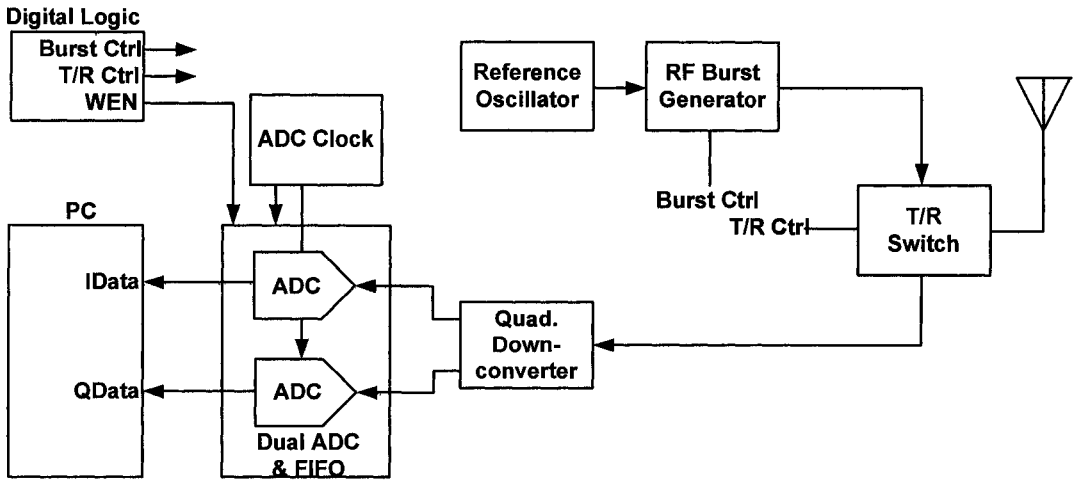

Figure 3.1: Simplified block diagram of the burst transceiver

The SAW sensor system prototype transceiver consist of two distinct segments; an RF signal burst transmitter and a high sensitivity RF receiver and coherent quadrature downconverter. A reference oscillator provides a coherent frequency reference for the transmit and receive paths. The continuous signal from the oscillator is converted to a short RF signal burst by using RF switches and power amplifiers. A transmit/receive (T/R) switch allows the burst to be transmitted before switching into the receive mode. The signal response of the SAW sensor is received and quadrature downconverted using Local Oscillator (LO) reference from the reference oscillator in the transmit path. After downconversion, a high rate, dual analog-to-digital converter (ADC) is used to sample the in-phase (I) and quadrature-phase (Q) baseband signals. The digitized signal samples are then buffered and stored for further processing and measurement extraction by a dedicated networked digital signal processor. Timing for the burst transmission, T/R switch and ADC sample buffer are all provided by the supporting digital logic.

By using a single reference oscillator for both the transmitted signal burst and quadrature demodulation, signal downconversion is coherent. A simple reflected burst response that is not modified by the SAW sensor should provide stable zero frequency I and Q sample values. The phase angle formed by the I and Q samples should be stable and will be based on the relative signal time delays due to the components and transceiver to sensor distance. When a SAW sensor causes a shift in frequency or a phase variation across a response burst, it will be observed in the quadrature I and Q samples. The relevant frequency and phase variations can then be calculated and the measurement derived based on known sensor calibration data.

3.2 Prototype burst transceiver

The prototype burst transceiver constructed for this project consists of multiple RF modules and manufacturer demonstration and development kits[130]. This allows rapid prototyping, simple system reconfiguration, and the opportunity to replace components with alternate or more advanced devices as they become available, from an available cost/performance basis. A detailed block diagram of the transceiver is shown in Figure 3.2. The modules constituting the RF transmit and receive path are shown inside the solid and dotted rectangles respectively. The frequency doubler and the amplifier generate the LO reference for the quadrature demodulator in the receive path.

The transceiver performs TDD between the transmit and receive signal paths. Since the burst requires a finite amount of time to be sent, arrive at the sensor, be applied and modified by the SAW device, and returned to the receiver, separate transmit and receive time intervals are defined and a transmit-receive (T/R) switch is used to select transmit and receive intervals. The switch, an HMC194MS8 GaAs SPDT from Hittite Microwave Corp., provides reasonable switching time (nominal of 10 nsec) and high isolation (nominal of 45 dB) between the transmit and receive paths. A simple, low-cost

custom antenna was constructed to both transmit and receive the wireless sensor signals.

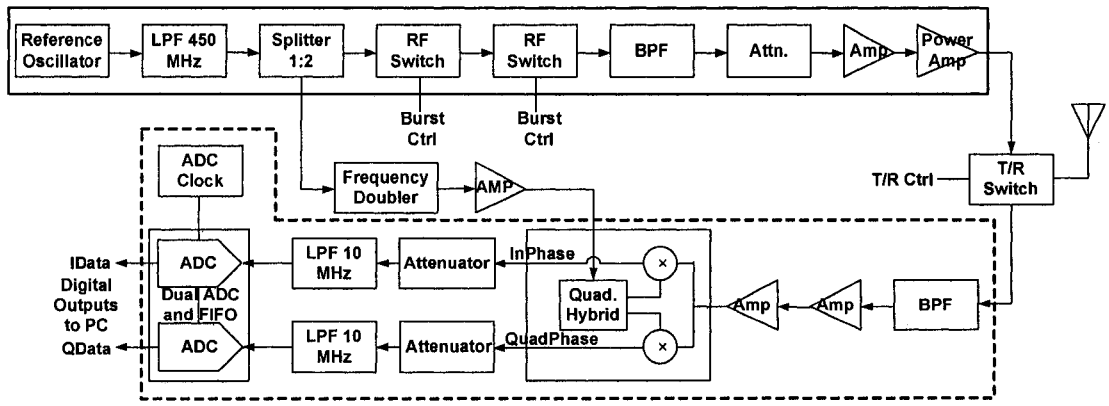

Figure 3.2: Detailed block diagram of the prototype burst transceiver

The transmission path provides a short duration RF burst that is sent to a burst-response SAW sensor. The path consists of a RF frequency that is split between the transmit and receive path, a dual RF switch, bandpass filter (BPF) and low power amplifier, a medium power amplifier, and a digitally controlled transmit/receive (T/R) switch. The receive path collects the burst response and coherently downconverts the signal for quadrature digital sampling and baseband processing. It consists of the T/R switch, bandpass frequency preselector, low noise amplifier, a quadrature downconverter, dual low pass filters, and a dual high-clock rate analog-to-digital converter (ADC). Not shown are the digital control logic, ADC data sample FIFO buffers and the host computer used which enable sampling the burst response and post-process the sampled data. The transmitter and the receiver block diagram are described in detail in the following sections.

3.2.1 Transmitter block diagram

To maintain frequency and phase coherence within the transceiver, a single reference oscillator (ZOS-535 from Mini-Circuits) is used to provide a 433 MHz reference to both the transmitter and receiver sections. In the transmitter, the continuous

reference is switched on or terminated to provide the required short duration burst. Both the RF switches and the T/R switch are GaAs SPDT switches, HMC194MS8 from Hittite Microwave Corp. The switches provide a reasonable 10 ns switching time and a minimum isolation of 45 dB between the RF1 and RF2 switch ports. When designing a medium power transmitter and a high sensitivity receiver, appropriate isolation must be provided during the receive period. Without power cycling the amplifiers, the residual transmitter output power with T/R switch isolation should be below the receiver noise floor of the transceiver. By using high isolation switches and the dual terminated switch configuration shown to generate the burst, the residual transmitter power is minimized.

After burst generation, filtering and gain compensation prior to power amplification is provided. Power amplification in the final configuration was performed in two stages, using a low power amplifier, a Mini-Circuits ZFL-500, and a medium power amplifier, a Mini-Circuits ZFL-2500VH. With nominal signal powers in the transmitter path expected between -10 dBm and +10 dBm, two amplifiers may not be ultimately required, but for testing purposes they are both available. For low power testing, the power amplifier is removed and a power output of +8 dBm can be sourced to the antenna. When the medium power amplifier is used, an output power of +22 dBm can be attained.

3.2.2 Transmitter gain and noise figure

A processing stage based block diagram of the prototype transmitter is shown in Figure 3.3. A cascaded gain and noise figure analysis of the expected performance during the burst signal transmission is shown in Table 3.1. Noise figure (NF) is a measure of degradation of the signal to noise ratio (SNR), caused by components in the RF signal chain. Noise Figure (*NF*) of each component in the chain is defined as the difference between the input and output SNRs,

$$NF = SNR_{in} - SNR_{out} \qquad \textbf{Equation 3-1}$$

where all the quantities are in decibels (dB). It is also sometimes expressed in linear units as a ratio called noise factor (F).

$$F = \frac{SNR_{in}}{SNR_{out}} \qquad \textbf{Equation 3-2}$$

When n components are cascaded, the noise figure of the overall chain is calculated using the following Frii's formula[131],

$$F = F_1 + \frac{F_2 - 1}{G_1} + \frac{F_3 - 1}{G_1 G_2} + \frac{F_4 - 1}{G_1 G_2 G_3} + \ldots\ldots\ldots\ldots + \frac{F_n - 1}{G_1 G_2 G_3 \ldots\ldots G_{n-1}} \qquad \textbf{Equation 3-3}$$

Also included in Table 3.1 is the measured performance when a continuous signal is transmitted. The expected and measured performances track each other well, with a buffered output power of + 4.57 dBm driving the antenna. By decreasing the attenuation, the maximum +8 dBm can be easily achieved.

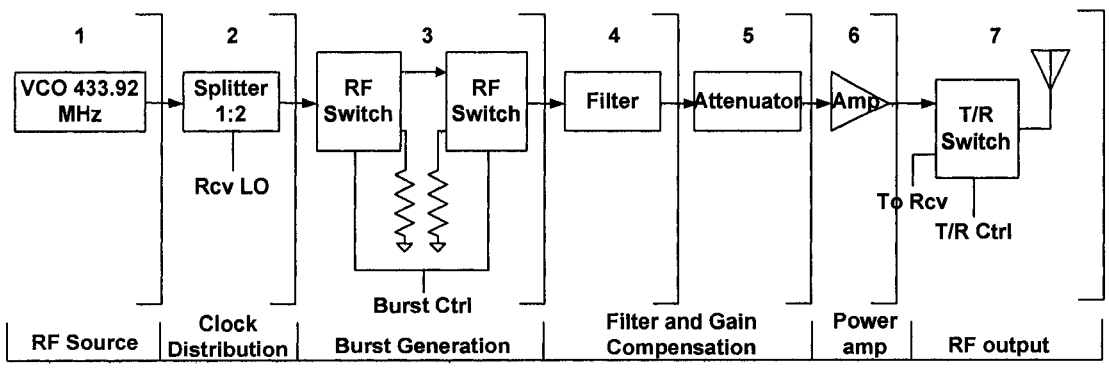

Figure 3.3: Transmitter processing stages

Table 3.1: Transmitter when transmitting - cascaded gain and noise figure

Stage	1	2	3a	3b	4	5	6	7
Gain (dB)	0.00	-3.50	-0.90	-0.90	-0.50	-20.00	20.00	-0.90
Noise Figure (dB)	0.00	3.50	0.90	0.90	0.50	20.00	5.30	0.90
Noise Figure (linear)	1.00	2.24	1.23	1.23	1.12	100.00	3.39	1.23
Total Gain (dB)	0.00	-3.50	-4.40	-5.30	-5.80	-25.80	-5.80	**-6.70**
Total Gain (linear)	1.00	0.45	0.36	0.30	0.26	0.00	0.26	0.21
Total NF (linear)	1.00	2.24	2.75	3.39	3.80	380.19	1288.25	1289.13
Total NF (dB)	0.00	3.50	4.40	5.30	5.80	25.80	31.10	**31.10**
Expected Signal Power (dBm)	10.00	6.50	5.60	4.70	4.20	-15.80	4.20	3.30
Measured Signal Power (dBm)	10.13	6.48	5.35	4.26	3.92	-16.29	5.65	4.57

As an additional note, while it would simplify the circuit to remove the attenuator and amplifier that result in a 0 dB cascaded gain, a buffer amplifier is needed between the burst switch and filtering stages and the T/R switch and antenna. The 5th and 6th stages provide this buffering with available components (and within maximum component input levels) while also providing a location for simple gain adjustments using different attenuators.

3.2.3 Receiver block diagram

When the receive path is selected, the SAW response signal is first filtered and amplified. Filtering is provided to reduce RF energy from adjacent signal bands. Amplification, first with a low noise amplifier, a Mini-Circuits ZFL-1000LN, and then a second amplifier, a Mini-Circuits ZFL-500, both limits the receiver noise figure and provide gain for weak signals. To measure subtle frequency changes or continuous phase variation caused by the SAW sensor, a coherent quadrature downconverter is used to translate the input waveform into a complex zero intermediate frequency (IF) waveform. By using a reference oscillator directly derived from the burst frequency, frequency offset between the receiver and transmitter is eliminated from the signal processing and any remaining complex frequency shift was thus caused solely by the SAW sensor. The quadrature downconverter was a demodulator evaluation board for the RF2721

quadrature modulator/demodulator from RF Micro-Devices (RF2721 PCBA-D).

After downconversion to a zero-IF, the in-phase and quadrature-phase (I and Q) outputs were low pass filtered (Mini-Circuits SLP-10) and attenuated before being sampled for digital signal processing by a dual ADC (AD9238) evaluation board from Analog Devices. While discrete components and an embedded processor would be used for a production application, the prototype used a digital FIFO board from Analog Devices to provide short term burst response data capture and a personal computer to both process the SAW responses and provide long term storage for the raw data. The HSC-ADC-EVAL-DC FIFO evaluation kit was used. It directly connects with the dual ADC board and provides a parallel port interface to a PC.

3.2.4 Receiver gain and noise figure

A processing stage based block diagram of the prototype receiver is shown in Figure 3.4. Based on the components selected, the signal power and noise figure levels for the design can be computed as shown in Table 3.2 using the same equations described in section 3.2.2. The receiver with a 10 MHz passband is designed to have a cascaded gain of 42.6 dB when both the amplifiers are operating in the receive chain and a receiver noise figure of approximately 6.0 dB.

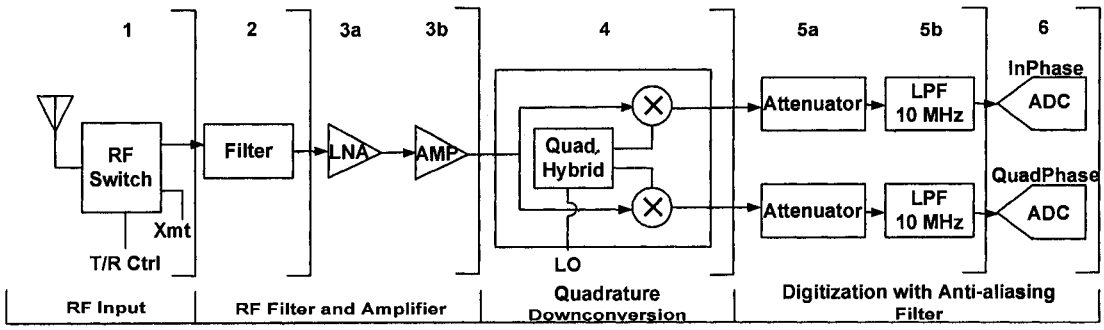

Figure 3.4: Receiver processing stages

Table 3.2: Receiver when receiving cascaded gain and noise figure

Stage	1	2	3a	3b	4	5a	5b
Gain (dB)	-0.90	-1.50	20.00	20.00	14.00	-6.00	-3.00
Noise Figure (dB)	0.90	1.50	2.90	5.30	35.00	6.00	3.00
Noise Figure (linear)	1.23	1.41	1.95	3.39	3162.28	3.98	2.00
Total Gain (dB)	-0.90	-2.40	17.60	37.60	51.60	45.60	**42.60**
Total Gain (linear)	0.813	0.575	57.544	5754.399	144543.977	36307.805	18197.009
Total NF (linear)	1.230	1.738	3.388	3.430	3.979	3.979	3.979
Total NF (dB)	0.90	2.40	5.30	5.35	6.00	6.00	**6.00**
Expected Signal Power (dBm)	-26.25	-27.75	-7.75	12.25	26.25	20.25	17.25
Measured Signal Power (dBm)	-28.19	-30.31	-10.27	11.84			

3.2.5 Oscillator reference frequencies

To maintain frequency and short-term phase coherence within the transceiver, a single reference oscillator is used to provide a 433 MHz reference to both the transmit and receive path. Figure 3.5 shows the block diagram of the LO reference generation circuitry that performs signal processing on the oscillator output to produce a signal at twice the input frequency for the quadrature demodulator LO reference. The reference oscillator is a ZOS-535 voltage-controlled oscillator (VCO) from Mini-circuits. The VCO has a tuning range of 300 to 525 MHz, providing a range of frequencies for prototype testing. Currently tuning is accomplished using a fixed DC supply voltage. A Mini-Circuits SLP-450 low pass filter is used to eliminate oscillator harmonics prior to the ZFSC-2-1 2-way 0 deg. power splitter that provides the two required transceiver references. The receiver reference is then frequency doubled using a Mini-Circuits MK-2 to provide the twice the input frequency required to drive the quadrature mixer. A ZFL-100 Mini-Circuits amplifier and gain adjustment attenuator follow the frequency doubler to provide the correct signal power level to the quadrature downconverter.

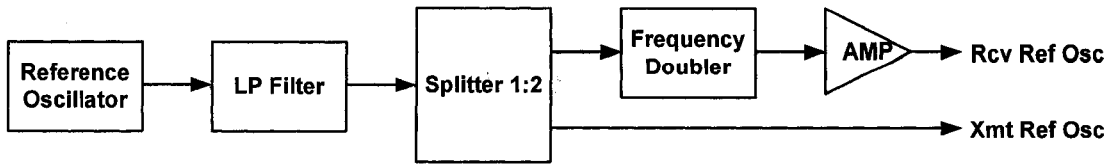

Figure 3.5: Transceiver frequency reference block diagram

3.2.6 Receiver sensitivity and maximum signal input

The receiver design is an iterative process based on a wide range of factors; including, output signal bandwidth, ADC maximum signal power levels, receiver gain, desired noise figure, derived thermal noise floor, etc. A diagram showing the applicable signal levels and performance for the prototype receiver is shown in Figure 3.6.

The bandwidth determined thermal noise floor is defined first as kT, where k is Boltzmann's constant which is 1.38×10^{-23} J/K, T is the temperature in degrees Kelvin (nom. 290 deg. K). For a 10 MHz receiver bandwidth (B), the equivalent thermal noise at the input to the receiver is -104 dBm ($10\log_{10}(kTB)+30$). The derived noise figure of the receiver from the input to the ADC is 6 dB (see Table 3.2 for the receiver noise figure) which sets the receiver noise floor at -98 dBm. For received signals above this power, the received signal-to-nose ratios (SNR) will be greater than 1 in a linear sense or positive when described in decibels. For received signal below this power, the SNR will be a linear fraction or negative when described in decibels. If it is assumed that an SNR of 8 dB or greater is needed to detect the signal response and derive a measurement, an 8 dB detection threshold (DT) can be added to the received noise threshold to define a signal power for the minimum detectable signal (MDS) level.

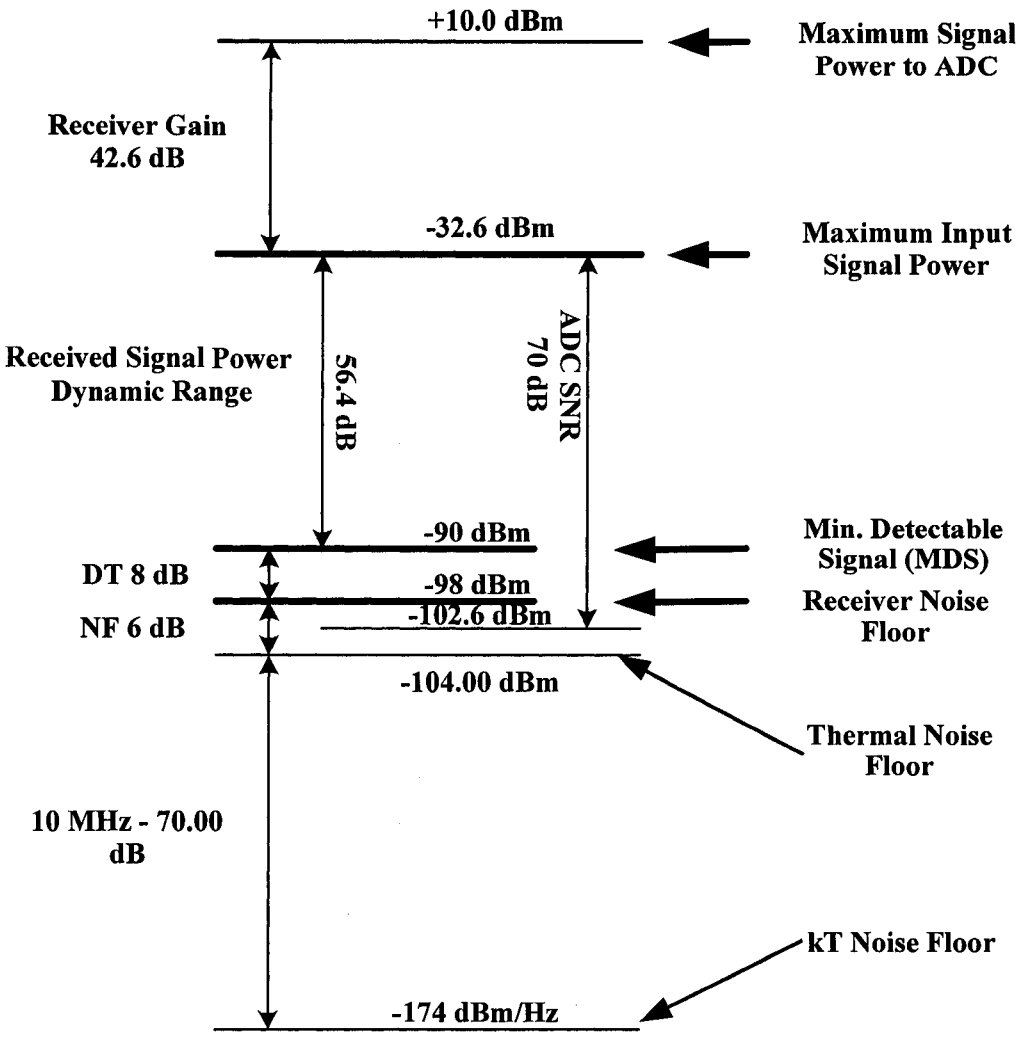

Figure 3.6: Receiver sensitivity and maximum signal input

If the receiver thermal noise is to dominate the noise contribution, the noise contribution of the ADC must be below the receiver noise floor. This is preferred in a digitizing receiver as the thermal noise may be modeled as Gaussian noise while the ADC noise may be correlated based on the device non-linearity and sampling performed. This can result in significant spurious response and reduce the useful receiver dynamic range. Thus, the minimum signal power that is within the available SNR of the ADC should be placed below the receiver noise floor. A second ADC consideration must also be accounted for, the maximum input signal to the ADC. The ADC preliminary

specification defines the SNR as 70 dB. For a maximum +10 dBm signal, that sets the ADC noise floor at –60 dBm or when translating this level to the receiver input, -102.6 dBm (see Table 3.2 for cascaded gain of the receiver). This level is 4.6 dB below the receiver noise floor and thereby satisfies the thermal versus ADC noise consideration previously described. Based on the ADC maximum signal level and the minimum detectable signal level, input response signals in the range of -32.6 dBm to -90 dBm, a dynamic range of 57.4 dB, can be detected and useful for parameter measurements. The AD9238 evaluation board provides RF input buffering with 50 ohm input impedance and allows a maximum input signal level of 2V peak to peak. For a sinusoidal signal, this corresponds to a maximum input signal power of +10 dBm ($10\log_{10}\left(\left(1/\sqrt{2}\right)^2/50\right)+30$).

Translating the ADC level to the input of the receiver (by subtracting the receiver gain), the maximum, non-saturating input signal power of the receiver is –32.6 dBm.

3.3 Prototype burst transceiver – test results

Burst transmission tests were conducted on the transceiver and the experimental setup is shown in Figure 3.7. The transmitter was configured to produce 180 μs duration RF burst and the receiver was configured to receive and process the burst signal. The signal levels at the output of the different sections of the receiver chain were recorded. Power levels at the various receiver stages were measured in the presence and absence of the RF burst. The results are summarized in Table 3.3. From the table, it can be seen that there is an approximate 50 dB attenuation in signal level (at the output of each receiver stage) when the transmitter is OFF mainly due to the isolation provided by the RF switches in the OFF state. The residual power that is seen in the Burst OFF state was found to be mainly due to the power radiated by the oscillator in the transmit path. This radiation was observed even after shielding the oscillator using a diecast aluminum enclosure and hence was an important challenge faced with the prototype burst

transceiver.

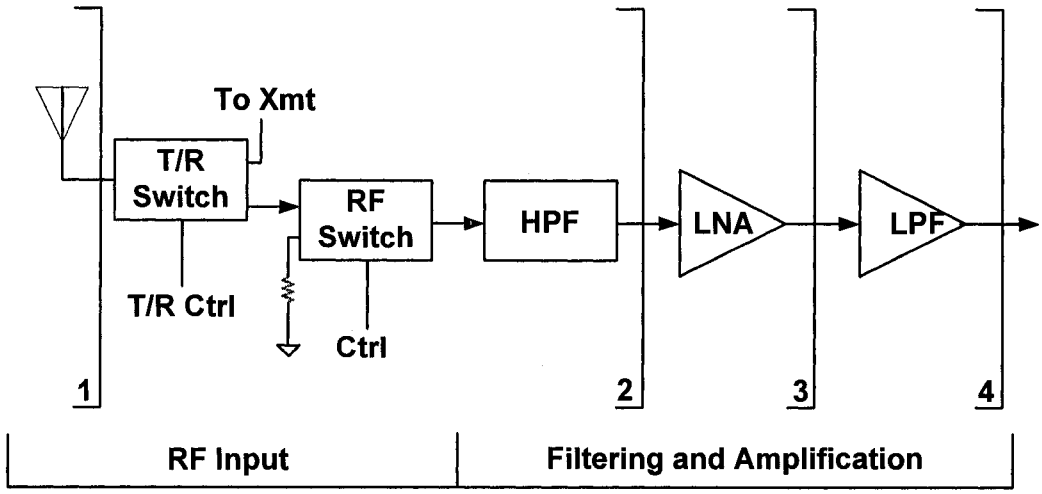

Figure 3.7: Block diagram of the experimental setup

Table 3.3: Summary of burst transmission test results

Output Signal Level (dBm)	Antenna	HPF	LNA	LPF
Burst ON	-23	-24	-0.7	-5
Burst OFF	-54.101	-75.05	-57.679	-59.689

Following this, a filtering and gain compensation circuit was designed whose schematic is shown in Figure 3.8. This circuit will filter out any high frequency components and also amplify the In-Phase and Quadrature outputs before digitization by the Dual ADC. A custom third-order Butterworth filter with a 10 MHz cutoff frequency was designed for this purpose[132]. Opamps were used to provide the 2.5V reference (IC741) needed for the quadrature down converter and also for bias cancellation of the filtered I and Q outputs (THS4001 from Texas Instruments). The overall gain of the circuit can be obtained as follows:

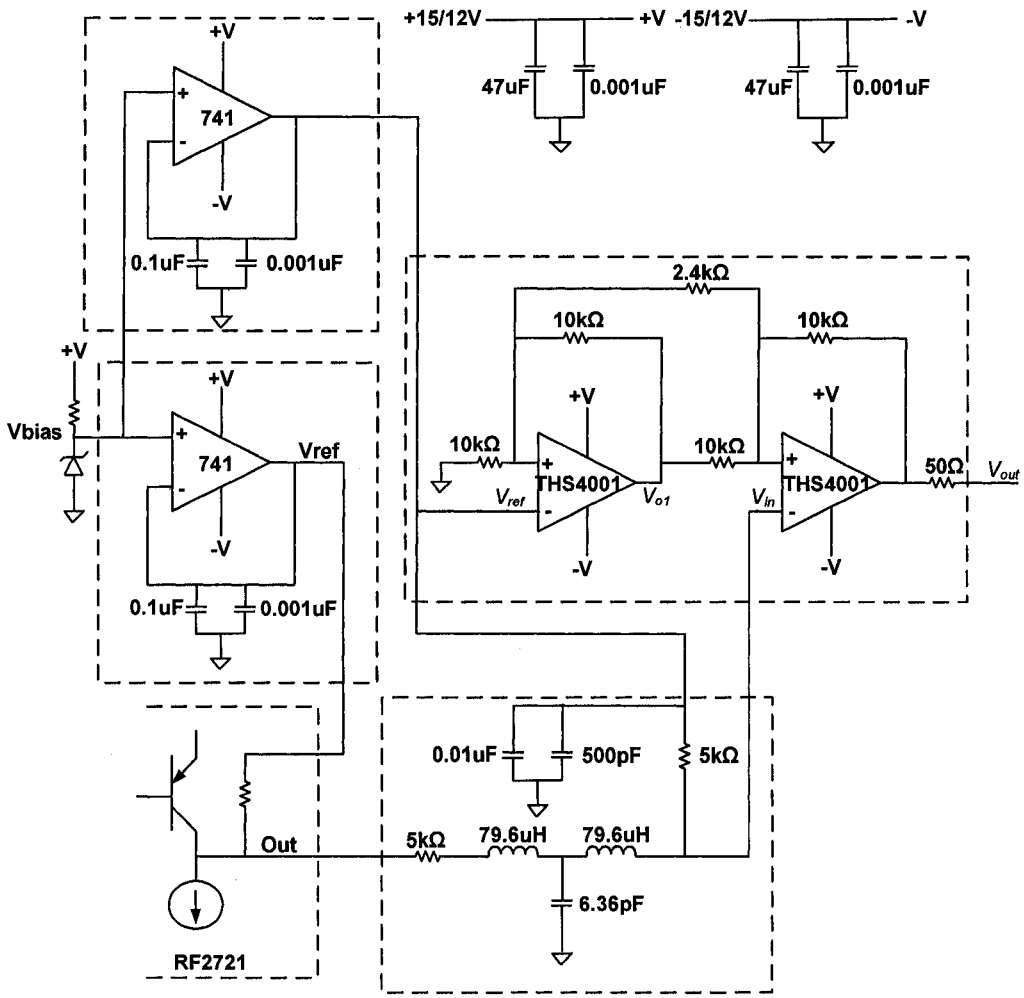

Figure 3.8: Filtering and gain compensation

Using KCL at nodes 1 and 2, we get the following two equations.

$$\frac{-V_{ref}}{10} = \frac{V_{ref} - V_{o1}}{10} + \frac{V_{ref} - V_{in}}{2.5} \qquad \textbf{Equation 3-4}$$

$$\frac{V_{ref} - V_{in}}{2.5} + \frac{V_{o1} - V_{in}}{10} = \frac{V_{in} - V_{out}}{10} \qquad \textbf{Equation 3-5}$$

The output of the filter circuit which is also the input to the opamp circuit can be written as

$$V_{in} = V_{ref} + V_{ac} \qquad \textbf{Equation 3-6}$$

Substituting this equation in Equations 3-4 and 3-5 and solving for V_{out}, we get

$$\frac{V_{out}}{V_{in}} = 10 \qquad \textbf{Equation 3-7}$$

and therefore the power gain of the opamp circuit can be written as

$$PowerGain = 10 \cdot \log_{10}\left(\frac{V_{out}}{V_{ac}}\right)^2 = 20dB \qquad \textbf{Equation 3-8}$$

The differential amplifier configuration thus provides a gain of 20 dB. The third order butterworth low pass filter with a 10 MHz cutoff frequency has a loss of 6 dB in the pass band. Taking the loss in the filter into account, it can be said that the overall gain provided by the filter and gain compensation circuit is 14 dB. Two of these circuits were built on a copper board one for each of the quadrature down converter outputs. The frequency response of this circuit was then measured using a Spectrum Analyzer as shown in Figure 3.9. It can be seen that the overall gain of the circuits is around 14 dB over a bandwidth of 6 MHz.

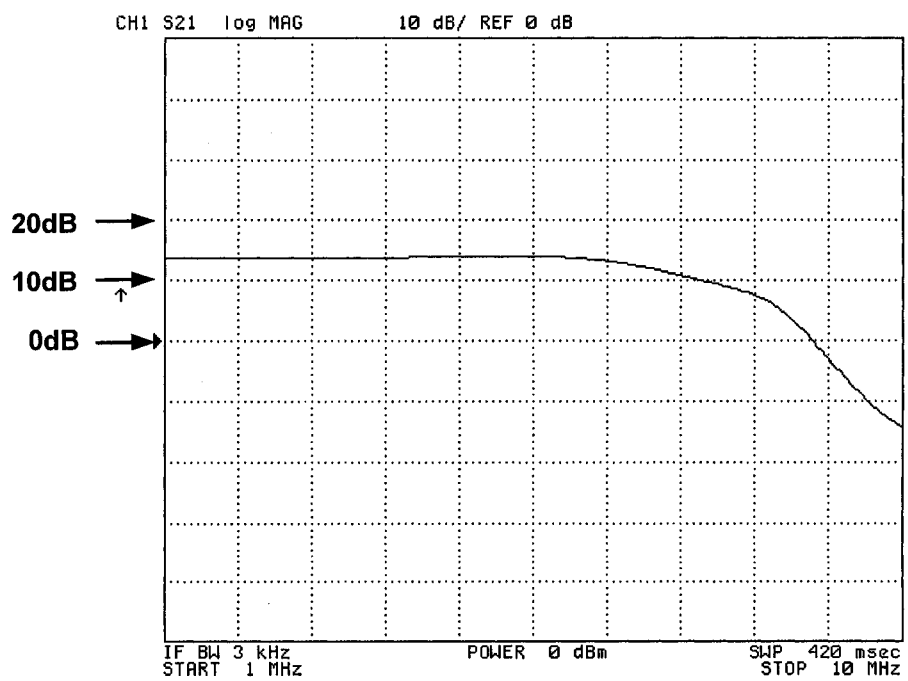

Figure 3.9: Frequency response of the filter and gain compensation circuit

The prototype burst transceiver including the LO reference generation path, the quadrature downconverter, the filter and opamp circuit and the dual FIFO and ADC were tested with the digitized I and Q outputs fed to a PC for further processing in MATLAB™. The test schematic is shown in Figure 3.10. A signal generator was used for the LO generation path instead of the VCO output so as to create a frequency offset that can be easily analyzed using MATLAB™. The burst duration was 180 μs at a frequency of 433 MHz and the signal generator was set to produce a 435 MHz signal at +3 dBm.

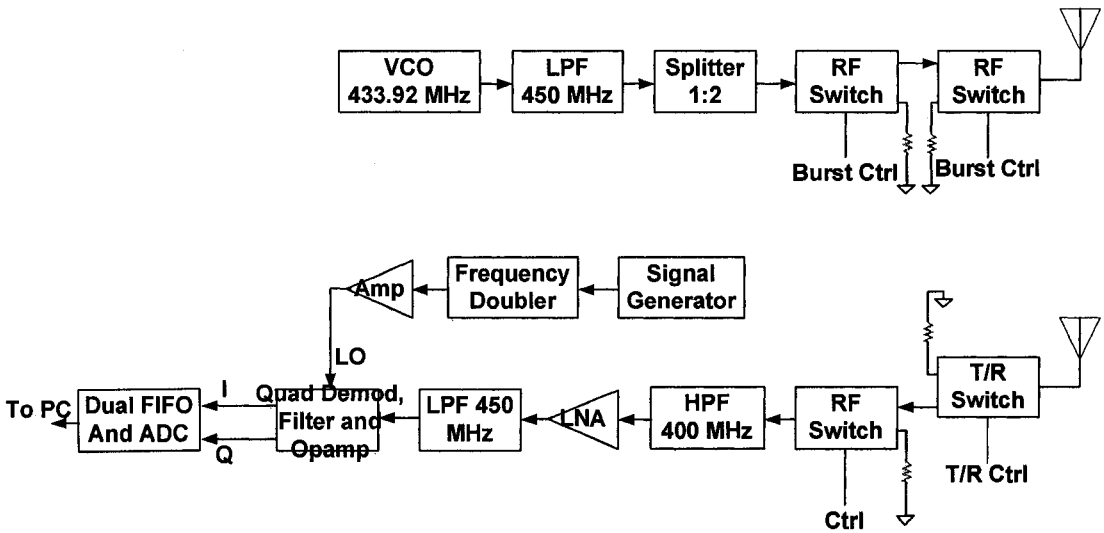

Figure 3.10: Experimental set-up with ADC and FIFO board connected to PC

Figure 3.11 shows the results of the digitized data processed in MATLAB™. The spectrum shows that I and Q signal frequency is around 1.682 MHz which was the frequency offset between the VCO and the signal generator used for LO reference. Also seen in this figure are the second, third and fourth harmonic at 3.364 MHz, 5.04 MHz and 6.723 MHz respectively. Having completely characterized the prototype burst transceiver, a PCB was then designed, fabricated and tested. Figure 3.12 shows a

photograph of both the prototype and the PCB that were built and tested. The following sections describe the architecture and the results obtained from the burst transceiver PCB.

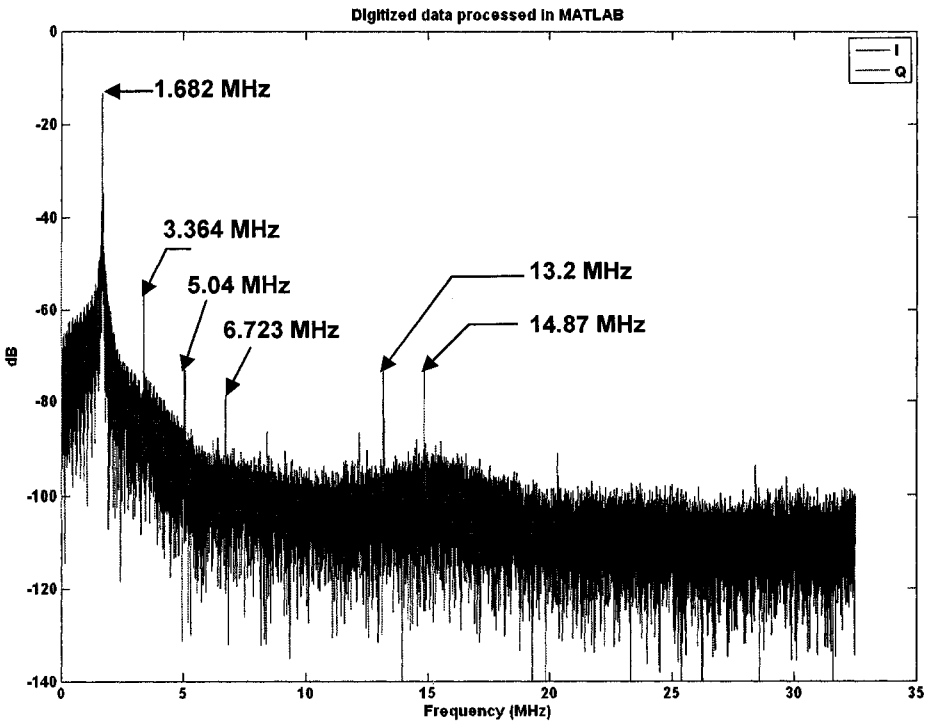

Figure 3.11: Power spectrum of the I and Q outputs plotted in MATLAB™

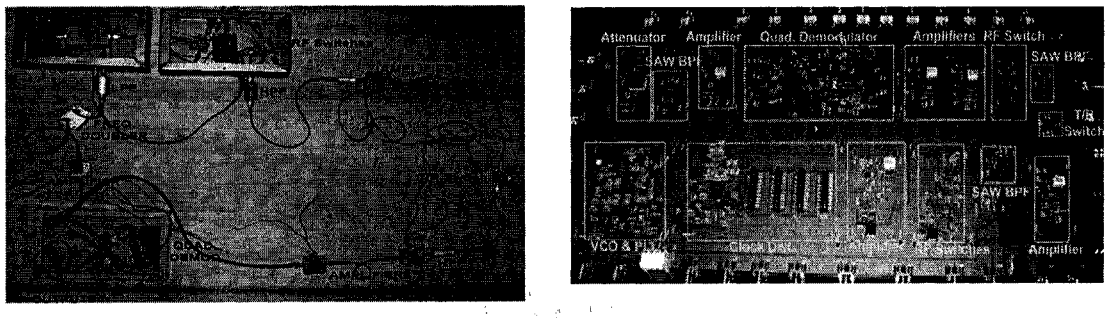

(i) Prototype (ii) PCB

Figure 3.12: Photograph of the burst transceiver prototype and PCB

3.4 Burst transceiver PCB

After the prototype burst transceiver was tested for its functionality using coaxial components, surface mount devices with similar characteristics were identified in order to build a burst transceiver Printed Circuit Board (PCB) to be used as part of the passive wireless SAW sensing system. Figure 3.13 shows the overall block diagram of the burst transceiver PCB. The transmit and receive path are shown within the solid and dotted rectangles respectively. In order to maintain frequency and phase coherence, a single clock reference is used for both transmit and receive paths just as in the prototype transceiver. However, in this case, the Integrated Synthesizer and VCO (ADF4360-7 from Analog Devices) generates a stable 868.84 MHz signal and the clock distribution circuitry (AD9515 from Analog Devices) provides two outputs one at 868.84 MHz and the other output with divide by 2 option enabled so as to provide a 434.42 MHz signal required for burst generation. The digital controls for the integrated synthesizer and VCO and the RF switches are provided using a Spartan II FPGA Prototyping board. The VHDL code that was used to generate the digital controls is given in Appendix A. With this configuration, even if the 868.84 MHz signal is radiated into the receive path it does not interfere with the sensor response in the 434.42 MHz band. The 434.42 MHz continuous signal is first amplified before being sent to the RF Switches for burst generation. The digitally controlled switches generate a short duration RF burst. The cascaded configuration provides a high isolation of ~90dB when the transmit path is disabled. The generated burst is first filtered using a SAW BPF centered at 434.42 MHz (B3757 from EPCOS). The SAW filter has a low insertion loss of 3 dB in the passband (434.26 – 434.58 MHz) and has excellent rejection characteristics in the stop band (~80dB attenuation at 900 MHz). The filtered signal is once again amplified before being transmitted to the SAW sensor. The amplifiers used in the transmit and receive path (MAV-11SM from Minicircuits) were selected to have a gain between 10 and 12 dB in the 434 MHz range so that the signal level at the input to the T/R switch does not

exceed the +27 dBm maximum rating specified. The amplifier used in the LO reference generation path has a slightly higher gain (15-18 dB) in order to be able to meet the minimum signal level requirements (-12 dBm) for the LO reference input of the Quadrature demodulator. The filter in the LO reference section is also a SAW BPF (B3571 from EPCOS) with a very narrow pass band centered around 868.69 MHz and good rejection characteristics.

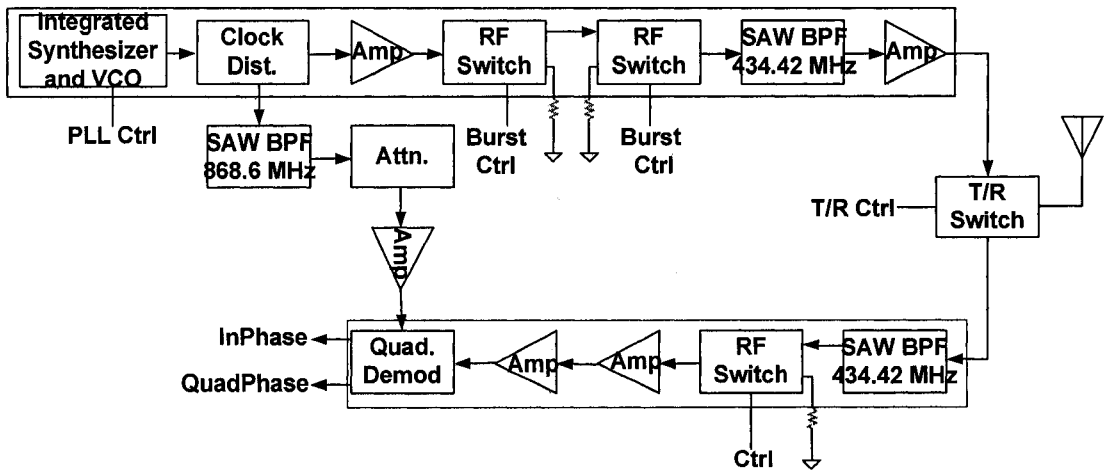

Figure 3.13: Block diagram for burst transceiver PCB

In the receive path, the SAW sensor response is first filtered and amplified before being sent to the quadrature demodulator (AD8348 from Analog Devices). The RF switch in the receive path provides an additional 45 dB isolation thus preventing any residual transmit signal from saturating the receive amplifiers. The following sections describe each of the individual sections of the transceiver in further detail.

3.4.1 Transmitter block diagram

The transmitter consists of a stable continuous reference at 434.42 MHz which is provided by the Integrated Synthesizer and VCO, ADF4360-7 from Analog Devices. This RF signal is then given to the clock distribution IC, AD9515 also from Analog

Devices which provides dual output, one at 434.42 MHz and other at 868.84 MHz, which are then used in the transmit path and LO reference sections respectively. The 434.42 MHz output from the clock distribution IC is amplified using a Minicircuits MAV-11SM amplifier before being sent to the burst generator. The burst generator consists of two RF switches which are switched ON/OFF at the appropriate instance to generate the required short duration RF burst. The burst thus generated is filtered using a SAW BPF with center frequency 434.42 MHz before being further amplified. The amplified signal is then transmitted to the SAW sensor through the T/R Switch. The following sections describe the schematic associated with each of the processing stages of the transmit path.

3.4.1.1 Integrated synthesizer and VCO

The integrated synthesizer and VCO can provide output frequencies in the range between 350 MHz and 1800 MHz. In addition, a divide-by-2 option is available on the output which can be enabled using the N-counter latch. With this option enabled, the attainable output frequency ranges between 175 MHz and 900 MHz. The schematic of the integrated synthesizer and VCO is shown in Figure 3.14. The PLL is programmed to produce the 868.84 MHz output and also to mute the RF outputs until the PLL locks to the right frequency. During initial power up, the R counter, control and N counter latch are programmed in the exact order using the Spartan II FPGA prototyping board paying careful attention to provide enough interval between programming the control and N counter latch to let the transient behavior of the ADF4360-7 during initial power-up to settle. The oscillation frequency of the VCO is set using two external inductors as shown in SUBCKT3 of Figure 3.14. The relationship between the external inductance value and the center frequency of VCO is given by the following equation:

$$f_o = \frac{1}{2\pi\sqrt{6.2pF(0.9nH + L_{ext})}} \qquad \textbf{Equation 3-9}$$

where 0.9nH represents the internal inductance due to the bond wires and the approximate value of the capacitance at the center band of the VCO is 6.2pF. Based on the center frequency required, the external inductance value can be calculated. For the 868.8 MHz output this inductance value was calculated to be 4.5 nH using the above equation. However, the PCB traces contributed additional inductance and therefore, the external inductance had to be lowered to 3nH to enable the PLL to lock to the right frequency. Depending on the desired output frequency and phase detector frequency, the values for R, A and B are calculated so as to satisfy the following relation

$$f_{VCO} = (A + BP) \cdot \frac{f_{ref}}{R} \qquad \textbf{Equation 3-10}$$

Using a 10 MHz reference frequency, the values of A, B, P and R were calculated to be 0, 4344, 8 and 400 respectively assuming 868.8 MHz PLL output frequency and 25 KHz phase detector frequency.

The reference frequency for the PLL is provided using 10 MHz crystal from Epson Electronics. The loop filter takes the output of the charge pump and provides the appropriate tuning voltage to the VCO and is shown in SUBCKT2 in Figure 3.14. The design tool ADIsimPLL from Analog Devices was used to determine the component values in the loop filter for a 2.5 kHz bandwidth and 45° phase margin. The output stage of the ADF4360-7 consists of an RF choke to VCC and a 100pF capacitor. The differential outputs from the synthesizer had a frequency of 868.8 MHz and a signal level of -5 dBm when measured with a TDS5104B Digital Phosphor Oscilloscope (see Figure 3.15).

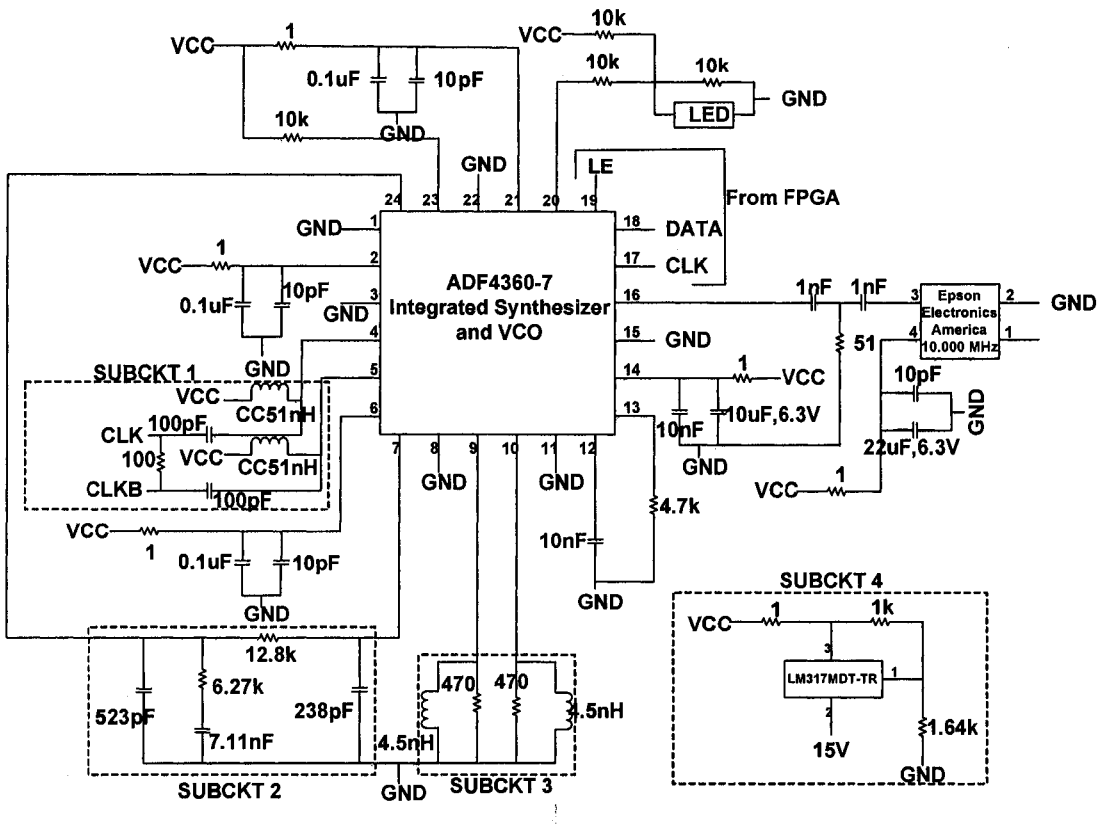

Figure 3.14: Integrated synthesizer and VCO schematic

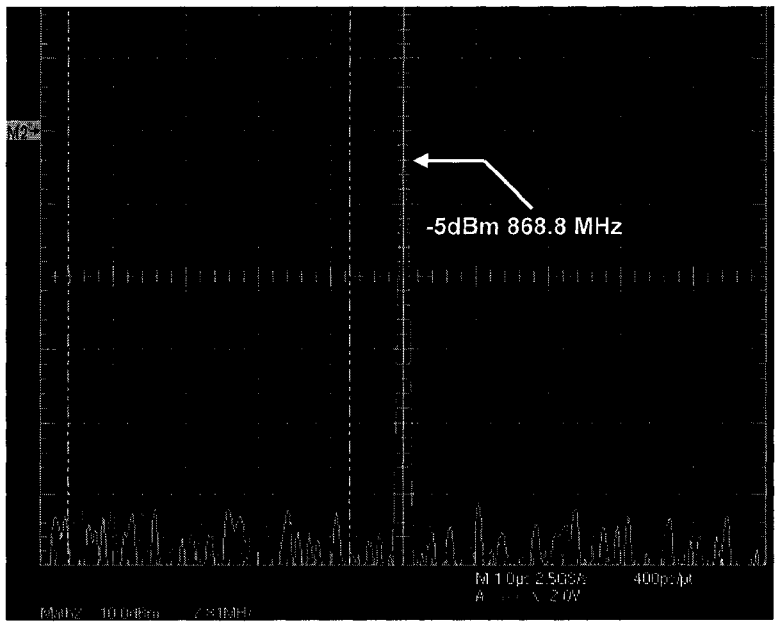

Figure 3.15: Integrated synthesizer differential outputs

3.4.1.2 Clock distribution

The clock distribution IC AD9515 is capable of providing two independent clock outputs each with a programmable divider and adjustable delays. One output is LVPECL (Low Voltage Positive Emitter Coupled Logic), while the other one can be configured either as LVDS (Low Voltage Differential Signaling) or CMOS. The LVPECL output can operate upto 1.6 GHz whereas the LVDS and CMOS can provide upto 800 MHz and 250 MHz respectively. The LVDS output was chosen to provide the 434.42 MHz signal for the transmit path and the LVPECL output is programmed to provide the 868.84 MHz reference signal for the LO. The schematic for the clock distribution circuitry is shown in Figure 3.16. The programming pins S0-S10 (pins 7-16 and 25 of the IC) can be used to adjust the delay, power level and divide ratio for the two outputs. Jumpers are placed on the PCB which enable the DC levels at these pins to be set to one of the four logic levels (0V, 1/3Vs, 2/3Vs, Vs) as required.

One of each of the LVPECL and LVDS outputs are terminated using a 50 ohm resistor. The other 868.8 MHz LVPECL output is used to feed the LO reference path and the other 434.4 MHz LVDS output is used to drive the amplifier in the transmit path. An optional arrangement using 127 Ω and the 83 Ω resistors (shown in dotted rectangle) can be used to provide a 50 Ω termination to V_s-2 volts ($R1 \| R2 = 50\Omega$ and $\frac{V_s R_2}{R_1 + R_2} = 1.3$).

Linear regulators (LM317MDT shown as a separate circuit in Figure 3.16) were used to provide a regulated DC supply voltage for all stages of the burst transceiver.

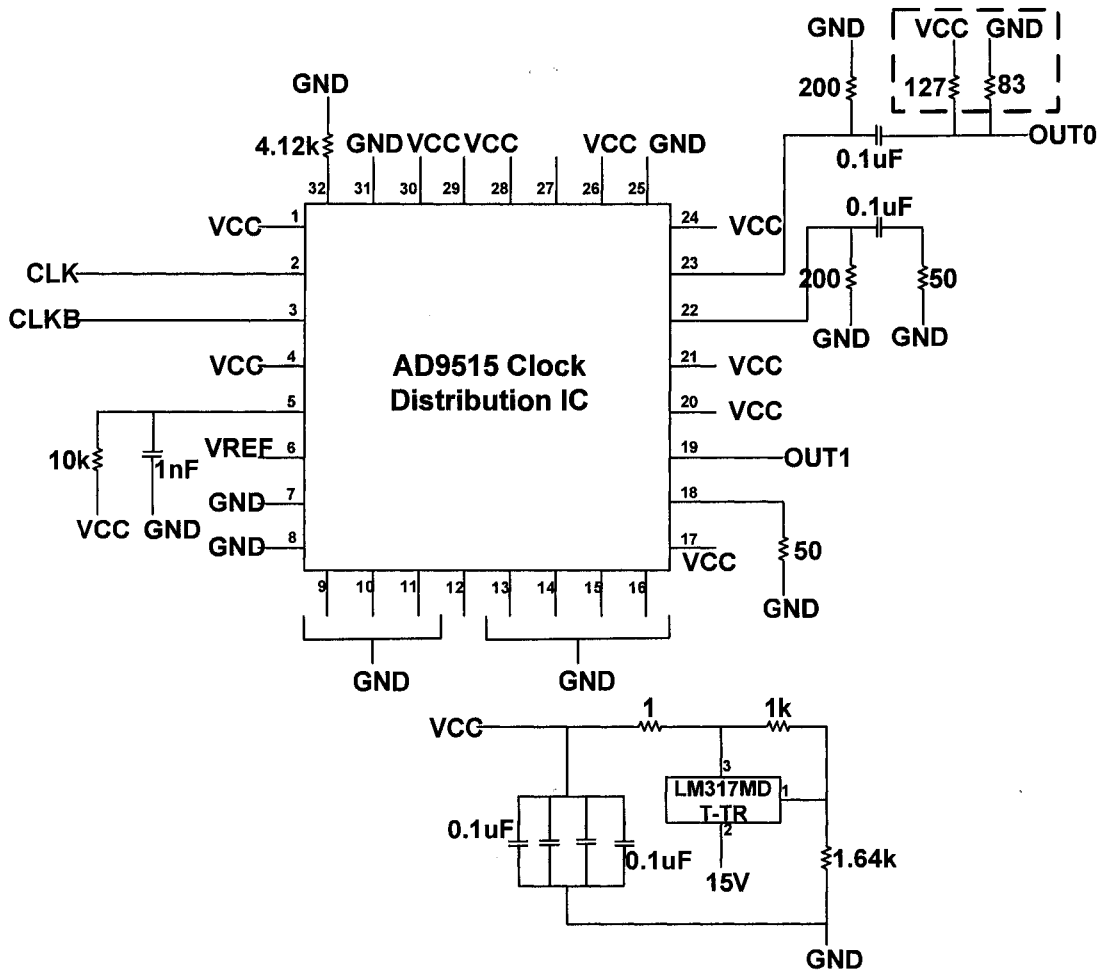

Figure 3.16: Clock distribution schematic

3.4.1.3 RF amplifiers

The 434.42 MHz output from the clock distribution circuit is processed in the subsequent stages of the transmit path before being sent to the SAW sensor. This signal is first amplified using MAV-11SM amplifiers from Mini-Circuits, which provide a gain of approximately 11 dB with a maximum output power of +17.5 dBm. The schematic for the amplifier circuitry is shown in Figure 3.17. The capacitors at the RF input and output of the amplifiers are used to block any dc that might be present. In addition, the resistor and RF choke provide the appropriate bias levels for the amplifier while at the same time minimizing the loss in the biasing resistor.

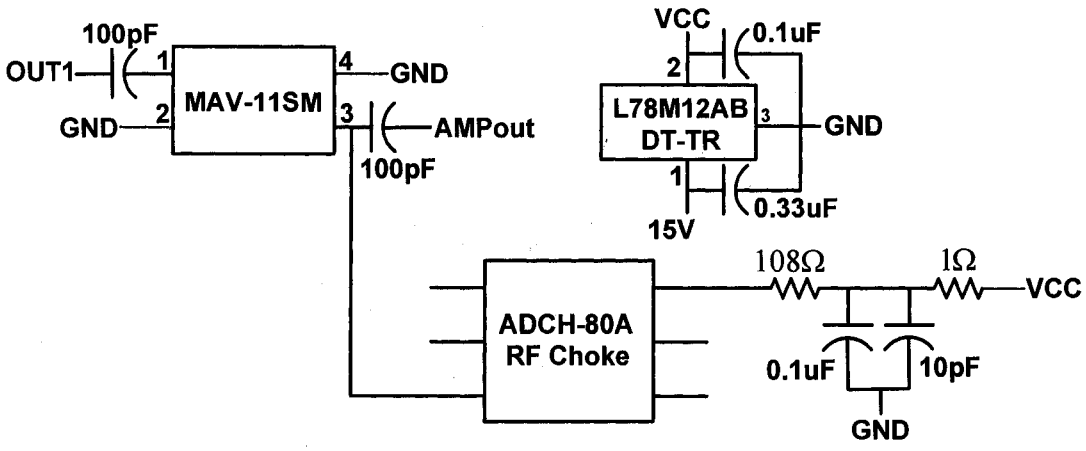

Figure 3.17: Low power amplifier schematic

3.4.1.4 Burst switches

A short RF signal burst is obtained from the 434.42 MHz CW signal by using two RF switches (HMC194MS8 from Hittite Microwave) in cascade. This schematic is shown in Figure 3.18. The control signals A and B (a "HIGH" on A makes channel 2 conducting and vice versa) enable either channel 1 or channel 2. While the burst is being transmitted channel 2 is enabled in both the switches. When the burst transmission is OFF and the receiver is operating, channel 1 is enabled in the cascade switches. The switches have a switching time of 10ns and a loss of 0.9 dB when conducting and also provide a good 45 dB isolation when connected to a 50 Ω termination. Thus, a total of 90 dB isolation is provided by the switches when in the OFF state.

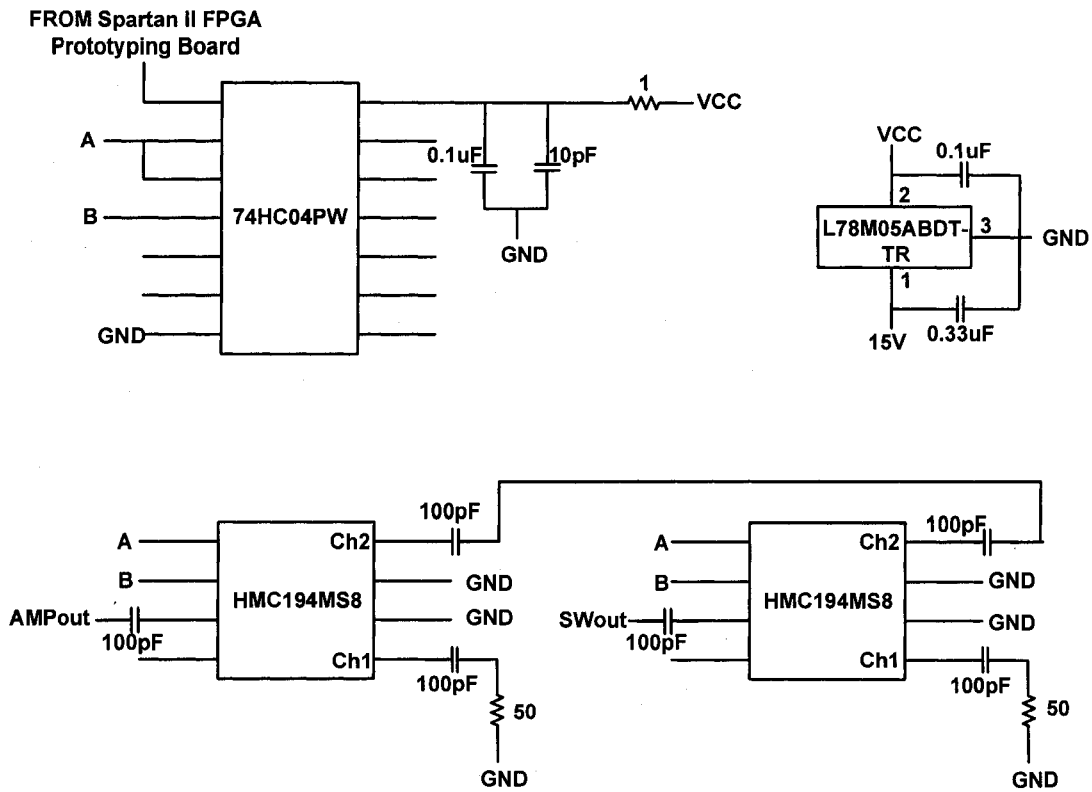

Figure 3.18: RF burst switches schematic

The control input for all the switches in the burst transceiver circuit are provided by the Spartan II FPGA prototyping board through the hex-inverter (74HCT03 from Philips Semiconductors).

3.4.1.5 Band pass filter

The burst signal is then filtered using a SAW BPF centered at 434.42 MHz (B3757 from EPCOS) before further amplification. The schematic is shown in Figure 3.19. The filter with careful PCB layout and matching circuitry has <3dB loss in the narrow 1 MHz passband centered at 434.42 MHz and has an attenuation of >65 dB at 868.84 MHz thus preventing any undesired signal from being transmitted to the sensor. The inductors at the input and output of the filters tune out the IDT capacitance and provide impedance matching to 50 ohms. Once filtered, the burst is further amplified before being transmitted to the SAW sensor.

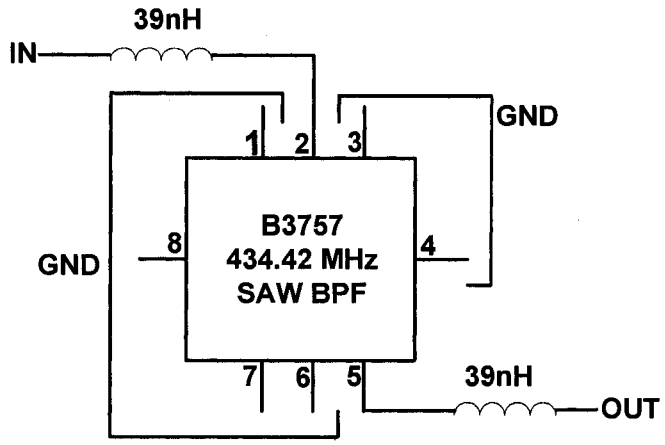

Figure 3.19: SAW BPF schematic

3.4.2 LO reference generation

Figure 3.20 shows the schematic for the circuit that processes the 868.84 MHz signal before it is given to the LO input of the quadrature demodulator. Filtering is achieved using a SAW BPF centered at 868.6 MHz (B3571 from Epcos). The schematic for the filter circuitry is identical to the one shown in Figure 3.19.

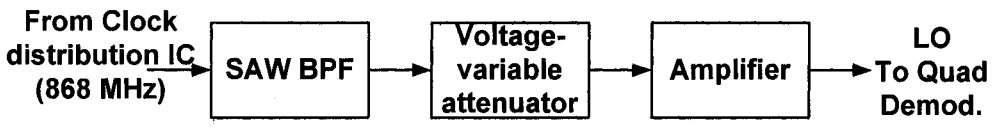

Figure 3.20: LO reference generation schematic

The filtered output is then sent to a gain control stage. It consists of a voltage variable attenuator (RVA-2500 from Minicircuits) in series with an amplifier (MAR-1SM from Minicircuits). The gain control stage ensures that the power level at the output meets the specifications stated for the LO input (-12 dBm to 0 dBm) of the quadrature demodulator. The schematic for the voltage variable attenuator circuit is shown in Figure 3.21.

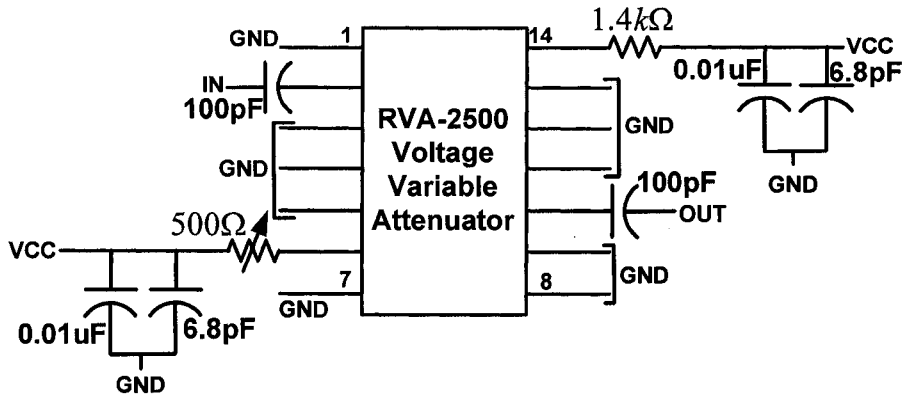

Figure 3.21: Voltage variable attenuator schematic

The 1.4 kΩ resistor is used to provide the appropriate DC level for the operation of the attenuator using a 12 V DC supply. The 500Ω potentiometer can be adjusted to control the attenuation provided by this stage.

3.4.3 Receiver block diagram

The receiver section of the burst transceiver is shown as part of Figure 3.13. The response from the SAW sensor is received by the T/R switch when in Receive mode and is filtered using a SAW BPF centered at 434.42 MHz, the same filter used as part of the transmit path. The filtered signal is then sent to another RF switch. The main purpose of this switch is to provide an additional 45 dB isolation in order to prevent any residual transmitted signal from saturating the amplifiers in the receive chain. The signal is then amplified using two MAV-11SM amplifiers whose schematic is shown in Figure 3.17. The amplified signal is then quadrature downconverted (using AD8348 from Analog Devices). Since the schematic of the other components have been discussed in the Section 3.4.1, the schematic for the AD8348 alone is described here.

3.4.3.1 Quadrature demodulator

The sensor response after being amplified in two stages is quadrature downconverted to provide the In-Phase and Quadrature-Phase outputs. The building

blocks of the quadrature demodulator are shown in Figure 3.22. The AD8348 is a quadrature demodulator with an integrated IF Variable Gain Amplifier (VGA) and baseband amplifiers. The baseband amplifiers are designed so that they can directly integrate with dual channel ADCs for digitization and further processing. Matching resistors are used to provide a 200 Ω source impedance to the IF input. These resistors form an L-pad at the IF input of the Quadrature Demodulator. The IF input signal is fed into the mixers after passing through an IF VGA. Optionally, the IF input can be directly given to the mixer thus bypassing the VGA. The VGA provides 44 dB of gain control. The gain of this amplifier stage can be controlled by the DC level at the VGIN pin of AD8348. Although the VGA provides a maximum gain of 25.5 dB to the IF input, the L pad placed at the IF input pin for impedance matching contributes an additional 11.5 dB. The LO quadrature phase splitter consists of a frequency divider to achieve high quadrature accuracy. Baseband amplifiers following the mixer I and Q outputs provide an additional 20 dB gain to the baseband outputs. The voltage applied to the VCMO pin sets the dc bias level at the baseband outputs. The VCMO pin can also be connected to internal 1V reference available at the VREF pin. The VCMO voltage can thus be selected to maximize the ADCs dynamic range.

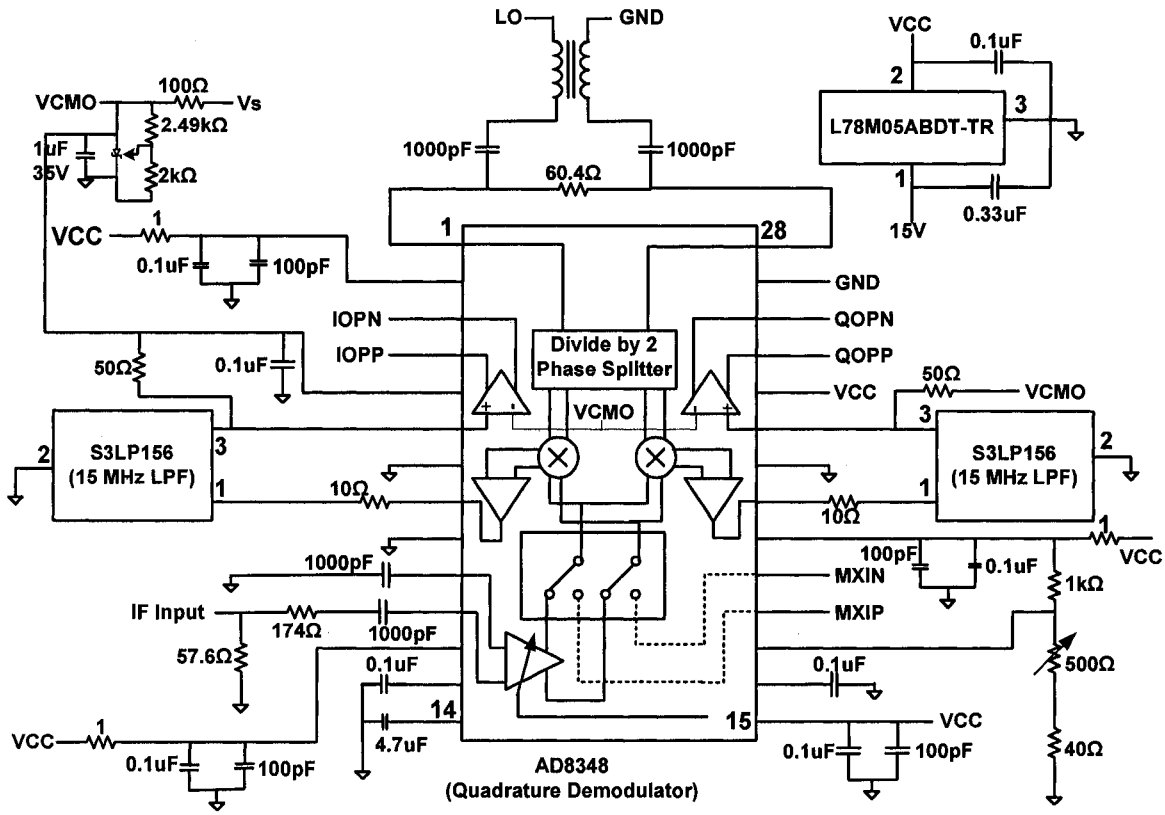

Figure 3.22: Quadrature demodulator schematic

The mixer outputs can be filtered using an external filter before being fed into the baseband amplifiers. Third order Butterworth low pass filters with 15 MHz cutoff frequency (S3LP156 from Coilcraft) were used for this purpose. These filters have a 50Ω characteristic impedance and have less than 0.3dB insertion loss. The single ended LO reference coming from the amplifier MAR-1SM is converted to a differential signal using a balun ETC1-1-13 from M/A-com. The overall gain in the quadrature demodulator stage (G_{QD}) can therefore be derived as

$$G_{QD} = G_{VGA} + G_{AMP} - L_{LPAD} - L_{LPF} = 25.5 + 20 - 11.5 - 0.3 = 33.7dB \qquad \textbf{Equation 3-11}$$

where G_{VGA} and G_{AMP} are the VGA and baseband amplifier gains and L_{LPAD} and L_{LPF} are the losses in the L-pad used at the IF input and the low pass filter respectively.

3.4.4 Receiver sensitivity and maximum signal input

Similar to Figure 3.6, the receiver dynamic range and various signal levels are shown in Figure 3.23 for the burst transceiver PCB. As can be seen, the receiver noise floor is at –95.5 dBm and the minimum detectable receiver signal is –87.5 dBm. With the maximum signal input to the ADC set at +10 dBm and the receiver gain being 49.9 dB, this gives a receiver dynamic range of 47.6 dB for useful parameter measurements. Also, the noise contribution of the ADC is at –109.9 dBm which is well below the receiver noise floor thereby preventing any spurious responses in the receiver.

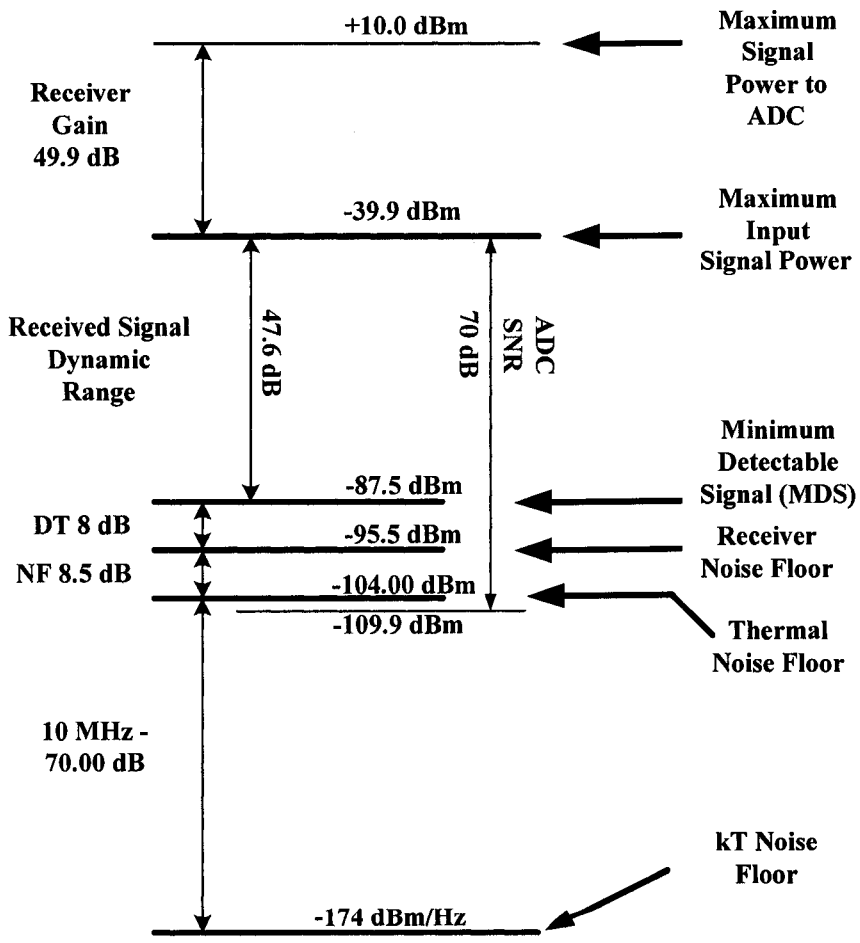

Figure 3.23: Receiver sensitivity and maximum signal input

3.5 PCB OrCAD layout

Once the components were identified for the burst transceiver PCB, the layout for the PCB was created using FreePCB. FreePCB is a free, open-source printed circuit board layout editor for Microsoft Windows, released under the GNU General Public License. It can be used to create 1-8 copper layer boards with sizes upto 60 inches × 60 inches. The final layout of the burst transceiver is shown in Figure 3.24. It is a 4 layer board, with the top and bottom layers used for signal routing and the intermediate layers are used as power and ground planes. All the surface mount components are placed on the top layer of the board. The board dimension is 15.3 cm × 41.8722 cm. The left half of the board consists of the transmit path and the right half of the board has the receive and the LO sections. Care was taken to make sure that the traces have no sharp corners. It was also made sure that inductors are placed perpendicular to each other in order to avoid coupling of energy between them. The trace width had to be optimized to give 50 ohm impedance. The relationship between trace dimensions and the impedance Z_o can be given by the following equation

$$Z_o = \frac{87}{\sqrt{\varepsilon_r + 1.41}} \cdot \ln\left(\frac{5.98H}{0.8W + T}\right) \qquad \textbf{Equation 3-12}$$

For an impedance of 50 ohms, dielectric thickness (H)= 10 mils, trace thickness (T)=1.5oz, dielectric permittivity of FR-4 (ε_r)=4.35, the trace width was calculated as 16.29 mils. However, due to the presence of components with very fine pitch and the required minimum distance between traces of 5 mils, the trace width was limited to 12 mils which gives an impedance of 59.37 ohms. Once the layout was complete, gerber files were generated and sent over to Cirexx International, Santa Clara, CA for fabrication and assembly.

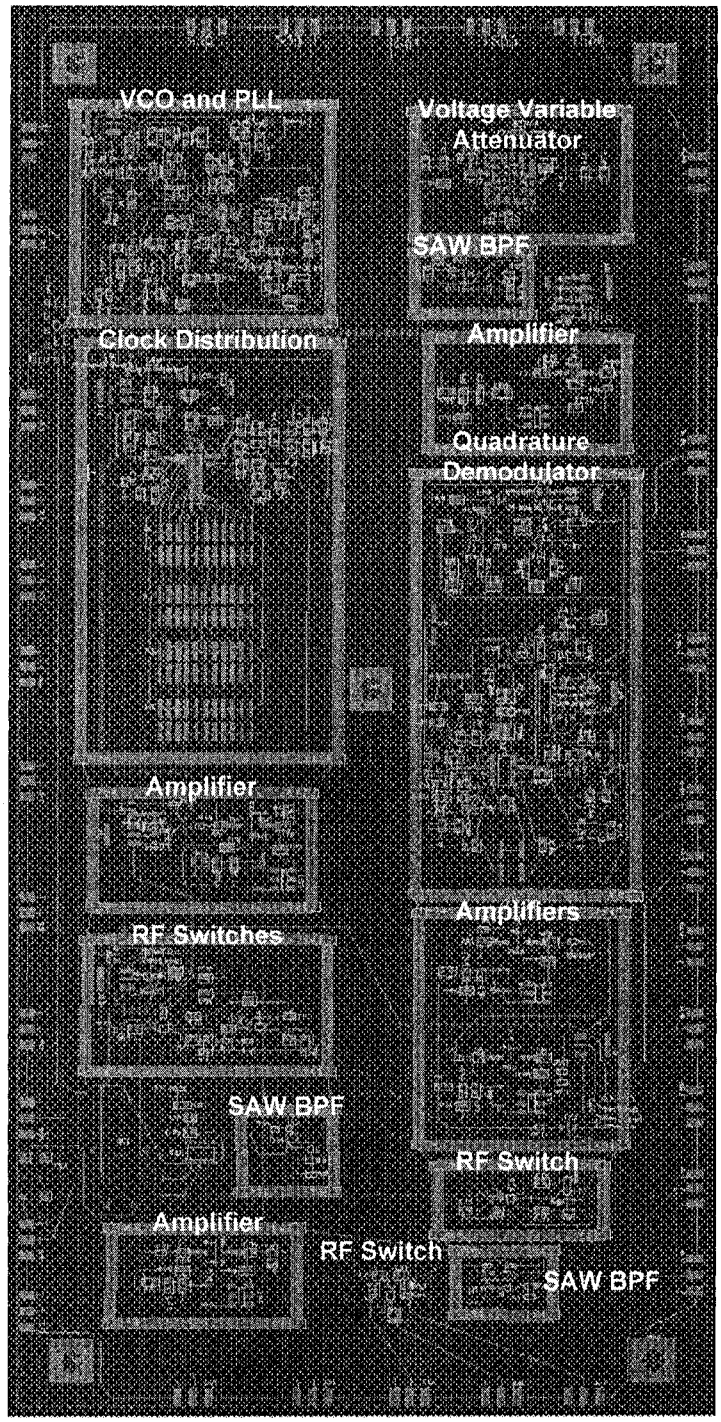

Figure 3.24: Burst transceiver PCB layout

3.6 Burst transceiver PCB – test results

3.6.1 Transmitter gain and noise figure

A processing stage based block diagram of the transmit path on the PCB is shown in Figure 3.25. A cascaded gain and noise figure analysis of the expected performance during the burst signal transmission is shown in Table 3.4. Included in this table is the measured performance when a continuous signal is transmitted. The expected and measured performances track each other well, with a buffered output power between +12 to +14 dBm driving the antenna. In this case, the gain control attenuator is not required as in the prototype transceiver since the amplifiers used in the transmit path only provide a 10 dB gain and hence the signal level at the input of the T/R switch will not exceed the maximum specified rating of +27 dBm. Figure 3.26 shows the spectrum of the CW signal at the output of the transmitter measured using a real time spectrum analyzer RSA3303 from Tektronix. It can be seen that the frequency is 434.395 MHz with the power level at +12.29 dBm.

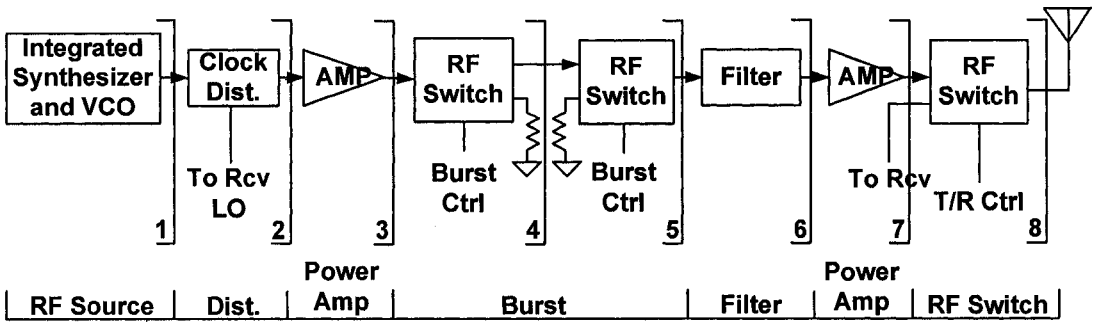

Figure 3.25: Transmitter processing stages

Table 3.4: Cascaded gain and noise figure analysis of transmitter when transmitting

Stage	1	2	3	4	5	6	7	8
Gain (dB)			10.50	-0.90	-0.90	-3.00	10.50	-0.90
Noise Figure (dB)			3.60	0.90	0.90	3.00	3.60	0.90
Noise Figure (linear)		1.00	2.29	1.23	1.23	2.00	2.29	1.23
Total Gain (dB)		0.00	10.50	9.60	8.70	5.70	16.20	**15.30**
Total Gain (linear)		1.00	11.22	9.12	7.41	3.72	41.69	33.88
Total Noise Figure (linear)		1.00	2.29	2.31	2.34	2.47	2.82	2.82
Total Noise Figure (dB)		0.00	3.60	3.64	3.69	3.93	4.50	**4.51**
Expected Signal Power (dBm)	-5.00	-1.80	8.70	7.80	6.90	3.90	14.40	13.50
Measured Signal Power (dBm)	-5.00	-1.80	7.97		5.00	3.90	12.60	12.29

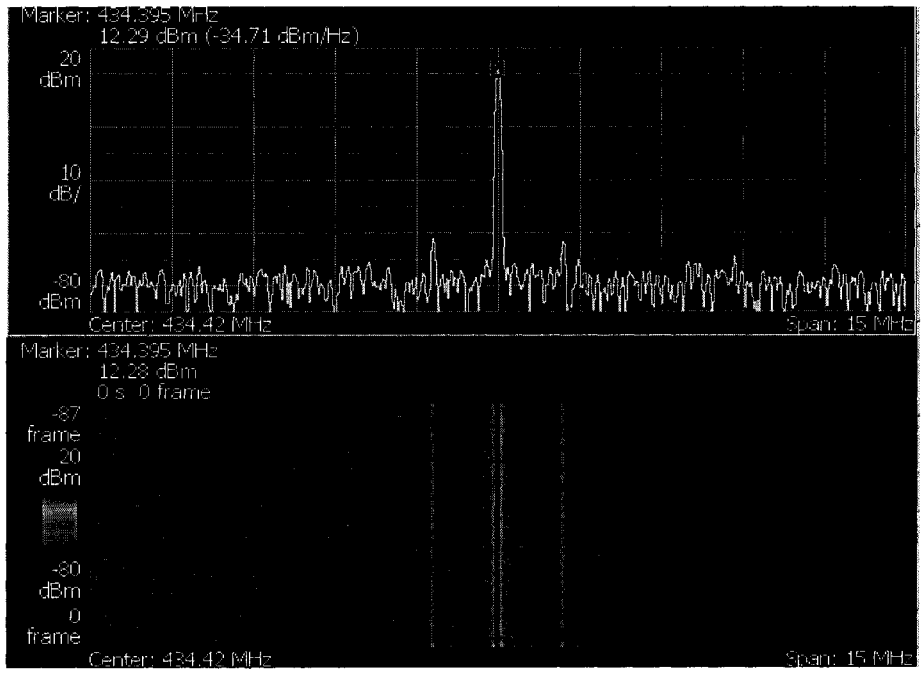

Figure 3.26: Transmitter CW output (12.29dBm at 434.395 MHz) measured using RSA3303 real-time spectrum analyzer

3.6.2 Receiver gain and noise figure

A processing stage based block diagram of the prototype receiver is shown in Figure 3.27. Based on the components selected, the signal and noise power levels for the design can be computed as shown in Table 3.5. The receiver with a 10 MHz passband is

designed to have a cascaded gain of 49.9 dB when both the amplifiers are operating in the receive chain and a receiver noise figure of approximately 8.76 dB.

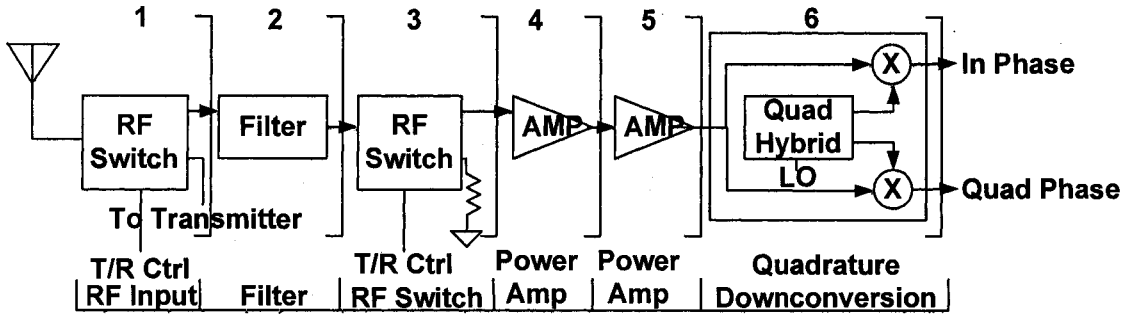

Figure 3.27: Receiver processing stages

Table 3.5: Cascaded gain and noise figure analysis of receiver when receiving

Stage	1	2	3	4	5	6
Gain (dB)	-0.90	-3.00	-0.90	10.50	10.50	33.70
Noise Figure (dB)	0.90	3.00	0.90	3.60	3.60	10.5
Noise Figure (linear)	1.23	2.00	1.23	2.29	2.29	11.22
Total Gain (dB)	-0.90	-3.90	-4.80	5.70	16.20	**49.90**
Total Gain (linear)	0.81	0.41	0.33	3.72	41.69	97723.72
Total Noise Figure (linear)	1.23	2.45	3.02	6.92	7.27	7.51
Total Noise Figure (dB)	0.90	3.90	4.80	8.40	8.61	**8.76**
Expected Signal Power (dBm)	-20.90	-23.90	-24.80	-14.30	-3.80	29.90
Measured Signal Power (dBm)					-4.00	

Also, the expected and measured signal powers at the output of receive amplifiers is shown as part of Table 3.5. Thus the power level at the input of the quadrature mixer stage is around -4 dBm.

3.6.3 Useful operating range of the burst transceiver

Frii's transmission equation can be used to determine the range R of the burst transceiver PCB, which defines the distance over which the burst transceiver can successfully communicate with and process responses from the SAW sensor. Frii's

transmission equation can be written as

$$\frac{P_r}{P_t} = G_t G_r \left(\frac{\lambda}{4\pi R}\right)^2 \frac{1}{L} \qquad \textbf{Equation 3-13}$$

where P_r and P_t are the received and transmitted power respectively, G_t and G_r are the transmit and receive antenna gains, λ is the wavelength, R is the distance between the transmitter and receiver and L is the system loss factor. For the burst transceiver we know that the transmit power is 12 dBm and the minimum detectable receive signal is ~-80 dBm. This gives an estimate of the total loss (2-way path loss+SAW device loss) to be 92 dB. Assuming a SAW device loss of 10 dB, the 1-way path loss can be calculated to be 41 dB.

Assuming the antenna gains and the system loss factor to be unity, Equation 3-13 can be rewritten as

$$PathLoss(dB) = 32.44 + 20 \cdot \log_{10} f(MHz) + 20 \cdot \log_{10} R(Km) \qquad \textbf{Equation 3-14}$$

For a path loss of 41 dB and a frequency of 434.42 MHz, the above equation gives the range R as 6.6m.

3.6.4 Burst transmission tests

Once the transmit, receive and LO sections were tested in terms of the relative signal levels and frequency, burst transmission tests were conducted by generating a 434.42 MHz burst with a duration of 500ns. The burst timing control was provided by the Spartan II FPGA that was used to program the PLL. Figure 3.28 shows the burst signal in time domain along with the control signal that was used to generate the burst. In Figure 3.29, the same burst is measured using the RSA3303 real time spectrum analyzer. The left half of the Figure shows the signal power in time domain. From this Figure, it is clear that for the burst duration of 500ns the signal power level is +12 dBm. The right half of the figure shows the spectrum of the signal collected for a duration of 40 μs. Additional experimental details of the passive wireless SAW system and the results obtained will be discussed at length in chapter 6.

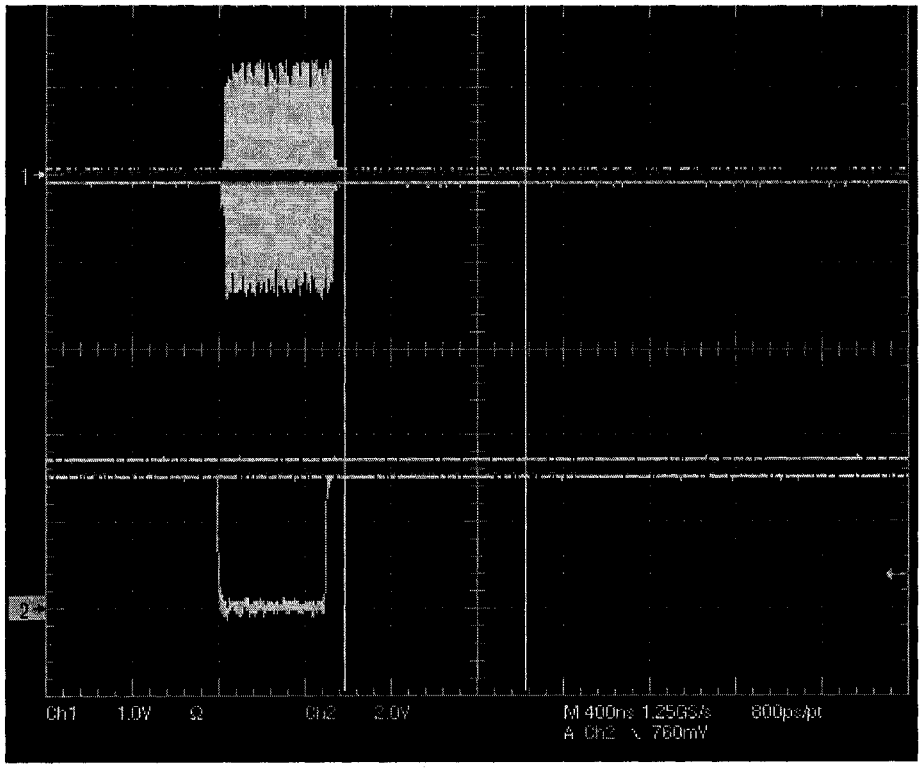

Figure 3.28: Burst signal for sensor interrogation

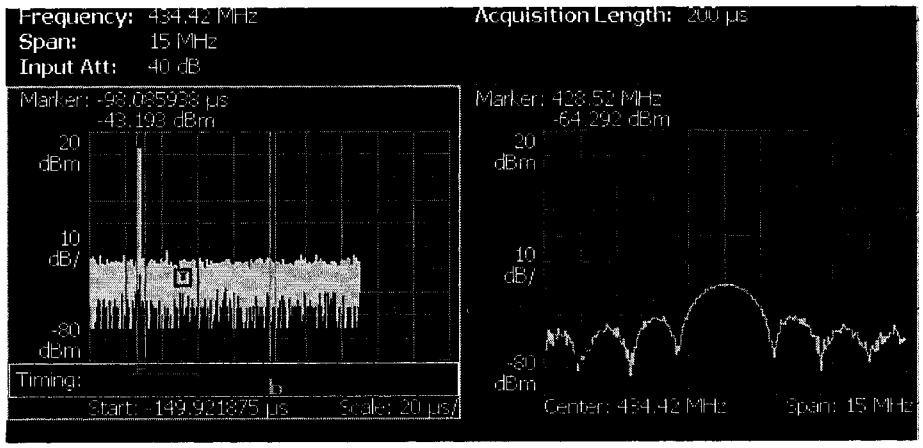

Figure 3.29: Burst captured using the RSA3303 real-time spectrum analyzer

3.7 Summary

This chapter presented a detailed description of the prototype as well as PCB

burst transceiver from the block diagram down to the cascaded gain and noise figure analysis. Initial tests were run on the prototype burst transceiver after which the burst transceiver PCB was designed, fabricated and tested. CW and burst tests were performed on the transceivers and the spectrum of the SAW sensor interrogation signal measured at the output of the transmit path was shown. The next chapter deals with the design, modeling and simulation of SAW sensors using MATLAB™ and CoventorWare™. Further results obtained from the passive wireless SAW system will be discussed in chapter 6.

CHAPTER IV

SAW DEVICES: DESIGN, MODELING AND SIMULATION

4.1 Introduction

This chapter deals with the design aspects, modeling and simulation of SAW devices using CoventorWare™ (CW), MATLAB™ and Orcad Capture CIS™. CW is a 3-Dimensional modeling and simulation package which makes use of the DESIGNER and ANALYZER modules to model and analyze the structure. The DESIGNER module was used to create 2-Dimensional layouts and 3-Dimensional models and the ANALYZER module was used to perform finite element (FE) steady-state or transient analysis on the 3D models. In MATLAB™, the SAW devices were simulated using the transmission matrix approach, in which the frequency response of the SAW device is computed by multiplying the transmission matrices corresponding to each element of the SAW device namely the IDTs, gratings and the acoustic transmission line. Boundary conditions are then applied to these matrices to determine an expression for the insertion loss of the devices. In Orcad Capture CIS™, the Mason's equivalent circuit was used to represent individual metallized and free sections on the substrate. These circuits were then cascaded to obtain the equivalent circuit for the entire transducer. Steady state analysis was then performed to determine the frequency response of the SAW devices. This chapter provides detailed information regarding the modeling and simulation of the frequency response of SAW devices using the three software packages.

4.2 Design aspects of SAW sensors

Figure 4.1 shows a schematic of the SAW IDT with the various design parameters. The same notation will be used throughout the rest of this dissertation. The

SAW wavelength is denoted by λ and the overlap between adjacent fingers which is called the acoustic aperture will be represented by W. The metallization ratio (η) is defined as the ratio between the width of the fingers (a) and the spacing between fingers (b).

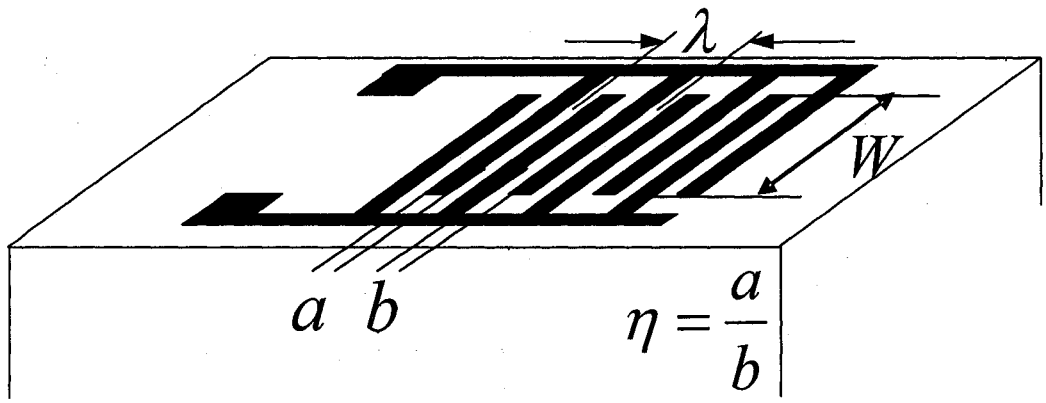

Figure 4.1: SAW IDT depicting the various design parameters

SAW delay line and two-port resonators were designed to operate at 100 MHz center frequency on Y-cut Z-propagating Lithium Niobate (YZ-$LiNbO_3$) by defining values for each of the above design parameters. For the delay lines, the input IDT was designed in order to achieve the desired frequency characteristics and the output IDT was made wideband and therefore does not alter the frequency response obtained using the input IDT. The number of finger pairs in the input and output IDT were chosen to be 50 and 10 respectively. The velocity of Rayleigh wave on YZ-$LiNbO_3$[133] is 3488 m/s and therefore for a center frequency of 100 MHz, the SAW wavelength (λ) is 34.88 μm. The width of the fingers (a) was designed to be 8.72 μm (quarter wavelength) and the metallization ratio (η) was chosen to be 0.5. The metallization height (h) was selected as 200 nm giving h/λ=0.573%, in order to minimize the reflections between the fingers of an IDT. The center to center separation between input and output IDTs of the delay line (d) was chosen to be 100λ in order to obtain a delay of 1μs. The acoustic aperture (W) was maintained at 80λ in order to minimize the substrate area and also the finger resistance.

For the SAW two-port resonators, the number of reflectors was chosen to be 500 in order to get the maximum Q as possible while at the same time minimizing the propagation loss in the region between the reflectors[134]. For shorted Aluminum reflectors, it has been established experimentally by Cross that for efficient coupling of the standing wave to the transducer, the distance between the IDT and the grating should be $\left(\frac{m}{2}+\frac{1}{8}\right)\lambda_o$ where m is any integer[134]. For our specific design, m=7 giving the distance between the IDT and grating to be $3.625\lambda_o$. The IDT to IDT distance was chosen to be $10\lambda_o$.

4.3 SAW sensor modeling and simulation results

4.3.1 3D finite element modeling using CoventorWare™

The sequence of steps that were followed in creating a 3D model of the SAW device is as follows. First, the properties for the materials to be used in the structure were entered into the material properties database (MPD)[135]. The MPD in CW comes with the material properties of most commonly used materials. However, in some cases, these have to be entered by the user. The only materials that are required to model the SAW device are Lithium Niobate ($LiNbO_3$) and Aluminum thin film. The most critical properties to be specified for piezoelectric materials are stiffness matrix [C], piezoelectric-stress coupling matrix [e], electrical permittivity matrix [ε] and density [ρ]. For the trigonal 3m crystal symmetry class, these matrices are as follows[136]:

$$c=\begin{bmatrix} c11 & c12 & c13 & c14 & 0 & 0 \\ c12 & c11 & c13 & -c14 & 0 & 0 \\ c13 & c13 & c33 & 0 & 0 & 0 \\ c14 & -c14 & 0 & c44 & 0 & 0 \\ 0 & 0 & 0 & 0 & c44 & c14 \\ 0 & 0 & 0 & 0 & c14 & (c11-c12)/2 \end{bmatrix}$$

$$e = \begin{bmatrix} 0 & 0 & 0 & 0 & ex5 & -ey2 \\ -ey2 & ey2 & 0 & ex5 & 0 & 0 \\ ez1 & ez1 & ez3 & 0 & 0 & 0 \end{bmatrix}$$

$$\varepsilon^S = \begin{bmatrix} \varepsilon^S_{xx} & 0 & 0 \\ 0 & \varepsilon^S_{yy} & 0 \\ 0 & 0 & \varepsilon^S_{zz} \end{bmatrix}$$

The following values were used for $LiNbO_3$[136]

$$C = \begin{bmatrix} 203000 & 53000 & 75000 & 0 & 0 & 9000 \\ 53000 & 203000 & 75000 & 0 & 0 & -9000 \\ 75000 & 75000 & 245000 & 0 & 0 & 0 \\ 0 & 0 & 0 & 75000 & 9000 & 0 \\ 0 & 0 & 0 & 9000 & 60000 & 0 \\ 9000 & -9000 & 0 & 0 & 0 & 60000 \end{bmatrix} \mu N / \mu m^2$$

$$e = \begin{bmatrix} 0 & 0 & 0 & -2.5 & 3.7 & 0 \\ -2.5 & 2.5 & 0 & 0 & 0 & 3.7 \\ 0.2 & 0.2 & 1.3 & 0 & 0 & 0 \end{bmatrix} pC / \mu m^2$$

$$\varepsilon^S = \begin{bmatrix} 84 & 0 & 0 \\ 0 & 84 & 0 \\ 0 & 0 & 30 \end{bmatrix}$$

$\rho = 4.7 \times 10^{-15}$ kg/μm^3

Care was taken while entering the values in CW to ensure that the subscript ordering is consistent with the handbook used for these values. Once the material properties are stored in the MPD, the fabrication sequence was specified in the process editor[135]. Figure 4.2 shows a screenshot of the process editor showing the fabrication sequence. To begin with, a delay line with just 4 finger pairs in the input and output IDT and a center frequency of 100 MHz was simulated in order to reduce computational time and also verify the validity of the model. The acoustic aperture was maintained at 80 μm and the spacing between the IDTs was 130 μm. The depth of the substrate used in

simulations was only 50 μm compared to the 500 μm in the fabricated devices. This was done in order to reduce computational time. Since most of the energy of the SAW is concentrated within one wavelength (34.88 μm) depth of the device, the effect of the reduced depth on the frequency response of the devices is minimal. The metallization thickness for the IDTs was chosen to be 200nm which is the same as that used for the fabrication process. After the process sequence is defined, the 2-Dimensional mask patterns required for the SAW delay line are drawn using the layout editor as shown in Figure 4.3. Figure 4.3(a) shows the acoustic aperture and also the overall width of the device to be 2790 μm and 750 μm approximately. Figure 4.3(b) shows the separation between the IDT and the wavelength to be 130.8 μm and 34.88 μm respectively.

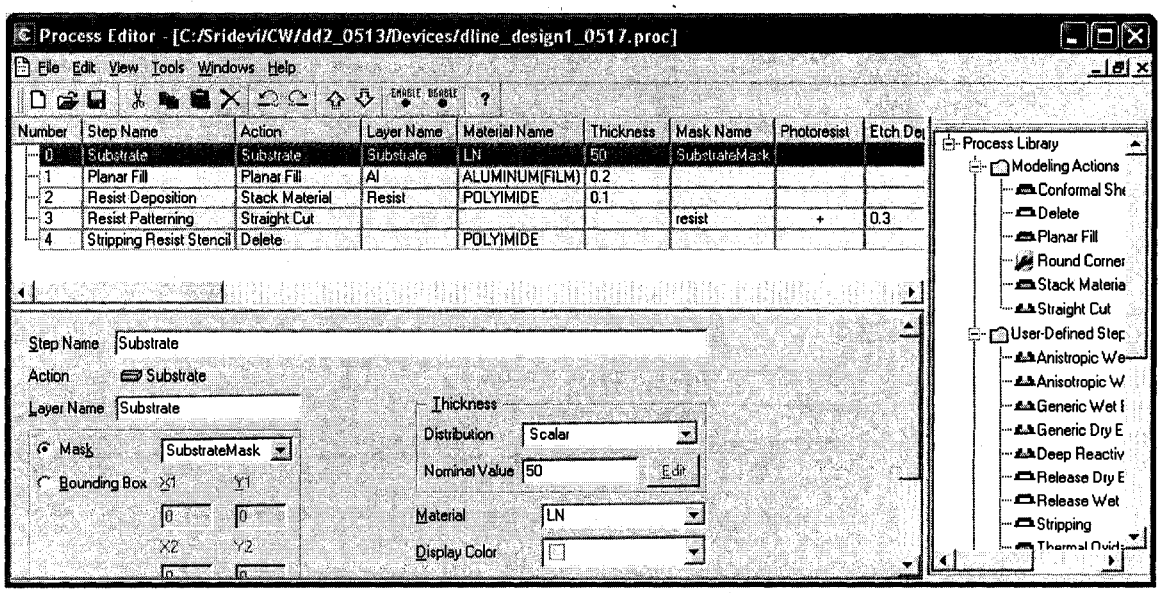

Figure 4.2: Fabrication sequence in the Process Editor

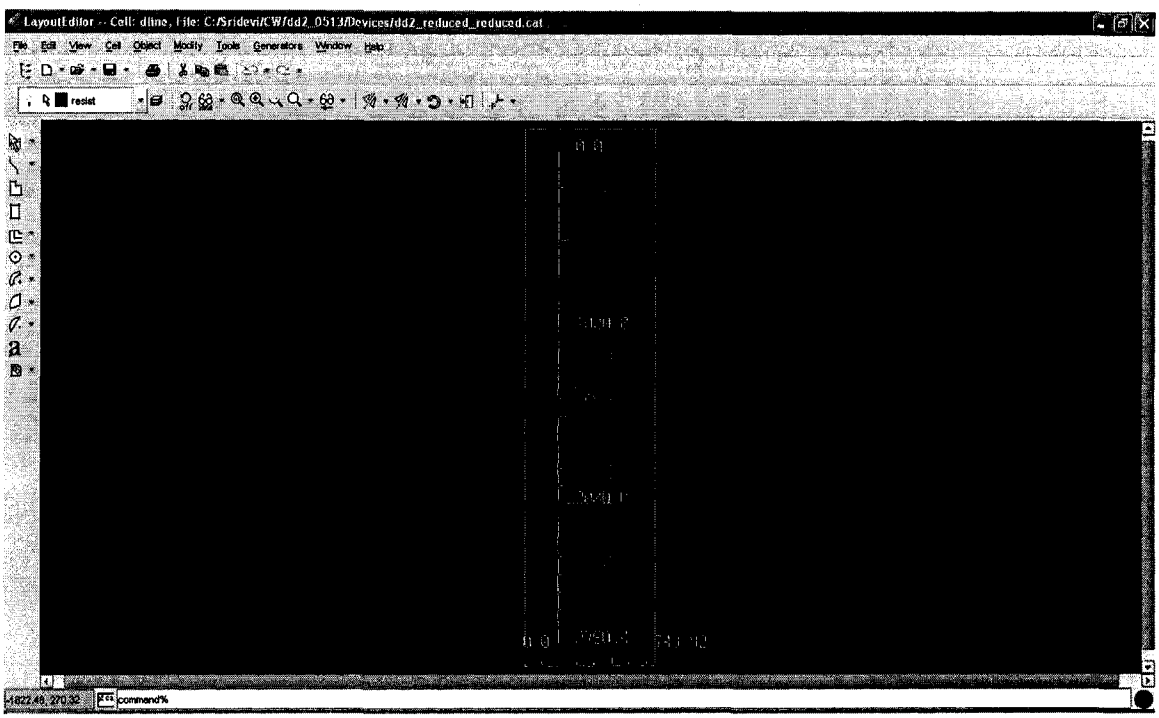

(a)

(b)

Figure 4.3: Mask layout in the Layout Editor (a) view showing the acoustic aperture to be 2790 μm (b) zoomed in view showing IDT separation=130.8 μm and λ=34.88 μm

Following this, the 3-Dimensional model is created and meshed using the Preprocessor. The meshed model was then rotated in the Preprocessor in order to obtain the required orientation (Y-cut, Z-propagating) of the substrate. The material properties of the device can also be edited using the Preprocessor. A tetrahedral mesh parabolic mesh was chosen since it can effectively model the anisotropic behavior of the substrate and also the parabolic elements have more number of nodes per element when compared

to the linear elements. Figure 4.4 shows the meshed delay line element size of 40 μm giving a total of 42642 elements for the entire 3-Dimensional structure. While in Preprocessor, it is required to name the patches on which boundary conditions will be applied prior to solving. For example, the input, output, ground fingers and also the bottom and sides of the substrate have to be named appropriately. The three dimensional structure was now ready for analysis.

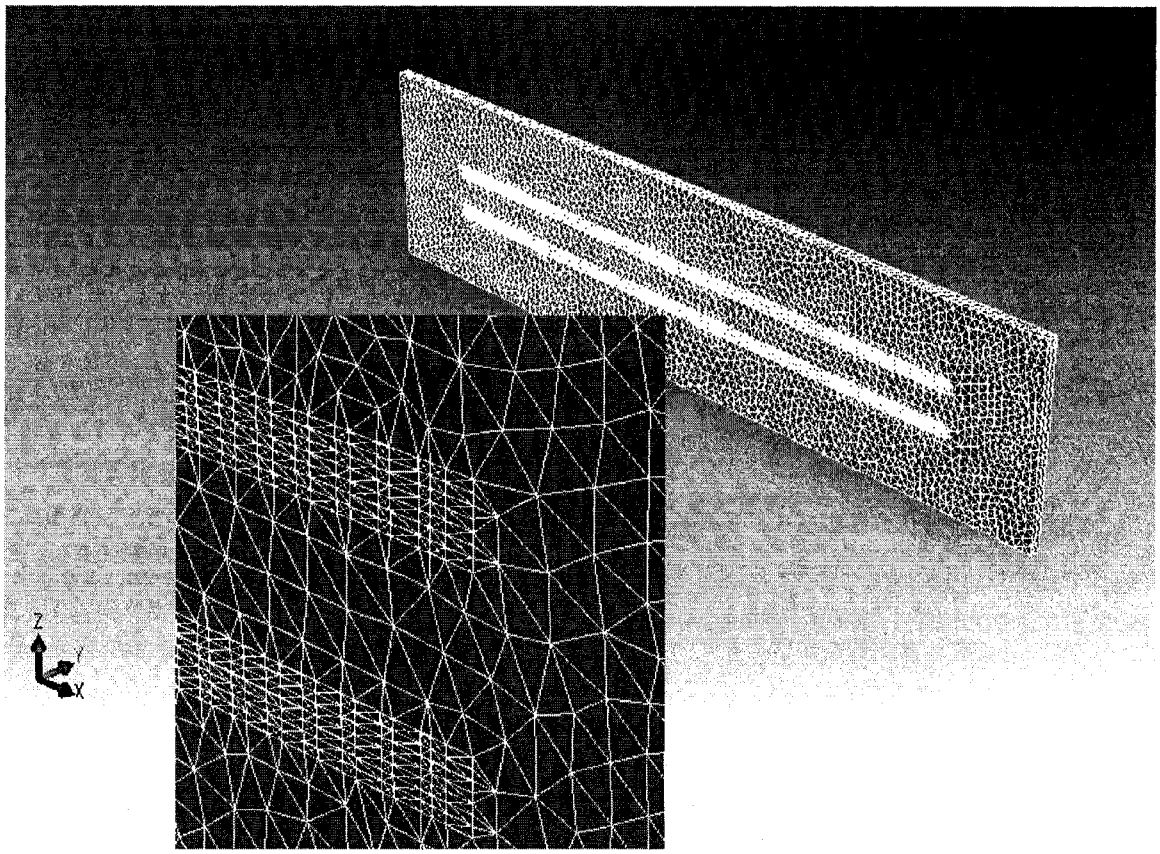

Figure 4.4: Meshed 3D view of the SAW delay line in Preprocessor

Once the 3-Dimensional structure was modeled using CW Designer, the analysis is run using CW Analyzer. A piezoelectric transient analysis was setup using the MemMech module available in the Analyzer. MemMech can be used for performing piezoelectric analysis involving voltage in-strain out or strain in-voltage out problems.

The direct piezoelectric effect is the creation of electric polarization due to mechanical stress. Closely related to it is the converse effect, where strain in a crystal is developed due to application of an electric field. Stress is developed when deformation is prevented or restrained by the surrounding materials. CW takes this effect into consideration and assumes the linear coupling relationship between electric displacement or electric field strength and mechanical factors such as strain and stress components. The piezoelectric constitutive equations are given by[135]

$$T_{ij} = c_{ijkl}^{E} S_{kl} - e_{kij} E_k \qquad \textbf{Equation 4-1}$$

$$D_i = e_{ikl} S_{kl} + \varepsilon_{ik}^{S} E_k \qquad \textbf{Equation 4-2}$$

where T_{ij} are the stress components, c_{ijkl}^{E} are the elastic constants of the substrate used, S_{kl} is the strain, E_k is the electric field intensity, e_{ikl} are the piezoelectric constants of the substrate, ε_{ik}^{S} is the permeability. These equations are solved together with Maxwell's equations and the mechanical equations of motion to obtain a solution for the piezoelectric problem. Assuming that the surrounding medium has lower dielectric constant when compared to the substrate, these equations can be solved independently in the domain of the substrate[137]. Since the acoustic waves are five orders of magnitude slower than the electromagnetic waves, the piezoelectrically coupled field is assumed as quasistatic and the Maxwell's equations can be written as[137]

$$\frac{\partial D_i}{\partial x_i} = 0 \qquad \textbf{Equation 4-3}$$

$$E_i = -\frac{\partial \phi}{\partial x_i} \qquad \textbf{Equation 4-4}$$

where D_i are the components of electric displacement and ϕ is the electric potential. Assuming the piezoelectric substrate to be a perfect insulator, the electric charge inside is assumed to be zero. The equations of motion in the absence of internal body forces therefore become

$$\frac{\partial T_{ij}}{\partial x_j} - \rho \frac{\partial^2 u_i}{\partial t^2} = 0 \qquad \textbf{Equation 4-5}$$

where ρ is the mass density and u_i are the components of displacement. The strain components are defined by

$$S_{ij} = \frac{1}{2}\left(\frac{\partial u_i}{\partial x_j} + \frac{\partial u_j}{\partial x_i}\right) \qquad \textbf{Equation 4-6}$$

Combining Equations 4-1, 4-2, 4-4 and 4-6 and substituting the results in Equations 4-3 and 4-5, we get the following set of equations:

$$-\rho \frac{\partial^2 u_i}{\partial t^2} + c^E_{ijkl} \frac{\partial^2 u_k}{\partial x_j \partial x_l} + e_{kij} \frac{\partial^2 \phi}{\partial x_k \partial x_j} = 0 \qquad \textbf{Equation 4-7}$$

$$e_{ikl} \frac{\partial^2 u_k}{\partial x_i \partial x_l} - \varepsilon^S_{ik} \frac{\partial^2 \phi}{\partial x_i \partial x_k} = 0 \qquad \textbf{Equation 4-8}$$

The above system of equations is then discretized and boundary conditions are applied in order to obtain the solution for each time step.

In our analysis, an impulse of magnitude 1×10^9 volts and duration of 1 nsec was applied to one set of fingers in the input IDT. One set of fingers in the input and output IDT were grounded. The four sides and the bottom of the substrate were fixed in order to eliminate reflection of acoustic waves from the sides of the substrate. In addition the bottom of the substrate was grounded in order to reduce electromagnetic coupling between the input and output IDTs. The analysis was performed for a total of 50 ns with a time step of 1ns. Since the propagation time of the SAW between the input and output IDT for the model shown in Figure 4.4 is approximately 37 ns, this simulation time can only show the effects of single transit and the influence of triple transit cannot be observed.

4.3.2 CoventorWare™ simulation results

Once the analysis was completed, the average voltage on the input and output IDTs was obtained as a function of time. Further analysis was performed in MATLAB™

to yield the frequency response of the device. Figure 4.5 shows the frequency response of the delay line. From the figure, it can be seen that the center frequency of the device is close to 100 MHz. In addition, the simulation results do not show any characteristic response beyond 300 MHz. This may be due to the insufficient density of nodes. Since the simulation does not model the effect of source and load impedance and any matching networks, the frequency response should be appropriately scaled when comparison with measured responses are required.

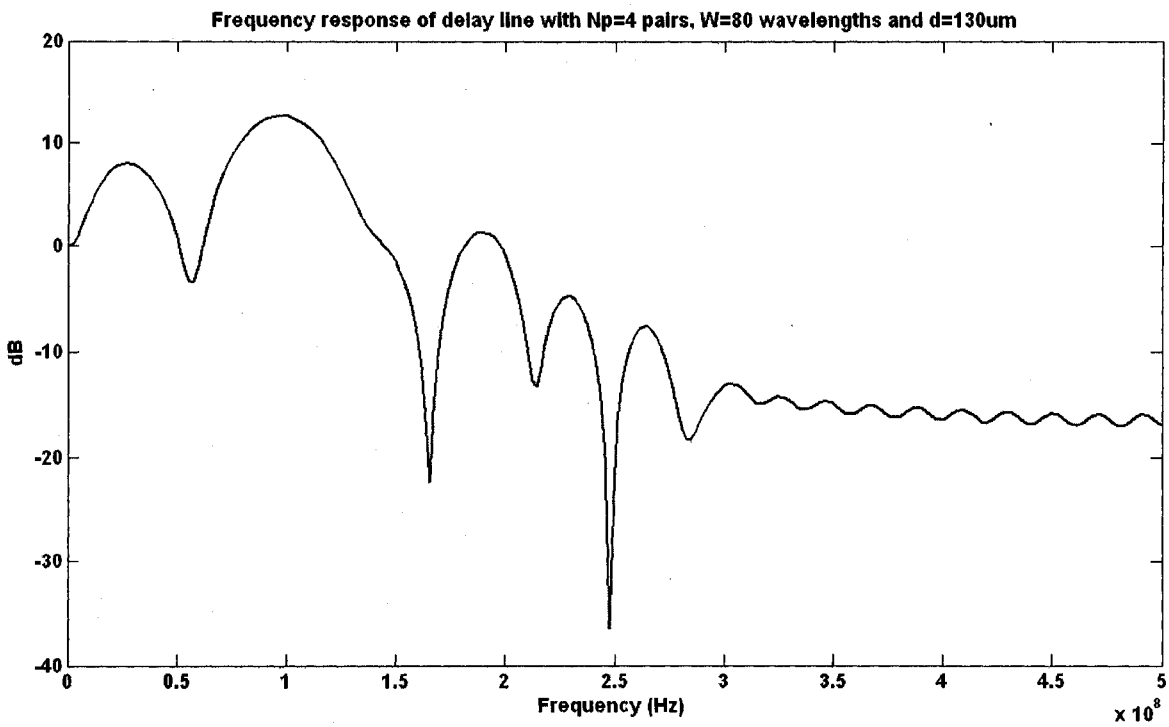

Figure 4.5: Delay line frequency response simulated in CoventorWare^{TM}

In addition to the frequency response, displacements along the three directions were also plotted for a duration of 50ns. This is shown in Figure 4.6. From the Figure, it is clear that the dominant displacements are in the y- and z- directions confirming the existence of Rayleigh waves. Figure 4.7 shows a three dimensional view of the wave

propagation on the substrate at (a) 35ns and (b) 49 ns. In Figure 4.7(a), the wave has just reached the output IDT whereas in Figure 4.7(b), the wave has traveled beyond the fingers defining the output IDT. By looking at the figure, it is clear that the wave is propagating along the z-direction. It can be observed that the acoustic wave is bidirectional since a portion of the acoustic energy from the input IDT also travels in the opposite direction and reached the edges of the substrate.

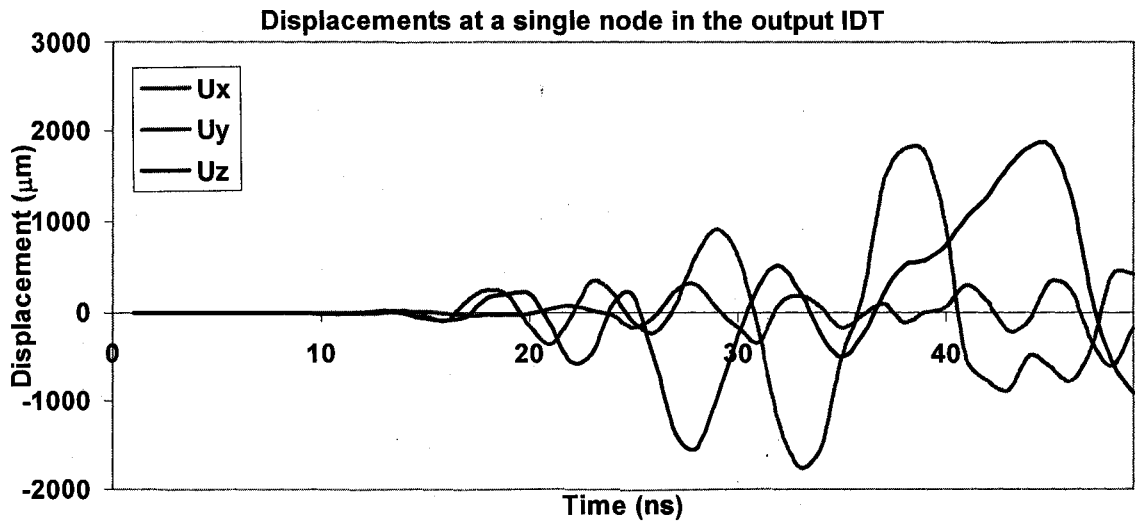

Figure 4.6: Displacements measured at a single node in the output IDT of the SAW device

Once the model was validated using the above results, a delay line with center frequency of 100 MHz, Np1=50, Np2=15, W=80λ and d=10λ was simulated using brick elements with mesh size of 175 μm, 10 μm and 4.36 μm in the x-, y- and z- directions respectively giving a total of 71608 elements. A transient analysis was conducted for a total of 300 ns by applying an impulse of magnitude 1×10^{9} volts for a duration of 1 ns. The sides of the substrate and the bottom were fixed to eliminate reflections and also the bottom of the substrate was grounded to minimize electromagnetic feedthrough.

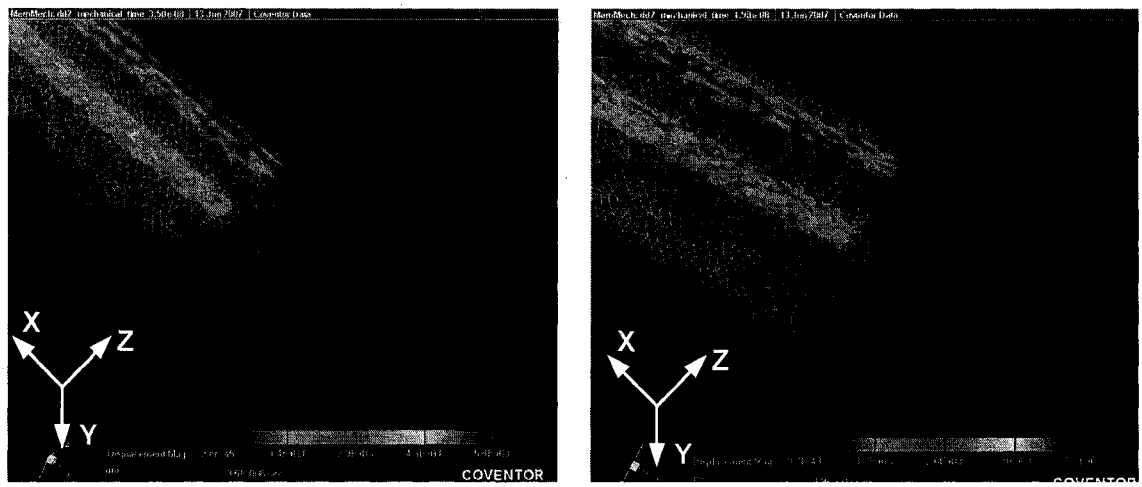

(a) **(b)**

Figure 4.7: Three dimensional view of the wave propagation on the substrate (a) 35 ns and (b) 49 ns

Figure 4.8 shows the frequency response obtained from the analysis. Although there is a characteristic peak at 100 MHz there is also a stronger signal close to 150 MHz probably due to the presence of bulk waves. Optimizing the mesh model for this device is currently under investigation in order to obtain a good match with the measured responses.

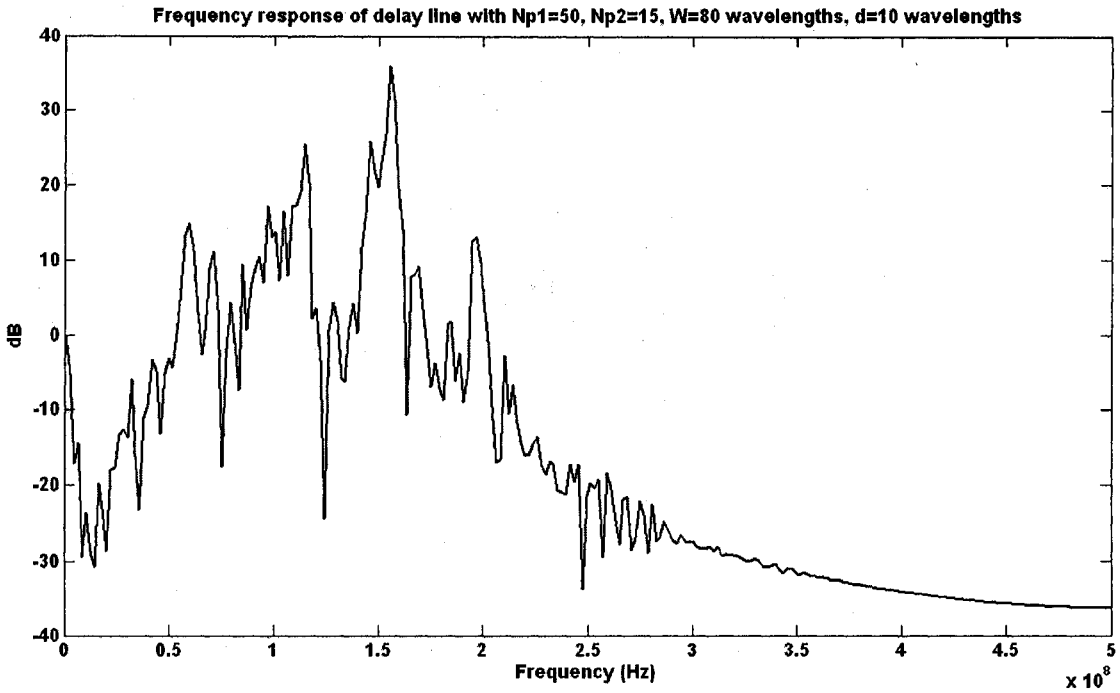

Figure 4.8: Frequency response comparison of delay line with Np1=50, Np2=15, W=80λ, d=10λ

4.3.3 SAW device modeling using MATLAB™

The frequency response of SAW devices was simulated in MATLAB™ using the transmission matrix approach by cascading the 2×2 acoustic transmission matrix corresponding to each element of the SAW device[138]. The element can be either an IDT, grating or the transmission line. The transmission matrix related the amplitudes of the forward and backward traveling waves on the left side of each element to those on the right side (see Figure 4.9). Therefore, the following vector notation will be used in the remainder of the section to represent the amplitudes of the acoustic wave at the right hand reference plane of each element of the SAW device.

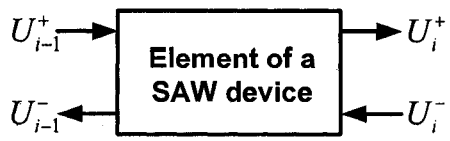

Figure 4.9: Acoustic wave amplitudes on either side of an element of the SAW device

$$U_i = \begin{bmatrix} U_i^{+} \\ U_i^{-} \end{bmatrix}$$ **Equation 4-9**

Here the '+' an '-'signs represent the forward and backward traveling acoustic waves. The transmission matrices will be defined for the IDT, grating and the acoustic transmission line and will be used to derive an expression for the frequency response of different SAW devices. In the next section, simulation results will be presented using the design parameters from the fabricated SAW devices.

Figure 4.10 shows the schematic of an IDT depicting the two acoustic ports and one electrical port. The overall transmission matrix for an IDT can be written as

$$\begin{bmatrix} U_{i-1}^{+} \\ U_{i-1}^{-} \\ I \end{bmatrix} = \begin{bmatrix} t_{11} & t_{12} & t_{13} \\ t_{21} & t_{22} & t_{23} \\ t_{31} & t_{32} & t_{33} \end{bmatrix} \begin{bmatrix} U_i^{+} \\ U_i^{-} \\ V \end{bmatrix}$$ **Equation 4-10**

The subscripts 1 and 2 in the transmission matrix refer to the acoustic ports and the subscript 3 refers to the electrical port.

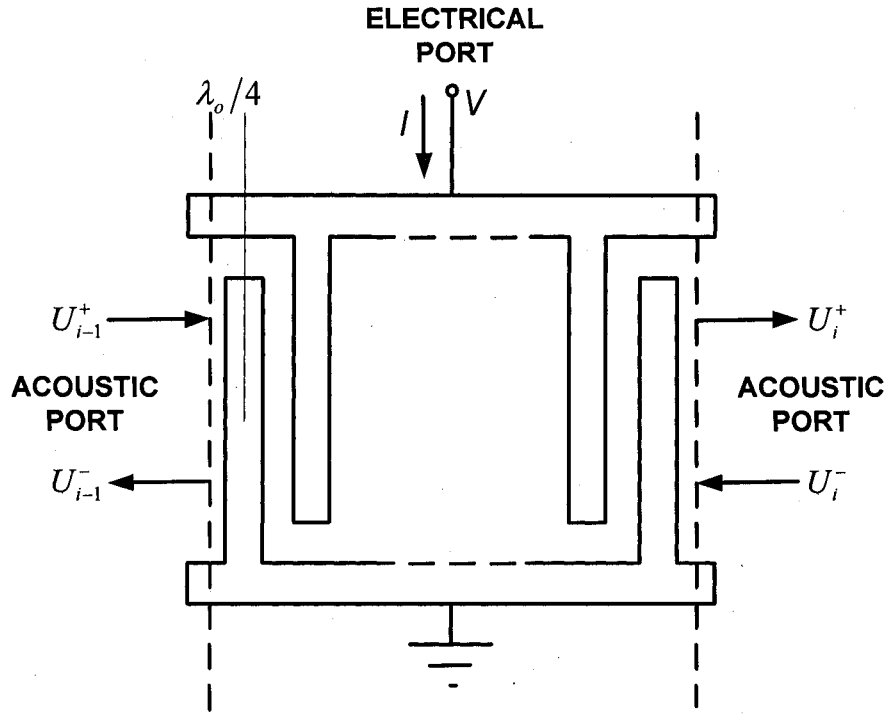

Figure 4.10: Schematic of an IDT depicting two acoustic ports and one electrical port

The overall transmission matrix for the IDT given by Equation 4-10 is obtained by cascading the transmission matrix for each finger. The schematic for a single finger in the IDT is shown in Figure 4.11. It consists of metallized and free sections with impedance and velocity of Z_m, V_m and Z_o, V_o respectively.

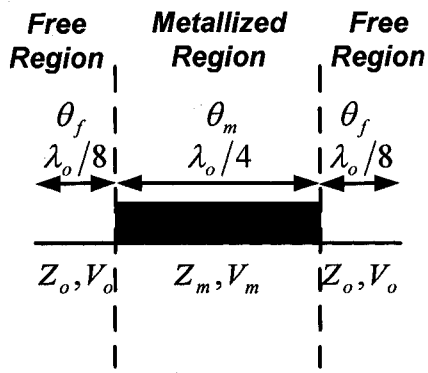

Figure 4.11: Schematic of a single finger in the IDT

The value of the velocity for the metallized section can be written as

$$V_m = \frac{\lambda_o}{4}\frac{1}{\frac{1}{2f_a}-\frac{1}{4f_o}}$$

where f_a is the average shifted center frequency and is given by

$$f_a = \frac{V_a}{\lambda_o} = \frac{V_o\left(1-k_{11}^{'}\right)}{\lambda_o}$$

where $k_{11}^{'}$ is the normalized self coupling coefficient and V_a is the average shifted velocity due to metallization. The impedances can now be expressed as

$$Z_o = \frac{1}{f_o C_S K^2} \text{ and } Z_m = \frac{1}{f_m C_S K^2}$$

In the above equation, C_s and K^2 are the capacitance of a finger pair and electromechanical coupling coefficient respectively and depend on the specific substrate used. The three-port matrix for a single finger is given by the following equation:

$$\begin{bmatrix} U_1^+ \\ U_1^- \\ I_3 \end{bmatrix} = \begin{bmatrix} t_{11} & t_{12} & t_{13} \\ t_{21} & t_{22} & t_{23} \\ t_{31} & t_{32} & t_{33} \end{bmatrix} \begin{bmatrix} U_2^+ \\ U_2^- \\ V_3 \end{bmatrix} \qquad \textbf{Equation 4-11}$$

The subscripts 1 and 2 refer to the acoustic ports and the subscript 3 refers to the electrical port. The individual elements of the T matrix are given by[139, 140]

$$t_{11} = \frac{1}{2}\left(2A_{se} + \frac{B_{se}}{Z_o} + Z_o C_{se}\right)$$

$$t_{12} = \frac{1}{2}\left(Z_o C_{se} - \frac{B_{se}}{Z_o}\right)$$

$$t_{13} = \frac{1}{2Z_e} j \tan\frac{\theta_e}{2}\sqrt{Z_o}\left(-A_{se} - 1 - \frac{B_{se}}{Z_o}\right) \qquad \textbf{Equation 4-12}$$

$$t_{21} = -t_{12}$$

$$t_{22} = \frac{1}{2}\left(2A_{se} - \frac{B_{se}}{Z_o} - Z_o C_{se}\right)$$

$$t_{23} = \frac{1}{2Z_e} j \tan\frac{\theta_e}{2} \sqrt{Z_o}\left(A_{se} + 1 - \frac{B_{se}}{Z_o} \right)$$

$$t_{31} = 2t_{13}$$

$$t_{32} = -2t_{23}$$

$$t_{33} = j\omega C_S + \frac{j2\tan\frac{\theta_e}{2}}{Z_e} - \frac{j\tan^2\frac{\theta_e}{2}\sin\theta_e}{Z_e}$$

The ABCD parameters for a single electrode section denoted in the above equations by A_{se}, B_{se}, C_{se} and D_{se} are obtained by cascading the ABCD matrices for the free and metallized sections corresponding to a single electrode as shown in Figure 4.11. From these parameters, the values of θ_e and Z_e are calculated as[139,140]

$$\theta_e = \cos^{-1}(A_{se})$$

$$Z_e = \frac{B_{se}}{j\sin(\theta_e)}$$

Equation 4-13

The main advantage of this method over the conventional transmission matrix approach is that the effect of metallization which creates a mismatch in the acoustic impedance is taken into account. Therefore, the results obtained are expected to be more accurate when compared to the conventional method given in [133].

In the following section, the cascaded matrices for two fingers (a single finger pair) will be derived which will then be generalized to n finger pairs. Figure 4.12 shows the cascade connection of two fingers. Here, the same voltage V is applied to both the fingers and the total current I is computed as the sum of the current in the two fingers I_1 and I_2 ($I = I_1 + I_2$).

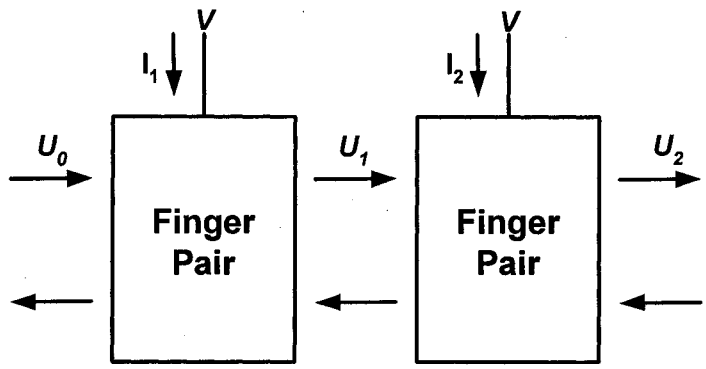

Figure 4.12: Schematic of two fingers in cascade

The three port transmission matrix for each finger pair can be written as follows:

$$\begin{bmatrix} U_o^+ \\ U_o^- \\ I_1 \end{bmatrix} = \begin{bmatrix} t_{11} & t_{12} & t_{13} \\ t_{21} & t_{22} & t_{23} \\ t_{31} & t_{32} & t_{33} \end{bmatrix}_1 \begin{bmatrix} U_1^+ \\ U_1^- \\ V \end{bmatrix} \quad \textbf{Equation 4-14}$$

$$\begin{bmatrix} U_1^+ \\ U_1^- \\ I_2 \end{bmatrix} = \begin{bmatrix} t_{11} & t_{12} & t_{13} \\ t_{21} & t_{22} & t_{23} \\ t_{31} & t_{32} & t_{33} \end{bmatrix}_2 \begin{bmatrix} U_2^+ \\ U_2^- \\ V \end{bmatrix} \quad \textbf{Equation 4-15}$$

Each of the above equations can be split into two equations one for the acoustic port and the other for the electric port. Equation 4-14 can be rewritten as

$$\begin{bmatrix} U_o^+ \\ U_o^- \end{bmatrix} = \begin{bmatrix} t_{11} & t_{12} \\ t_{21} & t_{22} \end{bmatrix}_1 \begin{bmatrix} U_1^+ \\ U_1^- \end{bmatrix} + \begin{bmatrix} t_{13} \\ t_{23} \end{bmatrix}_1 V \quad \textbf{Equation 4-16}$$

$$I_1 = \begin{bmatrix} t_{31} & t_{32} \end{bmatrix}_1 \begin{bmatrix} U_1^+ \\ U_1^- \end{bmatrix} + (t_{33})_1 V \quad \textbf{Equation 4-17}$$

Similarly, Equation 4-15 can be expressed as

$$\begin{bmatrix} U_1^+ \\ U_1^- \end{bmatrix} = \begin{bmatrix} t_{11} & t_{12} \\ t_{21} & t_{22} \end{bmatrix}_2 \begin{bmatrix} U_2^+ \\ U_2^- \end{bmatrix} + \begin{bmatrix} t_{13} \\ t_{23} \end{bmatrix}_2 V \quad \textbf{Equation 4-18}$$

$$I_2 = \begin{bmatrix} t_{31} & t_{32} \end{bmatrix}_2 \begin{bmatrix} U_2^+ \\ U_2^- \end{bmatrix} + (t_{33})_2 V \quad \textbf{Equation 4-19}$$

Combining Equation 4-16 and Equation 4-18 we get,

$$\begin{bmatrix} U_o^+ \\ U_o^- \end{bmatrix} = \begin{bmatrix} t_{11} & t_{12} \\ t_{21} & t_{22} \end{bmatrix}_1 \begin{bmatrix} t_{11} & t_{12} \\ t_{21} & t_{22} \end{bmatrix}_2 \begin{bmatrix} U_2^+ \\ U_2^- \end{bmatrix} + \left(\begin{bmatrix} t_{11} & t_{12} \\ t_{21} & t_{22} \end{bmatrix}_1 \begin{bmatrix} t_{13} \\ t_{23} \end{bmatrix}_2 + \begin{bmatrix} t_{13} \\ t_{23} \end{bmatrix}_1 \right) V \qquad \textbf{Equation 4-20}$$

In a similar manner, Equation 4-17, Equation 4-18, and Equation 4-19 can be combined to give the following expression for the total current I

$$I = \begin{bmatrix} t_{31} & t_{32} \end{bmatrix}_1 \left(\begin{bmatrix} t_{11} & t_{12} \\ t_{21} & t_{22} \end{bmatrix}_2 \begin{bmatrix} U_2^+ \\ U_2^- \end{bmatrix} + \begin{bmatrix} t_{13} \\ t_{23} \end{bmatrix}_2 V \right) + (t_{33})_1 V + \begin{bmatrix} t_{31} & t_{32} \end{bmatrix}_2 \begin{bmatrix} U_2^+ \\ U_2^- \end{bmatrix} + (t_{33})_2 V \qquad \textbf{Equation 4-21}$$

Using Equation 4-20 and Equation 4-21, the cascaded relations for a finger pair can be obtained as

$$T_p = \begin{bmatrix} t_{11} & t_{12} \\ t_{21} & t_{22} \end{bmatrix}_{fp} = \begin{bmatrix} t_{11} & t_{12} \\ t_{21} & t_{22} \end{bmatrix}_1 \begin{bmatrix} t_{11} & t_{12} \\ t_{21} & t_{22} \end{bmatrix}_2 \qquad \textbf{Equation 4-22}$$

$$B_p = \begin{bmatrix} t_{13} \\ t_{23} \end{bmatrix}_{fp} = \begin{bmatrix} t_{11} & t_{12} \\ t_{21} & t_{22} \end{bmatrix}_1 \begin{bmatrix} t_{13} \\ t_{23} \end{bmatrix}_2 + \begin{bmatrix} t_{13} \\ t_{23} \end{bmatrix}_1 \qquad \textbf{Equation 4-23}$$

$$C_p = \begin{bmatrix} t_{31} & t_{32} \end{bmatrix}_{fp} = \begin{bmatrix} t_{31} & t_{32} \end{bmatrix}_1 \begin{bmatrix} t_{11} & t_{12} \\ t_{21} & t_{22} \end{bmatrix}_2 + \begin{bmatrix} t_{31} & t_{32} \end{bmatrix}_2 \qquad \textbf{Equation 4-24}$$

$$t_{33p} = (t_{33})_{fp} = (t_{33})_1 + (t_{33})_2 + \begin{bmatrix} t_{31} & t_{32} \end{bmatrix}_1 \begin{bmatrix} t_{13} \\ t_{23} \end{bmatrix}_2 \qquad \textbf{Equation 4-25}$$

By repeating the above procedure for different values of the number of finger pairs, the author has derived the following generalized equations for N finger pairs.

$$T_N = (T_p)^N \qquad \textbf{Equation 4-26}$$

$$B_N = \sum_{i=1}^{N} T_p^{i-1} B_p \qquad \textbf{Equation 4-27}$$

$$C_N = \sum_{i=0}^{N-1} C_p T_p^i \qquad \textbf{Equation 4-28}$$

$$t_{33N} = N t_{33p} + \sum_{i=1}^{N} (N-i) C_p T_p^{i-1} B_p \qquad \textbf{Equation 4-29}$$

The overall transmission matrix for the IDT can now be expressed as

$$T = \begin{bmatrix} T_N & B_N \\ C_N & t_{33N} \end{bmatrix} \qquad \textbf{Equation 4-30}$$

where the order of the T_N, B_N, C_N matrices are 2 × 2, 2 × 1 and 1 × 2 respectively and therefore T will be a 3 × 3 matrix. In the following paragraphs, the transmission matrix for an open-circuited and short-circuited grating will be discussed. The acoustic wave amplitudes on the left and right hand side of a short circuit SAW grating is shown in Figure 4.13. The short circuited SAW grating has the same transmission matrix as that of the IDT and is given by[139]

$$\begin{bmatrix} U_{i-1}^{+} \\ U_{i-1}^{-} \end{bmatrix} = \begin{bmatrix} t_{11} & t_{12} \\ t_{21} & t_{22} \end{bmatrix} \begin{bmatrix} U_{i}^{+} \\ U_{i}^{-} \end{bmatrix} \qquad \textbf{Equation 4-31}$$

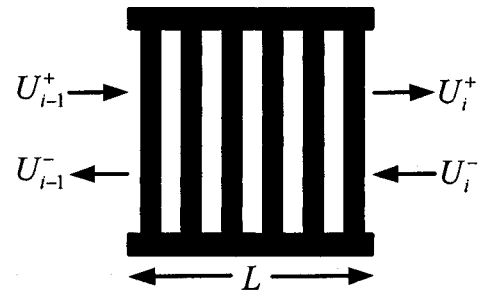

Figure 4.13: Schematic diagram of the short-circuit SAW grating

Figure 4.14 shows the schematic diagram of an open circuited reflector grating. The transmission matrix for an open-circuited SAW grating can be obtained from the 3 × 3 IDT transmission matrix given in Equation 4-10 by setting the current (I) between the bus bars of an IDT to be zero. By substituting this condition in Equation 4-10, the following transmission matrix can be derived for the open circuit SAW grating[139]:

$$\begin{bmatrix} U_{i-1}^{+} \\ U_{i-1}^{-} \end{bmatrix} = \begin{bmatrix} t_{11} - \dfrac{t_{13}t_{31}}{t_{33}} & t_{12} - \dfrac{t_{13}t_{32}}{t_{33}} \\ t_{21} - \dfrac{t_{23}t_{31}}{t_{33}} & t_{22} - \dfrac{t_{23}t_{32}}{t_{33}} \end{bmatrix} \begin{bmatrix} U_{i}^{+} \\ U_{i}^{-} \end{bmatrix} \qquad \textbf{Equation 4-32}$$

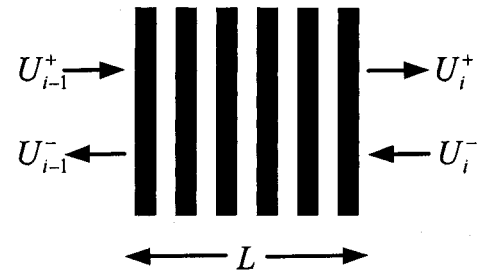

Figure 4.14: Schematic diagram of an open-circuit SAW grating

The acoustic transmission line of length d (see Figure 4.15) is represented by the following transmission line matrix $[D]$[29]

$$[D]=\begin{bmatrix} e^{j\beta d} & 0 \\ 0 & e^{-j\beta d} \end{bmatrix} \qquad \textbf{Equation 4-33}$$

4.3.3.1 Transmission matrix for the SAW delay line

Figure 4.15 shows the schematic of the SAW delay line depicted in terms of the constituent matrices. The acoustic wave amplitudes at the left side of the input transducer can be written as

$$[U_o]=[M][U_3]+\begin{bmatrix} t_{13} \\ t_{23} \end{bmatrix}_1 V_{in}+[K]V_{out} \qquad \textbf{Equation 4-34}$$

where $[M]=[t_1][D_2][t_3]$ and subscripts 1, 2 and 3 refer to the input IDT, delay path and output IDT respectively, $[t]=\begin{bmatrix} t_{11} & t_{12} \\ t_{21} & t_{22} \end{bmatrix}$ and the matrix $[D]$ is defined as in Equation 4-33. The matrix $[K]=[t_1][D_2]\begin{bmatrix} t_{13} \\ t_{23} \end{bmatrix}_3$. The currents in the input and output transducers can be written as

$$I_{in}=[P][U_3]+[L]V_{out}+(t_{33})_1 V_{in} \qquad \textbf{Equation 4-35}$$

$$I_{out}=[t_{31} \quad t_{32}]_3[U_3]+(t_{33})_3 V_{out} \qquad \textbf{Equation 4-36}$$

where $[P]=[t_{31} \quad t_{32}]_1[D_2][T_3]$ and $[L]=[t_{31} \quad t_{32}]_1[D_2]\begin{bmatrix} t_{13} \\ t_{23} \end{bmatrix}_3$. Since no acoustic power is

incident on the two acoustic ports, $U_0^+ = 0$ and $U_3^- = 0$.

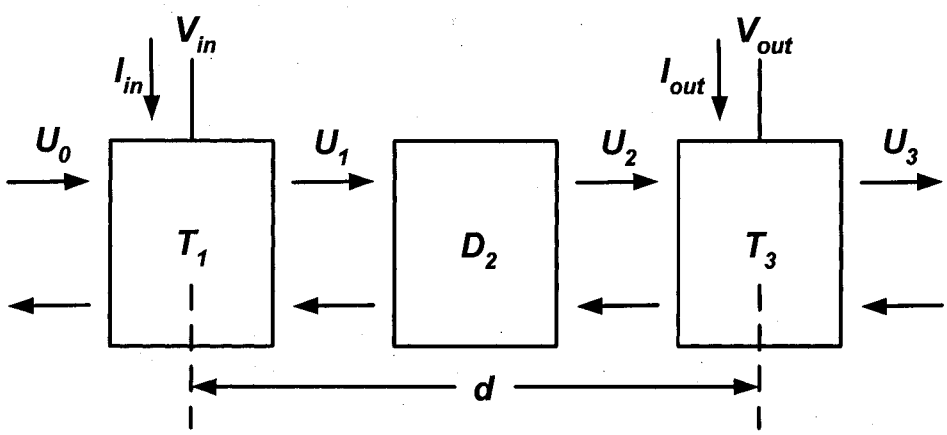

Figure 4.15: SAW delay line matrix building blocks

Using the above equations, the expressions for admittance or Y-parameters were first obtained and were used to determine the scattering or s-parameters. The Y-parameters for a two-port network are defined as:

$$\begin{bmatrix} I_{in} \\ I_{out} \end{bmatrix} = \begin{bmatrix} Y_{11} & Y_{12} \\ Y_{21} & Y_{22} \end{bmatrix} \begin{bmatrix} V_{in} \\ V_{out} \end{bmatrix} \qquad \textbf{Equation 4-37}$$

The Y-parameters for the SAW delay line were then determined as illustrated below:

$$Y_{11} = \frac{I_{in}}{V_{in}} \Big|_{V_{out}=0} \qquad \textbf{Equation 4-38}$$

Substituting V_{out}=0 in Equation 4-34, we get

$$\begin{bmatrix} 0 \\ U_0^- \end{bmatrix} = [M] \begin{bmatrix} U_3^+ \\ 0 \end{bmatrix} + \begin{bmatrix} t_{13} \\ t_{23} \end{bmatrix}_1 V_{in} \qquad \textbf{Equation 4-39}$$

from which we obtain $U_3^+ = -\frac{t_{131}}{M_{11}} V_{in}$.

Substituting V_{out}=0 in Equation 4-35, we get

$$I_{in} = [P] \begin{bmatrix} U_3^+ \\ 0 \end{bmatrix} + (t_{33})_1 V_{in} \qquad \textbf{Equation 4-40}$$

Substituting the expression for U_3^+ in Equation 4-40, we obtain

$$I_{in} = \frac{-P_{11}t_{131}}{M_{11}} V_{in} + t_{331} V_{in} \qquad \textbf{Equation 4-41}$$

Combining Equation 4-38 and Equation 4-41, we get

$$Y_{11} = \frac{-P_{11}t_{131}}{M_{11}} + t_{331} \qquad \textbf{Equation 4-42}$$

Using similar procedure, the other Y parameters were obtained by substituting boundary conditions in Equation 4-34, Equation 4-35 and Equation 4-36. The expressions for the other Y-parameters were derived as:

$$Y_{21} = \frac{I_{out}}{V_{in}}|_{V_{out}=0} = \frac{-t_{313}t_{131}}{M_{11}} \qquad \textbf{Equation 4-43}$$

$$Y_{12} = \frac{I_{in}}{V_{out}}|_{V_{in}=0} = \frac{-P_{11}K_{11}}{M_{11}} + L_{11} \qquad \textbf{Equation 4-44}$$

$$Y_{22} = \frac{I_{out}}{V_{out}}|_{V_{in}=0} = \frac{-t_{313}K_{11}}{M_{11}} + t_{333} \qquad \textbf{Equation 4-45}$$

Knowing the expressions for the Y-parameters, the expressions for the S-parameters can be easily obtained. The MATLAB™ code used to simulate the frequency response of the delay line is given in Appendix B.

4.3.3.2 Transmission matrix for the SAW two-port resonator

Figure 4.16 shows the schematic of the SAW two-port resonator depicted in terms of the constituent matrices. The acoustic wave amplitudes at the left side of the grating can be written as

$$[U_o] = [M][U_3] + [N]V_{in} + [K]V_{out} \qquad \textbf{Equation 4-46}$$

where $[M] = [G_1][D_2][t_3][D_4][t_5][D_6][G_7]$, $[N] = [G_1][D_2]\begin{bmatrix} t_{13} \\ t_{23} \end{bmatrix}_3$, $[K] = [G_1][D_2][t_3][D_4]\begin{bmatrix} t_{13} \\ t_{23} \end{bmatrix}_5$.

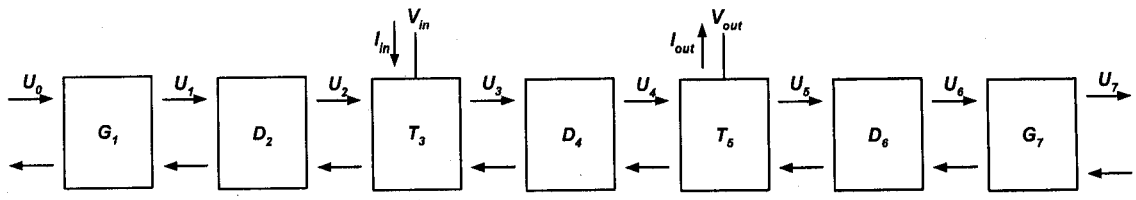

Figure 4.16: SAW two-port resonator matrix building blocks

The currents in the input and output transducers can be written as

$$I_{in} = [P][U_7] + [L]V_{out} + (t_{33})_3 V_{in} \quad \textbf{Equation 4-47}$$

$$I_{out} = [t_{31} \quad t_{32}]_5 [D_6][G_7][U_7] + (t_{33})_5 V_{out} \quad \textbf{Equation 4-48}$$

where $[P] = [t_{31} \quad t_{32}]_3 [D_4][T_5][D_6][G_7]$ and $[L] = [t_{31} \quad t_{32}]_3 [D_4] \begin{bmatrix} t_{13} \\ t_{23} \end{bmatrix}_5$. Since no acoustic power is incident on the two acoustic ports, $U_0^+ = 0$ and $U_7^- = 0$. Substituting V_{out}=0 in Equation 4-46, we get

$$\begin{bmatrix} 0 \\ U_0^- \end{bmatrix} = [M] \begin{bmatrix} U_7^+ \\ 0 \end{bmatrix} + [N]V_{in} \quad \textbf{Equation 4-49}$$

where $[N] = [G_1][D_2] \begin{bmatrix} t_{13} \\ t_{23} \end{bmatrix}_3$ and therefore $U_7^+ = -\frac{N_{11}}{M_{11}} V_{in}$.

Substituting V_{out}=0 in Equation 4-47, we get

$$I_{in} = [P] \begin{bmatrix} U_7^+ \\ 0 \end{bmatrix} + (t_{33})_3 V_{in} \quad \textbf{Equation 4-50}$$

Substituting the expression for U_7^+ in Equation 4-50, we obtain

$$I_{in} = \frac{-P_{11}N_{11}}{M_{11}} V_{in} + t_{333} V_{in} \quad \textbf{Equation 4-51}$$

Therefore, we get

$$Y_{11} = \frac{-P_{11}N_{11}}{M_{11}} + t_{333} \quad \textbf{Equation 4-52}$$

Using similar procedure, the other Y parameters were obtained by substituting boundary conditions in Equation 4-46, Equation 4-47 and Equation 4-48. The expressions for the other Y-parameters were derived as:

$$Y_{21} = \frac{I_{out}}{V_{in}}|_{V_{out}=0} = [t_{31} \quad t_{32}]_5 [D_6][G_7]\begin{bmatrix} -N_{11} \\ \overline{M_{11}} \\ 0 \end{bmatrix} \qquad \textbf{Equation 4-53}$$

$$Y_{12} = \frac{I_{in}}{V_{out}}|_{V_{in}=0} = \frac{-P_{11}K_{11}}{M_{11}} + L_{11} \qquad \textbf{Equation 4-54}$$

$$Y_{22} = \frac{I_{out}}{V_{out}}|_{V_{in}=0} = [t_{31} \quad t_{32}]_5 [D_6][G_7]\begin{bmatrix} -K_{11} \\ \overline{M_{11}} \\ 0 \end{bmatrix} + t_{335} \qquad \textbf{Equation 4-55}$$

Knowing the expressions for the Y-parameters, the expressions for the S-parameters can be easily obtained.

4.3.3.3 Transmission matrix for the SAW one-port resonator

Figure 4.17 shows the SAW one-port resonator represented in terms of the individual element matrices. However, since there is only one-port in this case, only Y_{11} needs to be derived.

The acoustic wave amplitudes at the left side of the grating can be written as

$$[U_o] = [M][U_5] + [N]V_{in} \qquad \textbf{Equation 4-56}$$

where $[M] = [G_1][D_2][t_3][D_4][G_5], [N] = [G_1][D_2]\begin{bmatrix} t_{13} \\ t_{23} \end{bmatrix}_3$.

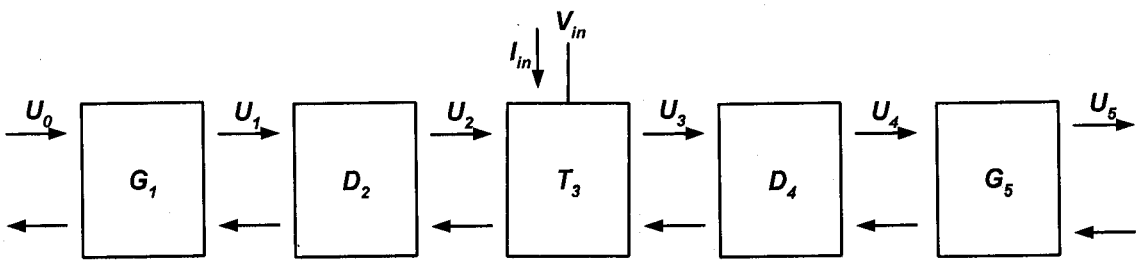

Figure 4.17: SAW one-port resonator matrix building blocks

The current in the transducer can be written as

$$I_{in} = [P][U_5] + (t_{33})_3 V_{in} \qquad \textbf{Equation 4-57}$$

where $[P] = [t_{31} \quad t_{32}]_3 [D_4][G_5]$. Since no acoustic power is incident on the two acoustic ports, $U_0^+ = 0$ and $U_5^- = 0$. From Equation 4-56, we get

$$\begin{bmatrix} 0 \\ U_0^- \end{bmatrix} = [M]\begin{bmatrix} U_5^+ \\ 0 \end{bmatrix} + [N]V_{in} \qquad \textbf{Equation 4-58}$$

and therefore $U_5^+ = -\frac{N_{11}}{M_{11}}V_{in}$. Substituting the expression for U_5^+ in Equation 4-58, we obtain

$$I_{in} = \frac{-P_{11}N_{11}}{M_{11}}V_{in} + t_{333}V_{in} \qquad \textbf{Equation 4-59}$$

Therefore, we get

$$Y_{11} = \frac{-P_{11}N_{11}}{M_{11}} + t_{333} \qquad \textbf{Equation 4-60}$$

In the next section, results of SAW device simulations using the transmission matrix approach will be presented.

4.3.4 MATLAB™ simulation results

Different SAW device designs were simulated using the transmission matrix approach in MATLAB™. Figure 4.18 shows the magnitude and phase of S_{21} of a SAW delay line with the following specifications: number of fingers pairs are 50 and 15 for the input and output IDTs respectively, acoustic aperture $80\lambda_o$ and separation between IDTs=$100\lambda_o$. The substrate used was YZ-$LiNbO_3$ with the following specifications: Electromechanical coupling coefficient (K^2)=0.045, capacitance/finger pair/unit length (C_o)=4.6 pF/cm and free surface wave velocity (V_s)=3488 m/s. The ripples in the frequency response can be attributed to the reflection between fingers and also impedance mismatch with the 50Ω source and load impedance used in the simulations[141]. In addition, triple transit interference and electromagnetic interference (EMI) causes additional ripples in the passband[133]. Also, the increased sidelobe levels are due to the fact that neither of the transducers were apodized to provide better sidelobe suppression. The bandwidth (BW) between the first nulls on either side of the center frequency depends on the number of finger pairs in the IDT and is given by[29]

$$BW = \frac{2}{N_p} f_o \qquad \textbf{Equation 4-61}$$

where N_p is the number of finger pairs in the IDT and f_o is the center frequency of the IDT. Therefore, as the number of finger pairs decreases the bandwidth increases.

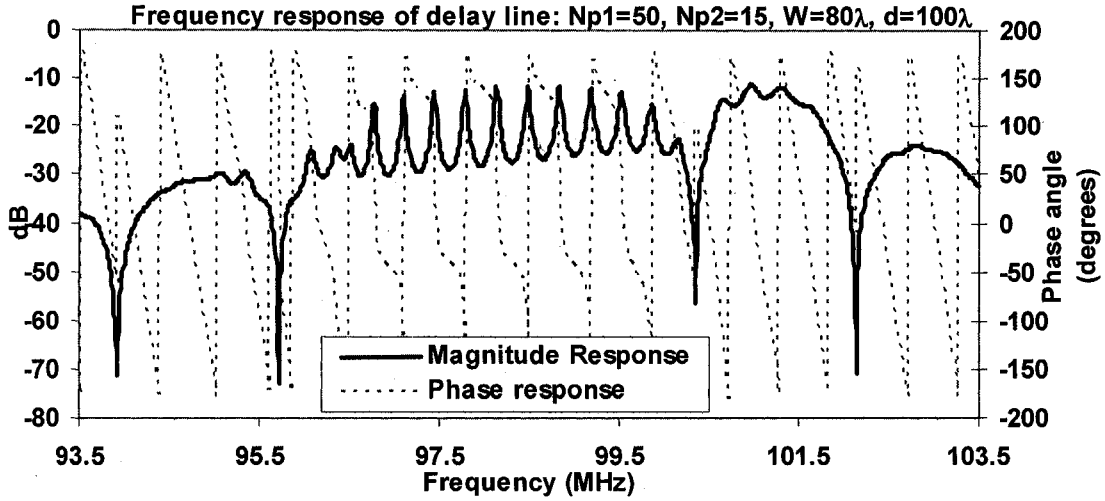

Figure 4.18: Frequency response of delay line with Np1=50, Np2=15, W=80λo, IDT separation=100λo

Figure 4.19 shows a comparison of the frequency response of 2 different delay line designs where all the design parameters are the same except for the number of finger pairs in the input IDT. The solid curve shows the response for N_p=50 and the dotted curve shows the response for N_p=40. It can be seen that fewer number of finger pairs in either of the IDTs gives rise to a wideband response. For an IDT with N_p=50 and N_p=40, Equation 4-61 gives *BW* of 4 MHz and 5 MHz. The same can also be verified from Figure 4.19 where the *BW* for the two different designs are shown for the frequency response curves that was simulated using MATLAB™. From the simulated responses in Figure 4.19, it was observed that the bandwidth between the first nulls were close to 4.6 MHz and 5.4 MHz for N_p=50 and N_p=40 respectively. Thus, the simulated results were in good agreement with theoretical predictions.

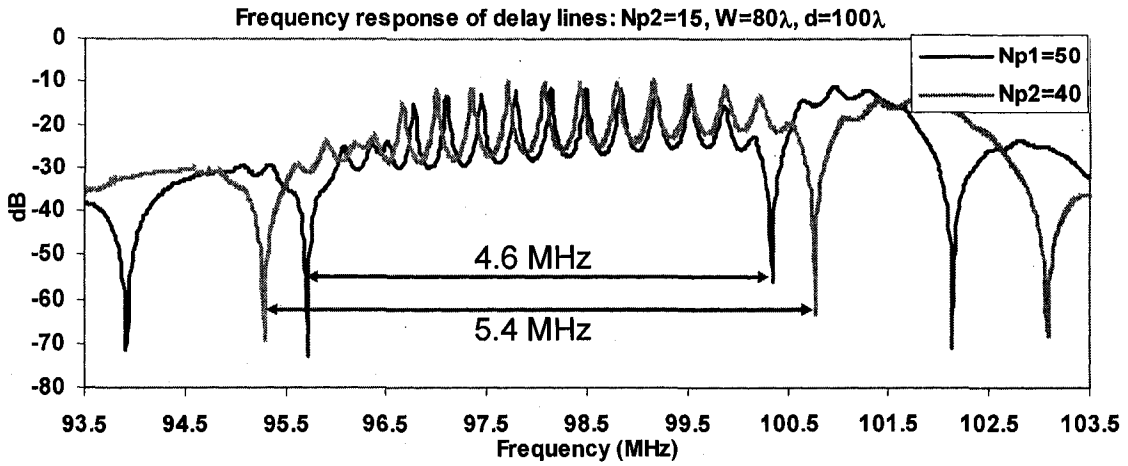

Figure 4.19: Comparison of frequency response of delay line with different finger pairs in the input IDT

4.3.5 PSpice™ simulation using the 3-port equivalent circuit model

Simulation of SAW devices was done in Orcad Capture CIS™ using the Mason's equivalent circuit for IDTs and reflectors and the transmission line representation for the delay path[142]. For the IDTs, the mason's equivalent circuit for a single finger was used which included the effects of impedance mismatch between the metallized and free regions. Figure 4.20 shows the Mason's equivalent circuit for a single finger[143]. This circuit was then cascaded depending upon the device design to obtain the overall equivalent circuit for the IDT. The transit angles for the metallized and free sections of the substrate are given by ψ_n and ϕ_n respectively where

$$\psi_n = \frac{\pi\omega}{2\omega_m}$$

$$\phi_n = \frac{\pi\omega}{2\omega_o}$$

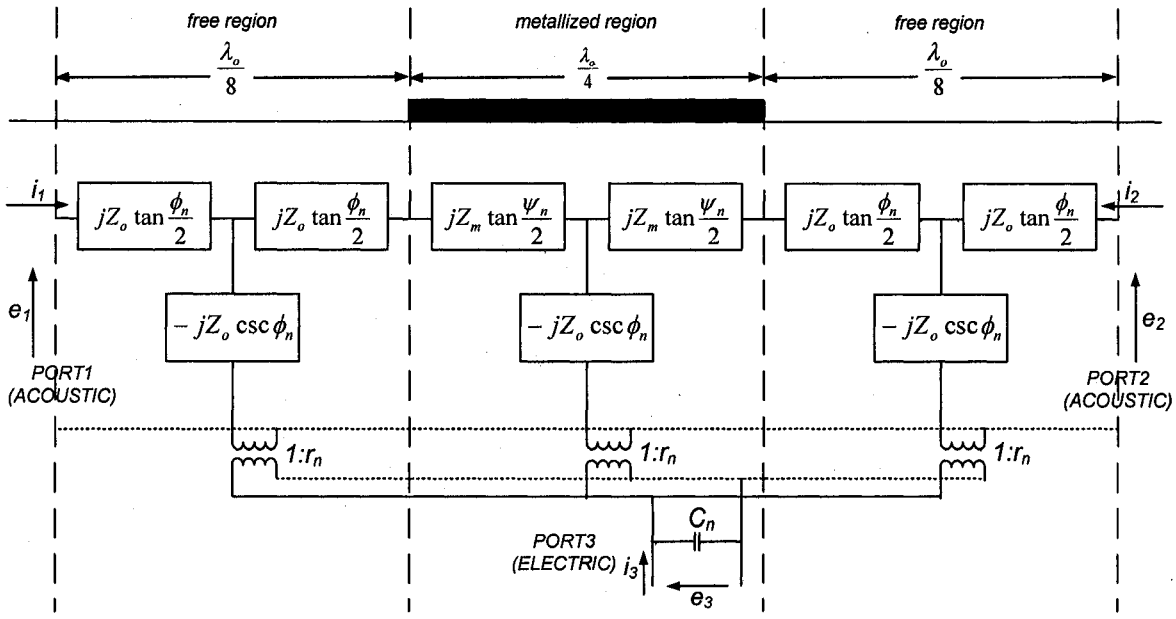

Figure 4.20: Mason's equivalent circuit for a single finger in the IDT

The electroacoustic coupling is represented by the transformer whose turns ratio is given by[143]

$$r_n = (-1)^n \sqrt{2 f_n C_n k^2 Z_o}\left[\frac{K(2^{-1/2})}{K(q_n)}\right]$$

where f_n is the center frequency of the IDT, k^2 is the electromechanical coupling coefficient of the substrate, Z_o is the substrate mechanical impedance, K is the Jacobian complete elliptic integral of the first kind, C_n and q_n are given by the following relations:

$$C_n = \frac{w_n \sqrt{\varepsilon_{11}\varepsilon_{33}}}{2}\frac{K(q_n)}{K(q_n')}$$

$$q_n = \sin\left(\frac{\pi}{4}\right)$$

$$q_n' = \sqrt{1-q_n^2}$$

where w_n is the acoustic aperture of the specific section of the IDT, ε_{11} and ε_{33} are the dielectric tensor components of the substrate. The impedance of the free and metallized

sections are given by

$$Z_o = \frac{1}{f_o C_s K^2}$$

$$Z_m = \frac{1}{f_m C_s K^2}$$

where f_m is given by the following relation[133]

$$f_m = \frac{v_m}{\lambda_o} = \frac{1}{\left(\frac{2}{f_a} - \frac{1}{f_o}\right)}$$

where C_s is the capacitance of one periodic section of the IDT, v_m is the velocity of the acoustic wave in the metallized section, f_o is the center frequency of the IDT and f_a is the average shifted center frequency in the IDT.

The tan and cosec elements shown in the Mason's equivalent circuit of Figure 4.20 were implemented using inductors and capacitors as shown in Figure 4.21. Also, shown is a functional description of these elements. From the graphs, the poles and zeros and the value of the impedance at one other frequency are determined and the value for each inductor-capacitor pair is then calculated using the Foster's method[144]. For the cosec circuit, the functional description is realized as a combination of two tan networks as shown by the dashed and dotted curves in Figure 4.21[142]. The values of the tan and cosec elements for the free and metallized region are shown below for a delay line with the following parameters: wavelength λ_o=34.88 μm, acoustic aperture W=80λ_o. The steps used to calculate these values are further detailed in Appendix C.

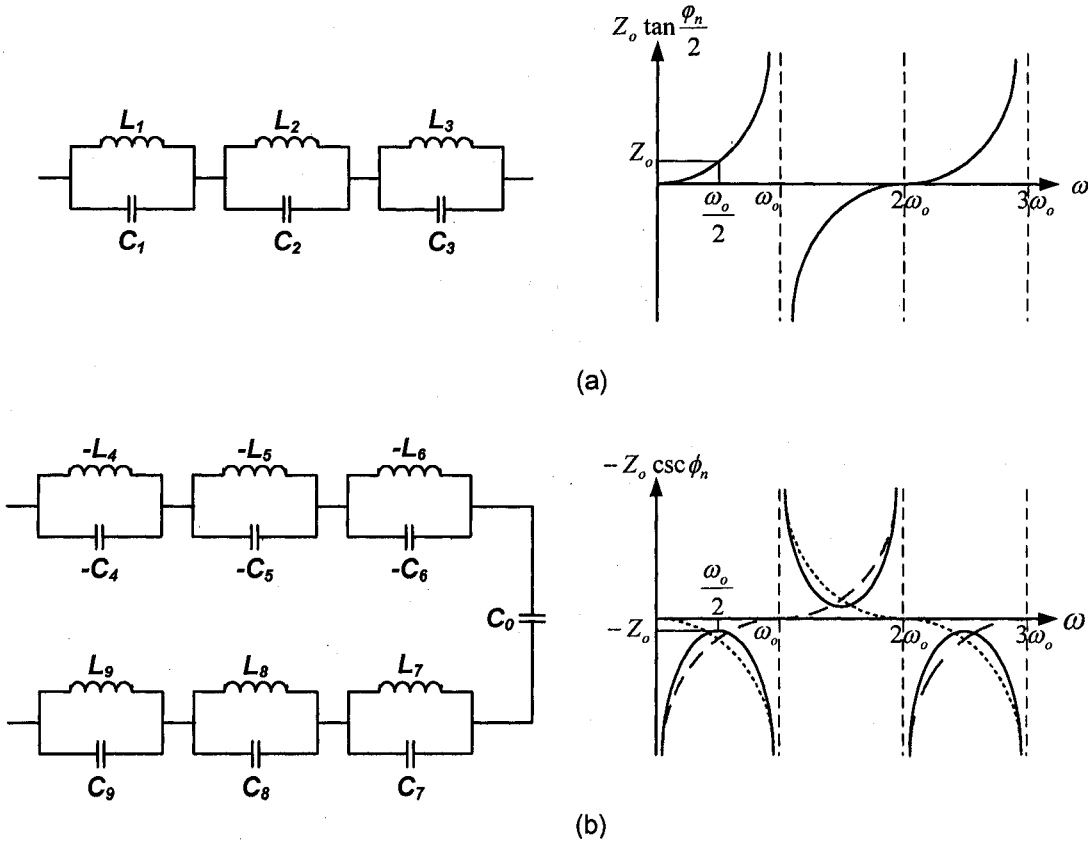

Figure 4.21: Equivalent L-C networks that represent the (a) tan and (b) cosec elements of the Mason's circuit

The delay path between the IDTs was then modeled using a lossless transmission line using the impedance Zo=1 and delay time T=1 μs. The delay time was chosen to be the propagation time of the SAW between the input and output IDTs which are separated by $100\lambda_0$. This assumption is valid since the SAW propagation loss on YZ-$LiNbO_3$ is negligible. Once the values for the circuit elements were determined, a PSpice™ library was created using the PSpice Model Editor™. Orcad Capture CIS was then used to create the schematic and perform the simulation.

4.3.6 PSpice™ simulation results

The schematic for the SAW delay is shown in Figure 4.22. It consists of three main elements: input IDT, output IDT and the delay line separating them. A steady state analysis was then performed on the schematic over a frequency span of 10 MHz around

the 100 MHz center frequency of the SAW delay line. The design specifications that were used for the delay line are as follows: Np1=50, Np2=15, W=80λ_o, λ_o=34.88 μm, IDT separation=100λ_o. The results of the steady state analysis are shown in Figure 4.23. It can be seen that the center frequency is shifted from 100 MHz to 98 MHz due to the effect of metallization. Also, there are periodic ripples in the passband due to the second order effects like triple transit interference, mass loading etc. Figure 4.24 is a comparison of the frequency responses of two delay lines with slightly different number of fingers in their input IDT. It can be seen that the bandwidth between the first nulls on either side of the center frequency decreases as the number of finger pairs is increased from 40 to 50 as discussed in Section 4.3.4.

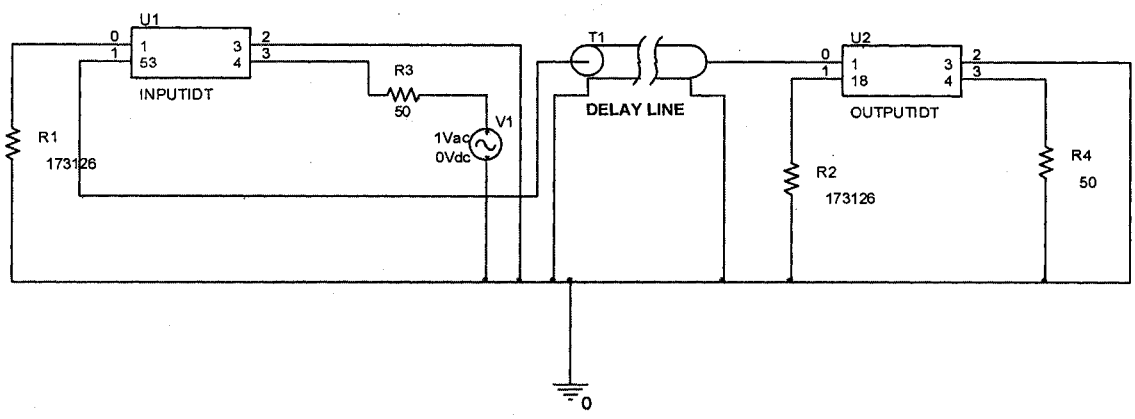

Figure 4.22: SAW delay line model created in Orcad Capture CIS™

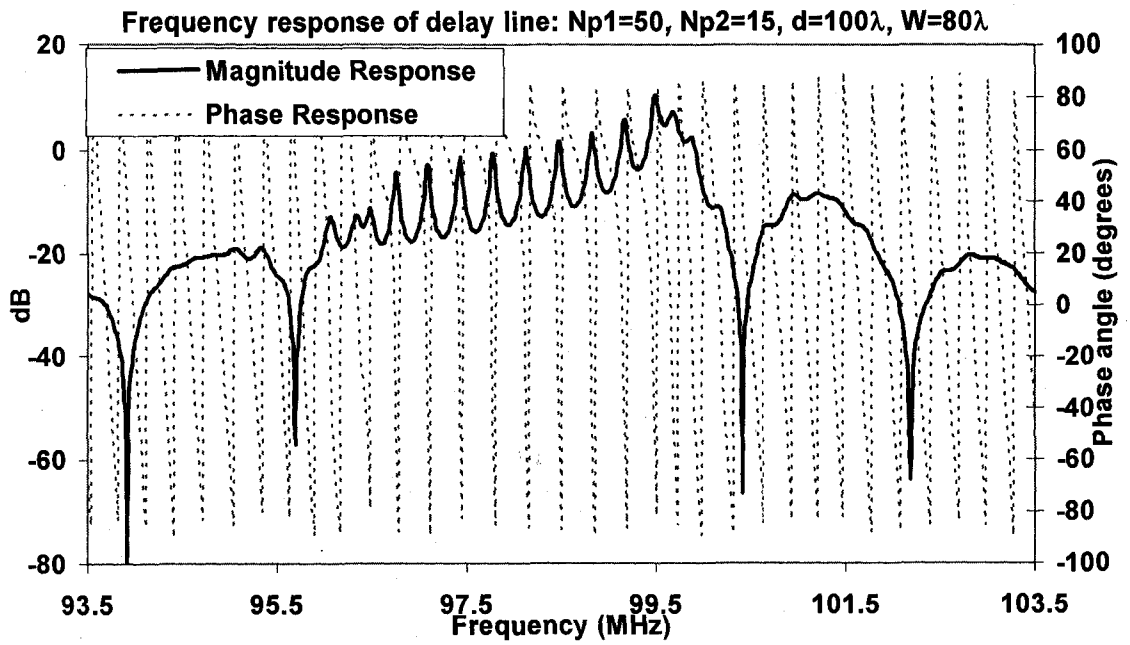

Figure 4.23: Frequency response of the delay line simulated in OrCAD Capture CIS™

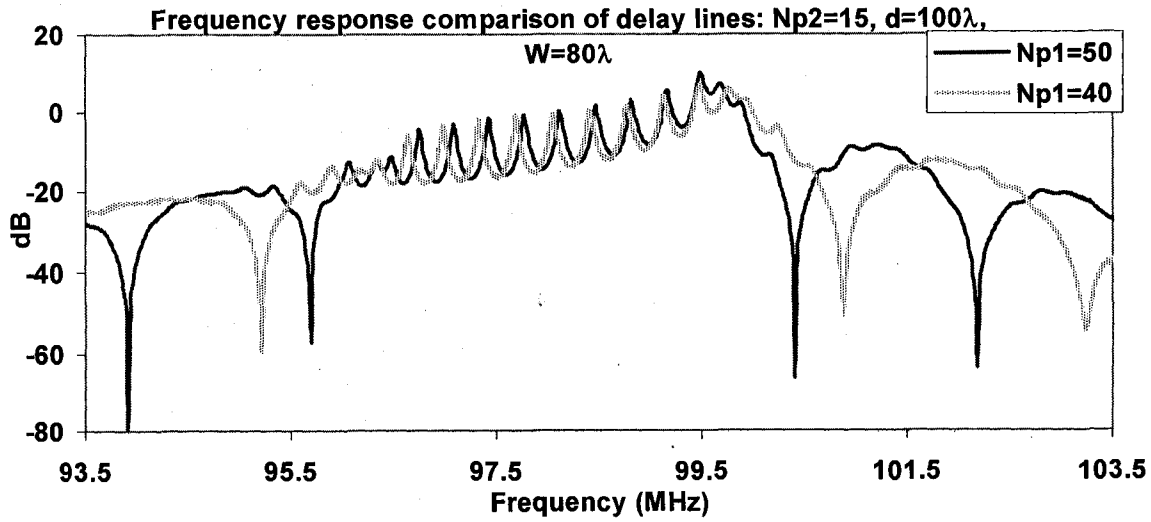

Figure 4.24: Comparison of frequency response of delay lines with different number of fingers in the input IDT

4.4 Summary

This Chapter describes the design of SAW devices and gives a detailed account of the modeling and simulation of SAW devices using three different tools namely CoventorWare™, MATLAB™ and Orcad Capture CIS™. In addition, the simulation results obtained using each of the above tools were presented. In both MATLAB™ and Orcad PSpice™, the effect of finger reflections on the frequency response was taken into account in the simulations. The locations of the nulls, the insertion loss and the magnitude of the ripples were successfully simulated in MATLAB™ and Orcad PSpice™. In CoventorWare™, a complete 3-dimensional view of the wave propagation on the structure can be obtained and it allows the user to probe every single node in the structure to obtain displacement and potential values.

When it comes to modeling, the transmission matrix approach in MATLAB™ requires an in depth understanding of the device physics as well as the mathematics involved. It also requires derivation of the frequency response of the devices using matrix manipulation. Modeling in Orcad PSpice™ is relatively simpler once the values of the tan and cosec elements for each finger are determined. CoventorWare™ modeling is the easiest since only the design parameters have to be known in order to be able to get the 3-dimensional model. However, it requires careful rotation of the model to obtain the required orientation and also optimization of the mesh element sizes in order to be able to compare with the measured responses. In addition, it requires a faster processor and a large memory for the successful completion of the simulations. In terms of computational time, MATLAB™ was observed to be fastest and only takes a few minutes when compared to a few hours for both Orcad PSpice™ and CoventorWare™. Careful consideration of these factors will be helpful in choosing the appropriate method to be used for simulations. The next chapter discusses the fabrication and characterization of SAW devices. It also presents a comparison between simulated and measured SAW device responses.

CHAPTER V

SAW DEVICE FABRICATION AND CHARACTERIZATION

5.1 Introduction

SAW delay lines and two port resonators with a center frequency of 100 MHz were fabricated on a single wafer with the devices having slightly different design parameters. The fabrication was done at the University of Michigan's Micro/Nano fabrication facility in Ann Arbor. This chapter describes in detail the fabrication and characterization process of SAW devices. The measurement results for these fabricated devices are also presented and compared with simulated results for a few devices.

5.2 Mask layout

The mask layout was designed using the layout editor available as part of the CW software. Figure 5.1 is the layout of a single SAW delay line device showing input and output IDTs and the contact pads. Figure 5.2 shows the mask layout for the entire wafer. The L-shaped markers at the four corners of each device were used for alignment purposes during wafer dicing. The mask had six different delay line designs and a two-port resonator design as shown in Table 5.1 and Table 5.2 respectively. All the devices were designed with a center frequency of 100 MHz and were fabricated on Y-cut $LiNbO_3$ wafer.

Table 5.1: Design parameters for fabricated SAW delay lines

Design No	Type of IDT	Np1	Np2	W	IDT separation
1	single finger	50	15	80λ	100λ
2	single finger	50	15	80λ	70λ
3	single finger	40	15	80λ	100λ
4	single finger	50	15	60λ	100λ
5	single finger	50	10	80λ	100λ
6	split finger	50	15	80λ	70λ

Table 5.2: Design parameters for fabricated SAW two-port resonators

Design No	Type of grating	Np1	Np2	Nr	IDT-Grating distance	IDT-IDT distance	W
1	open	9.5	9.5	500	3.635λ	10λ	80λ
2	short	9.5	9.5	500	3.635λ	10λ	80λ

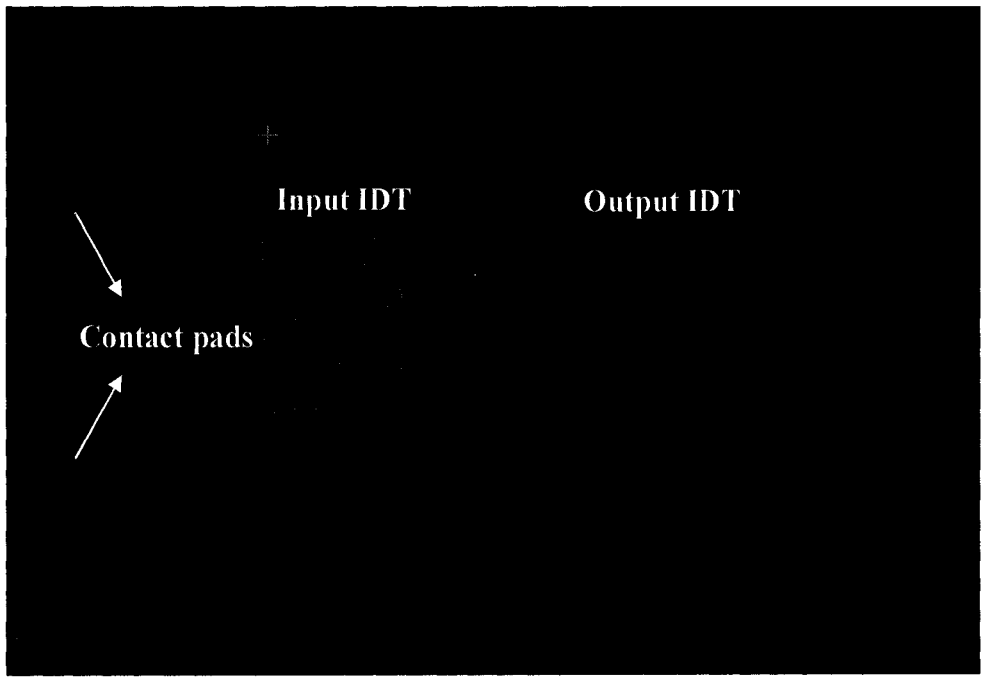

Figure 5.1: Mask layout for a single SAW device with alignment markers

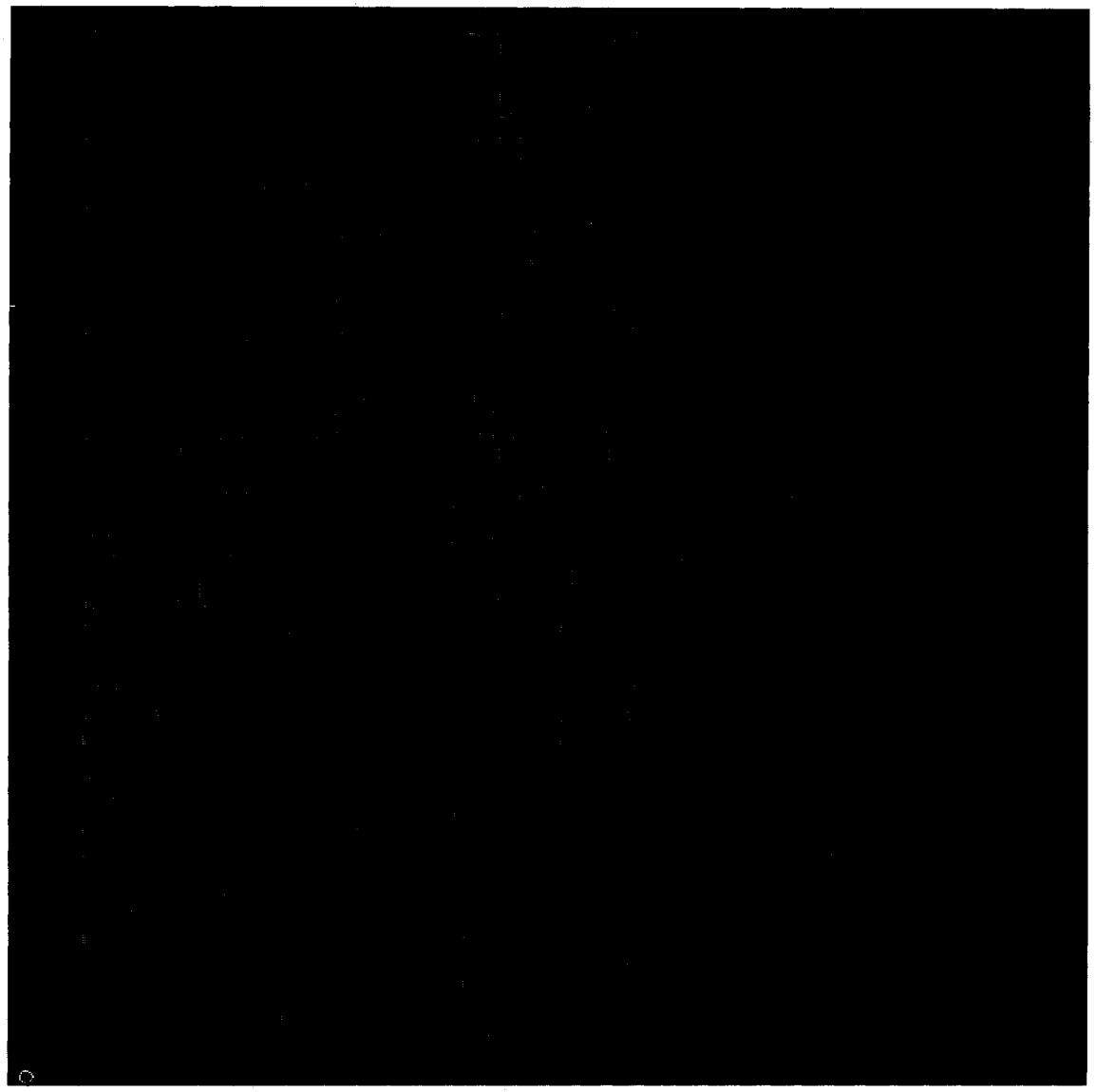

Figure 5.2: Mask layout for the entire Y-cut $LiNbO_3$ wafer

While designing the mask for the devices, careful attention was paid to ensure that the SAW propagation axis was along the z-direction. Figure 5.3 shows the alignment of the devices with respect to the major flat. As can be seen from the figure, the propagation direction of the SAW is parallel to the +Z axis. Following the mask design, the devices were fabricated at the University of Michigan's Micro/Nano fabrication facility in Ann Arbor, Michigan. The fabrication sequence is discussed briefly in the following section.

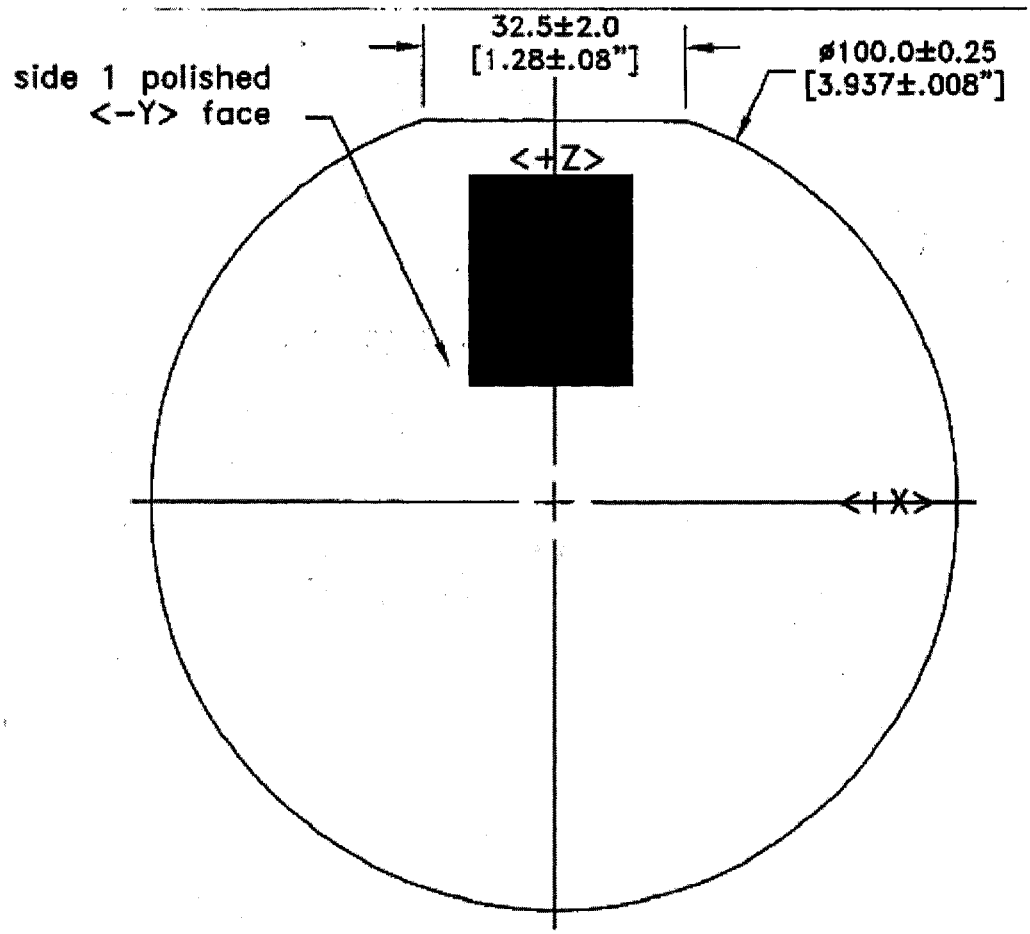

Figure 5.3: Alignment of SAW devices on the Y-cut $LiNbO_3$ wafer

5.3 Fabrication sequence for SAW devices

The fabrication sequence for SAW devices involved seven steps explained here. In the following figures, the fabrication key given below is used.

Fabrication key



Substrate Aluminum Photoresist

The first step of fabrication starts with the cleaning of the substrate by immersing it in a solution of soapy water with a pH between 7.0 and 8.5 or low concentration ammonia in

water, followed by hand-wiping in a mixture of four parts alcohol and one part acetone. The hand wiping is in a continuous motion from one edge to the other to avoid leading- or trailing edge stains. Throughout the cleaning process, it is critical to avoid letting the wafer dry during intermediary steps or prior to the final drying step. Premature drying can leave stains or residue from the baths or cleaning solutions that can be difficult to remove. In step 2, the photoresist was spun on the front side of the wafer (see Figure 5.4). In step 3, photoresist was exposed to UV light using the mask and developed as shown in Figure 5.5. Subsequently, a 200nm thick Aluminum layer was deposited (see Figure 5.6). In step 5, the exposed Aluminum was removed using lift-off as seen in Figure 5.7. Step 6 involved stripping of the photoresist to produce the final device (see Figure 5.8). As a final step, the wafer was diced using blue tape on one side to produce individual devices.

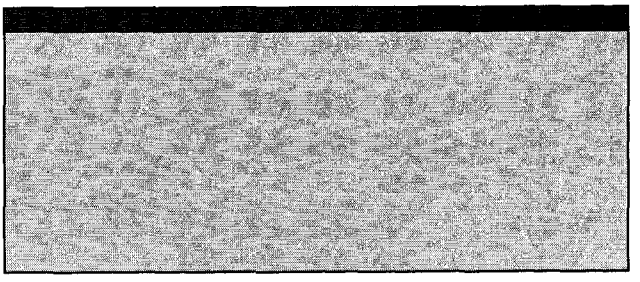

Figure 5.4: Substrate with photoresist (Step 2)

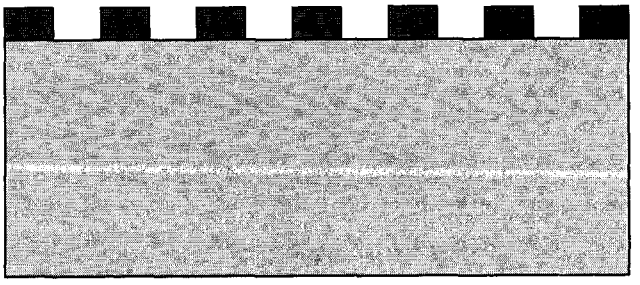

Figure 5.5: Photoresist after exposure to UV light (Step 3)

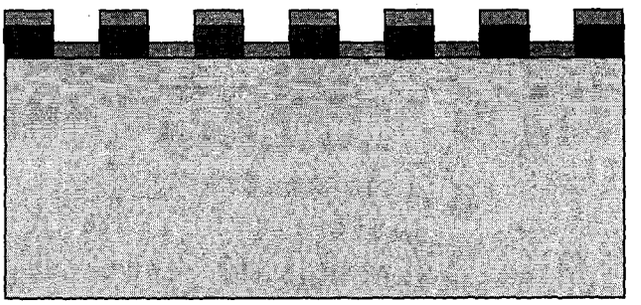

Figure 5.6: Substrate with developed photoresist and deposited aluminum (Step 4)

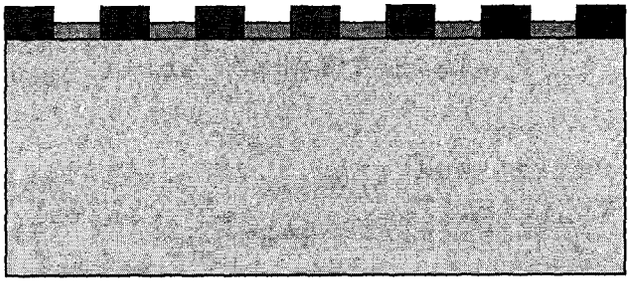

Figure 5.7: Structure after aluminum lift-off (Step 5)

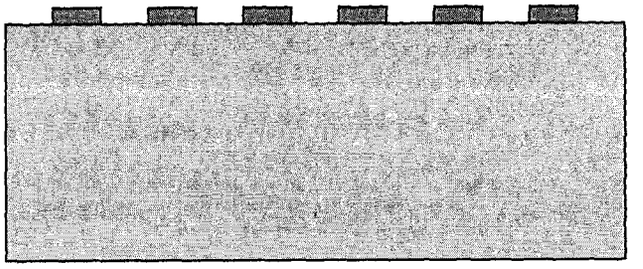

Figure 5.8: Final device after stripping photoresist (Step 6)

5.4 SAW sensor characterization

Figure 5.9 (a) shows a photograph of the fabricated SAW devices after dicing. These devices were then loaded onto a copper board which was mounted with SMA connectors (see Figure 5.9 (b)) and the frequency response of these devices were measured using Agilent 4396B Spectrum/Network/Impedance Analyzer.

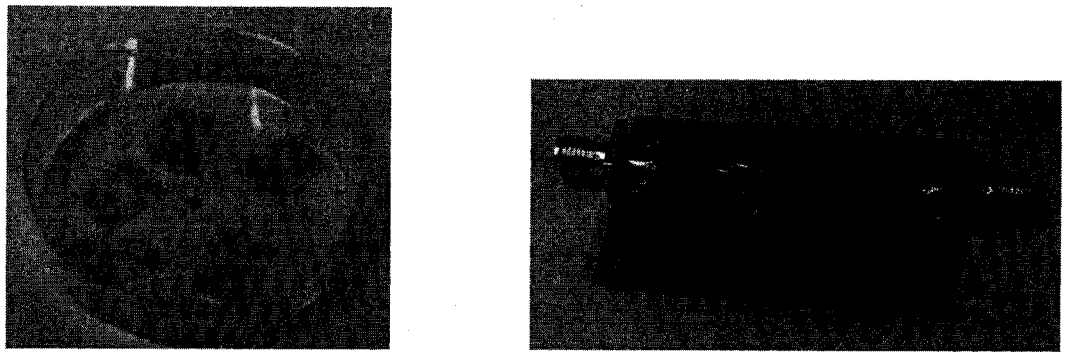

(a) (b)

Figure 5.9: SAW devices (a) after dicing (b) loaded onto Cu board with SMA connectors

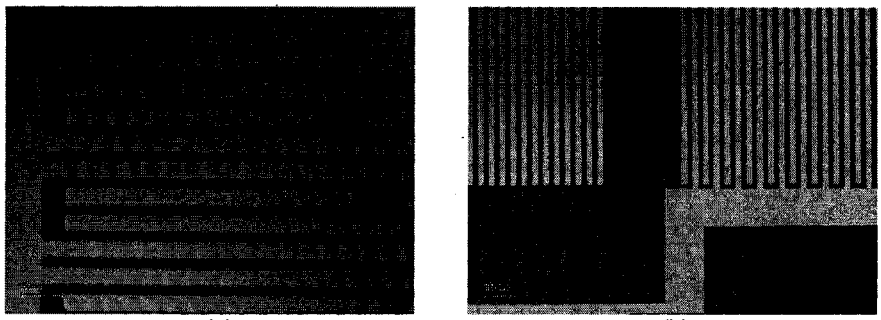

(a) (b)

Figure 5.10: Optical microscope images (a) split finger IDT of a delay line (b) two-port resonator

Figure 5.10 shows optical microscope images of the fabricated SAW devices. Figure 5.10(a) shows the split finger IDT configuration of delay line design 6 and Figure 5.10(b) shows a portion of the IDT and grating of a SAW two-port resonator. Figure 5.11 shows the frequency response of the delay line with the following design specifications: number of fingers pairs are 50 and 15 for the input and output IDTs respectively, acoustic aperture $80\lambda_o$ and separation between IDTs=$100\lambda_o$. The bandwidth between the first nulls on either side of the center frequency is dominated in this design by the input IDT since the output IDT is relatively wideband due to the fewer number of finger pairs. In Section 4.3.4, the null to null bandwidth of the above designed was

calculated to be 4 MHz. From Figure 5.11, it can be seen that the bandwidth between the first nulls is ~4 MHz. The presence of ripples in the passband can be attributed to the various second order effects as explained earlier in chapter 4, electrical/mechanical loading effect of the metallization, electromagnetic and triple transit interference and impedance mismatch with the source and the load to name a few. Figure 5.12 shows the measured frequency response of identical SAW delay lines with different number of finger pairs in the input IDT. As can be seen from the figure the null to null bandwidth of the delay lines with Np1=50 and Np1=40 are close to 4 MHz and 5 MHz respectively and these values closely match the theoretical values predicted in Section 4.3.4.

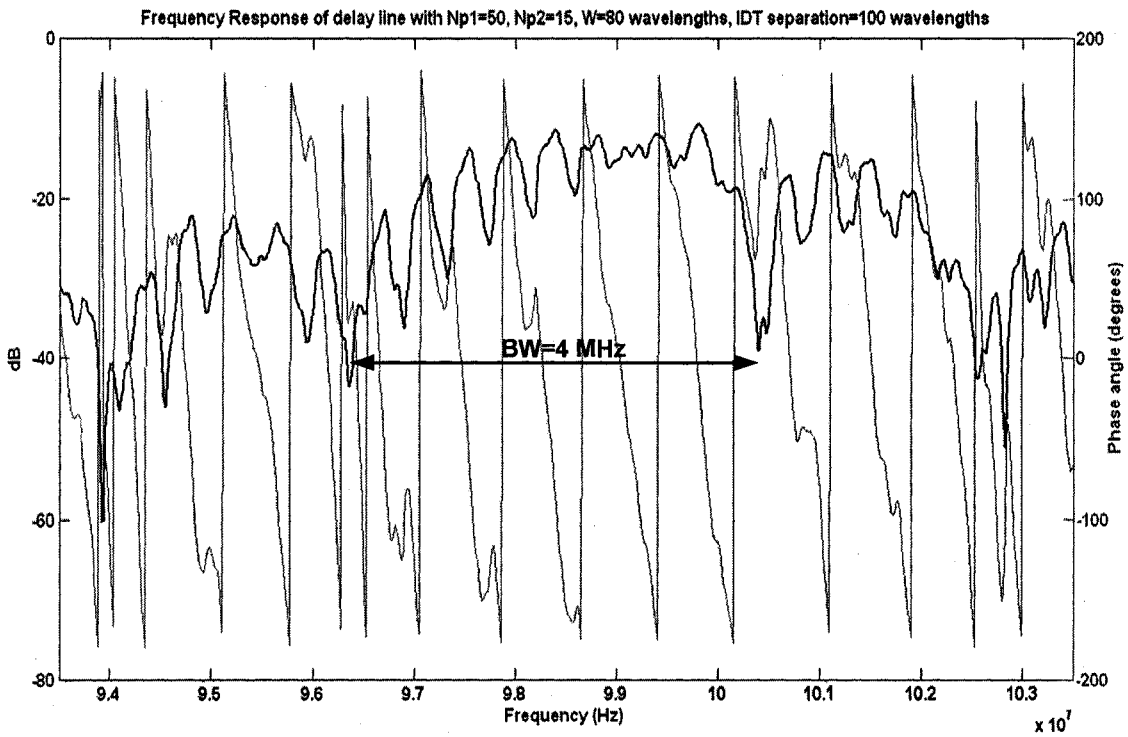

Figure 5.11: Frequency response of delay line with Np1=50, Np2=15, W=80λ_o, IDT separation=100λ_o

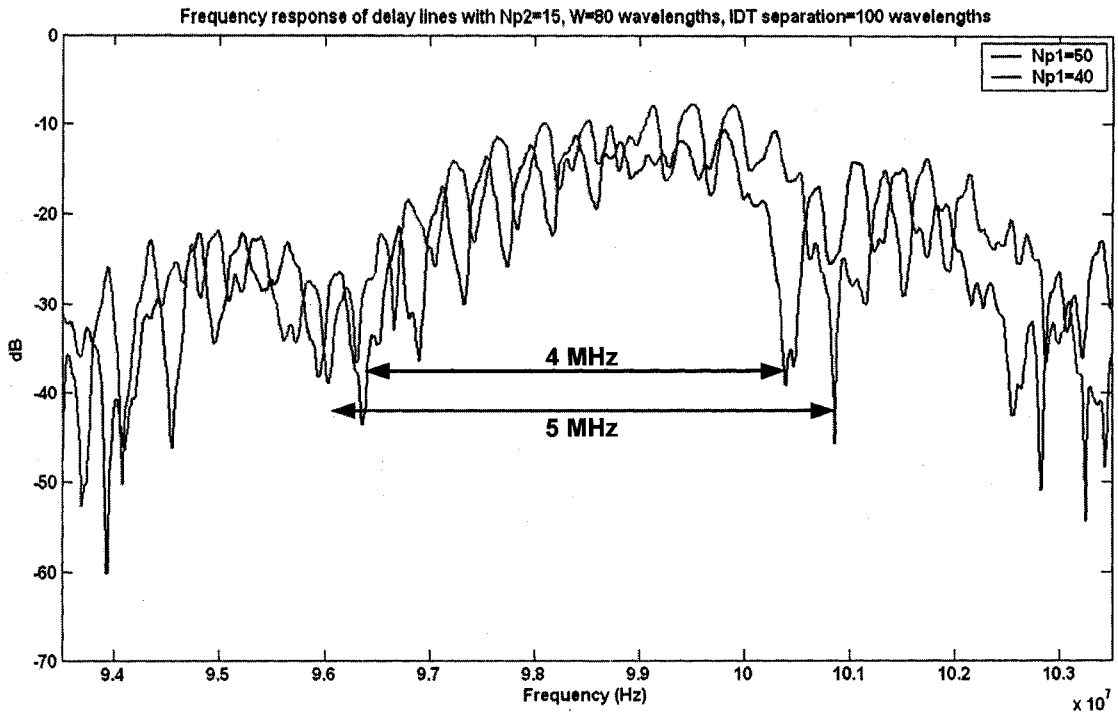

Figure 5.12: Comparison of frequency response of delay lines with different finger pairs in the input IDT

Figure 5.13 shows the measured frequency response of a SAW two-port resonator with a center frequency of 100 MHz. From this figure, it can be seen that the frequency response of a two-port resonator is identical to that of a delay line with an additional resonance peak due to the presence of gratings. In addition, it can be seen that the insertion loss is reduced by almost 7-8 dB due to the reflections from the grating. When the resonator is used as a frequency control element in an oscillator configuration, in addition to the resonance frequency f_0, mode hopping is also possible at frequencies f_1 and f_2 thereby affecting the stability of the oscillator. However, since the relative insertion loss of the device at f_1 and f_2 are almost 8 dB higher than that of f_0, with careful design mode hopping can be eliminated. Using Equation 4-61, the bandwidth between the first nulls can be calculated for this device as 21.05 MHz for N_p=9.5 and f_o=100 MHz. From the measured response, this value was found to be approximately 21 MHz.

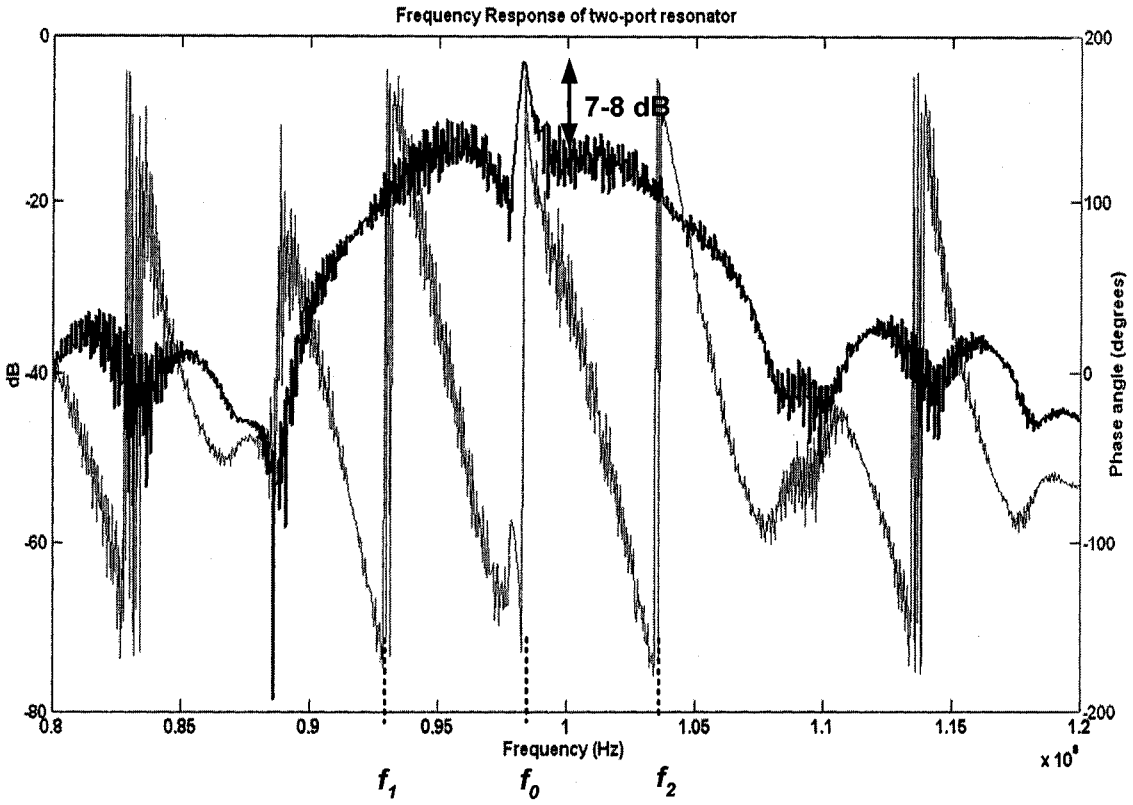

Figure 5.13: Frequency response of the two-port resonator

5.5 Comparison of measured and simulated results

Figure 5.14 shows a comparison of the simulated and measured delay line frequency response. The specifications for the delay line are as follows: number of finger pairs in the input IDT (Np1)=50, number of finger pairs in the output IDT (Np2)=50, acoustic aperture (W)=80λ, separation between IDTs (d)=100λ. It is clear that the simulation models in both MATLAB™ and PSpice Capture™ successfully compare with the actual device. The amplitude of the ripples and the locations of the nulls obtained from simulation results are in good agreement with the measured response. The ripples found in the pass band are attributed to the reflections between fingers of the IDT.

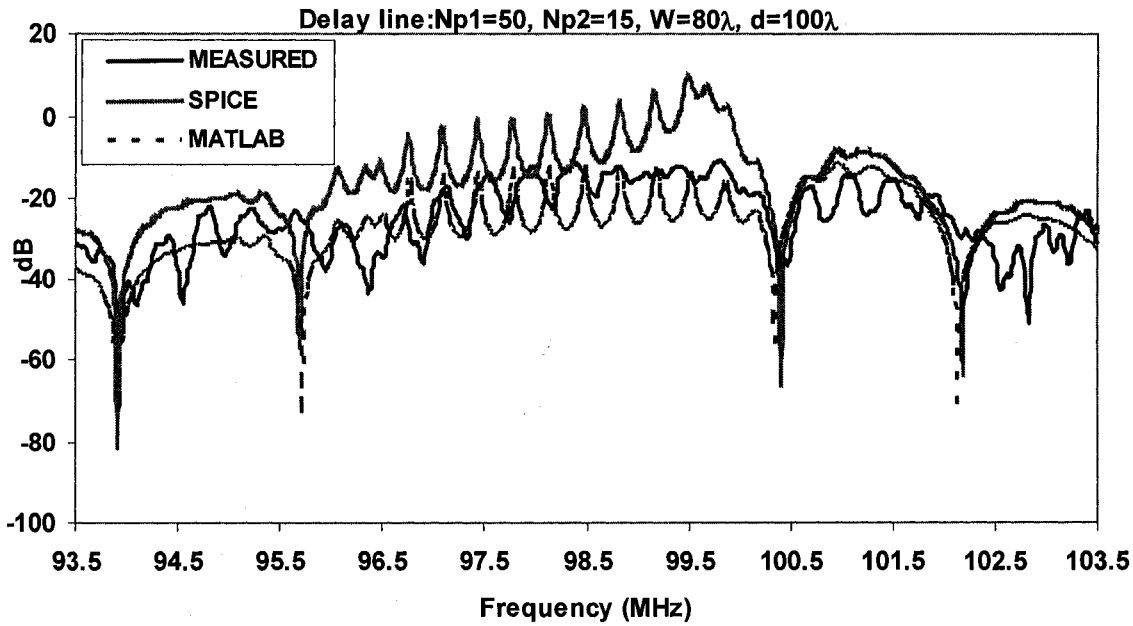

Figure 5.14: Comparison of measured and simulated SAW delay line frequency response

Figure 5.15 shows a similar comparison between the measured and simulated responses but with Np1 changed to 40 instead of 50. It can be seen that the characteristics are almost similar except that in this case the central lobe is wider. This is due to the inverse relationship between the number of finger pairs and bandwidth as discussed earlier. Also from Figure 5.14 and Figure 5.15, it can be seen that MATLAB™ simulation results agree closely with the measured results in terms of the location of the nulls, the insertion loss of the devices and the amplitude of the ripples. Although Orcad PSpice™ results have similar characteristics to that of MATLAB™, the insertion loss is lower compared to MATLAB™ as well as measured results. From Figure 5.14 and Figure 5.15, it can be seen that the difference in insertion loss is 15.7 dB and 13.8 dB for Np1=50 and Np1=40 respectively. In order to better understand the reason for this difference, the author performed simulations on delay lines with different number of finger pairs in the input and output IDT.

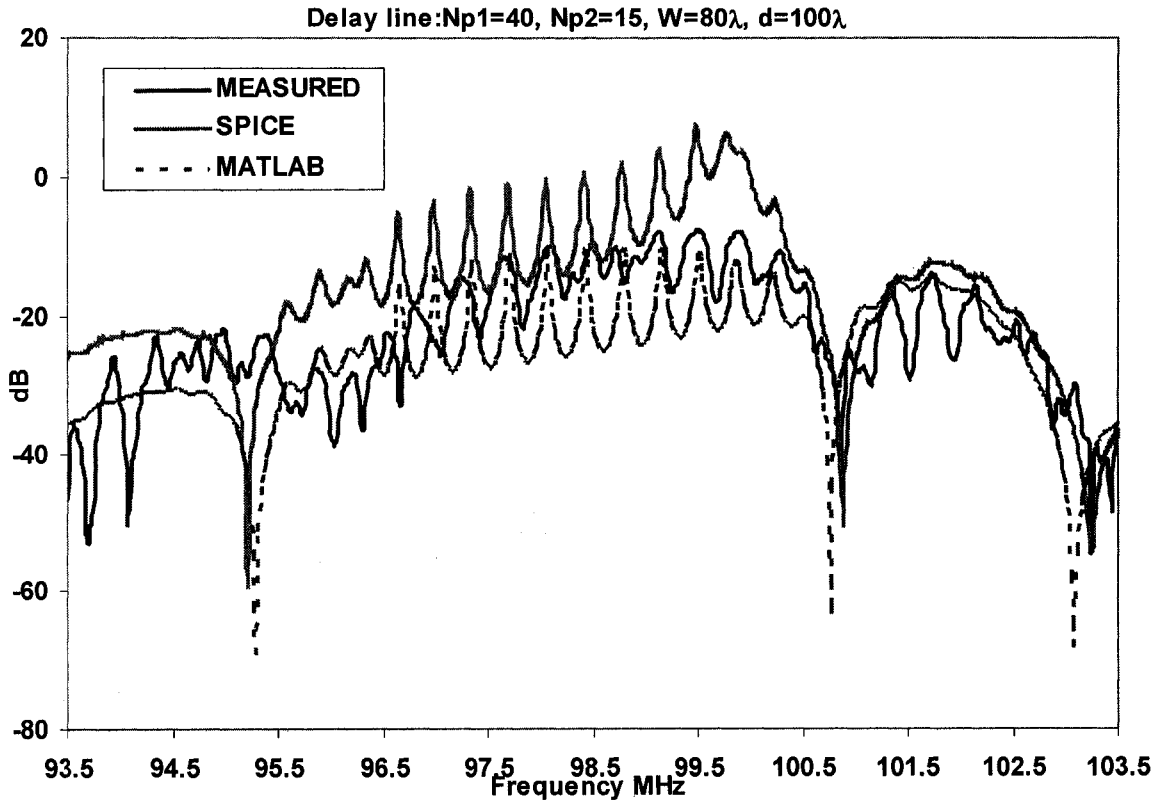

Figure 5.15: Comparison of measured and simulated SAW delay line frequency response

Figure 5.16 shows a comparison of the two methods for (a) 4 finger pairs (b) 8 finger pairs and (c) 16 finger pairs in the input and output IDTs. The separation between the IDTs was maintained at 10λ for each case.

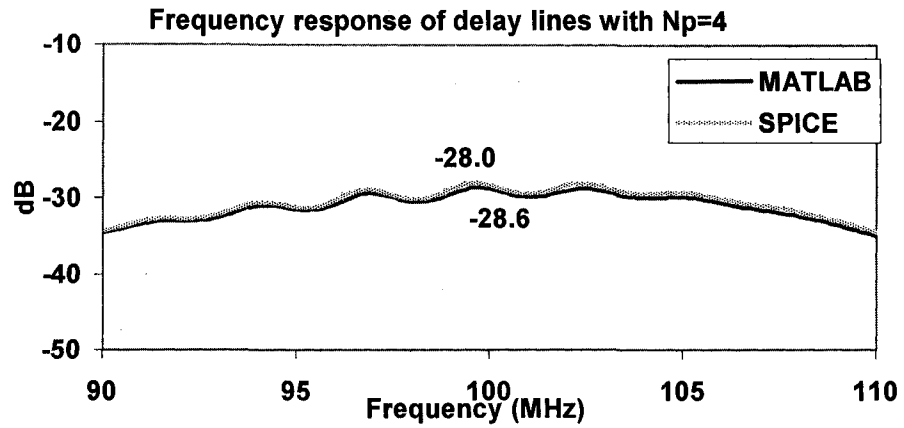

(a)

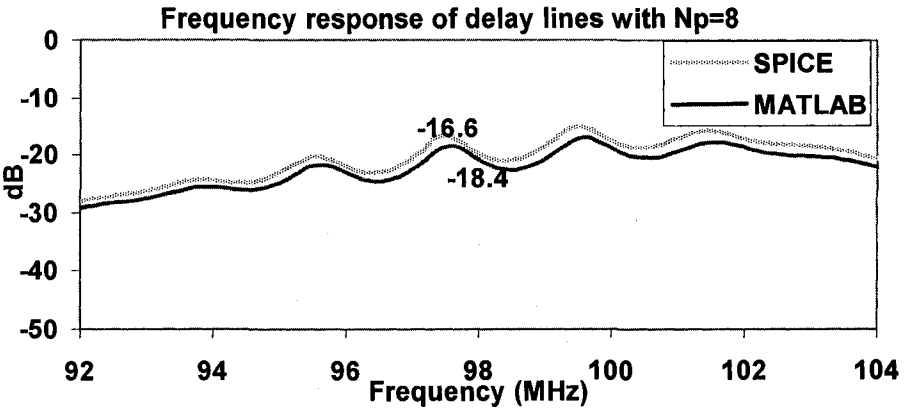

(b)

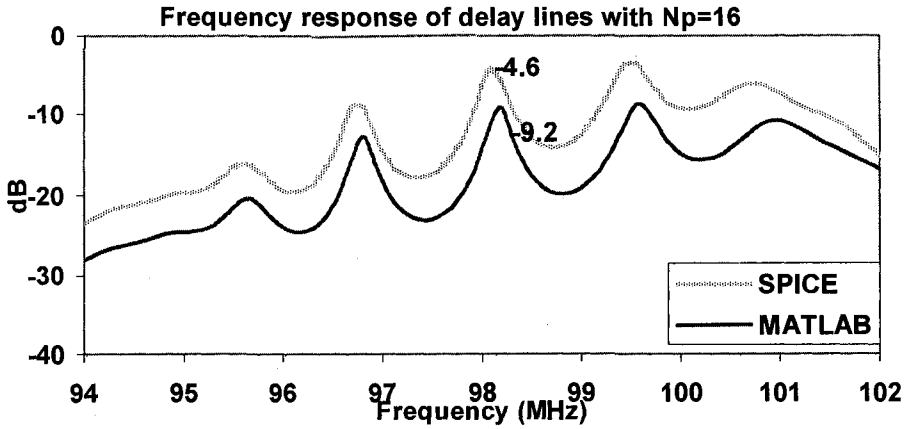

(c)

Figure 5.16: Frequency response comparison of delay line simulated in MATLAB™ and Orcad PSpice™

From the figure, it can be seen that the difference between the insertion loss from the two methods increases with the number of finger pairs in the input IDT. The difference was found to be 0.6 dB, 1.8 dB and 4.6 dB for delay lines with 4, 8 and 16 finger pairs respectively. This could be attributed to the fact that in Orcad Spice™ uses inductors and capacitors to model the tan and csc elements in each finger and there could be some energy storage effects due to the presence of these elements. This difference is however, a subject of further investigation.

5.6 Summary

This chapter discussed the fabrication procedure for SAW devices and presented measured responses for the same. Also, the measured responses were compared with simulation results obtained. The relative merits and demerits of different simulation techniques with reference to the measured frequency response were provided. The next chapter presents the results obtained from the wireless passive sensing system.

CHAPTER VI

PASSIVE WIRELESS SAW SENSING SYSTEM

6.1 Introduction

The wireless passive system including the interrogation unit and the SAW device were tested for their functionality. The digital controls for the interrogation unit were provided by a Spartan II FPGA prototyping board. Short duration RF burst was sent to the reflective SAW device and the SAW response was processed in the receive section of the interrogation unit. This chapter describes the measurement setup and the results obtained from these tests.

6.2 Measurement set-up

Figure 6.1 shows the block diagram of the experimental set up used for testing the overall wireless SAW system. Experiments were conducted in one of the RF shielded rooms to avoid any unwanted interferences. The transmitter was used to generate a RF burst at 434.42 MHz for a duration of 800 μs. This signal was then transmitted to the SAW reflective delay line through the antenna and the received signal was observed using a Tektronix Oscilloscope. The separation between the interrogation unit and the SAW device was maintained at 1m. The digital controls used for programming the Integrated Synthesizer and also the burst switches were generated using a Spartan II FPGA prototyping board. Figure 6.2 shows a photograph of the experimental setup which includes separate PCBs for the transmit and receive path, Spartan II FPGA prototyping board and the antenna. The following section discusses the results obtained from the tests.

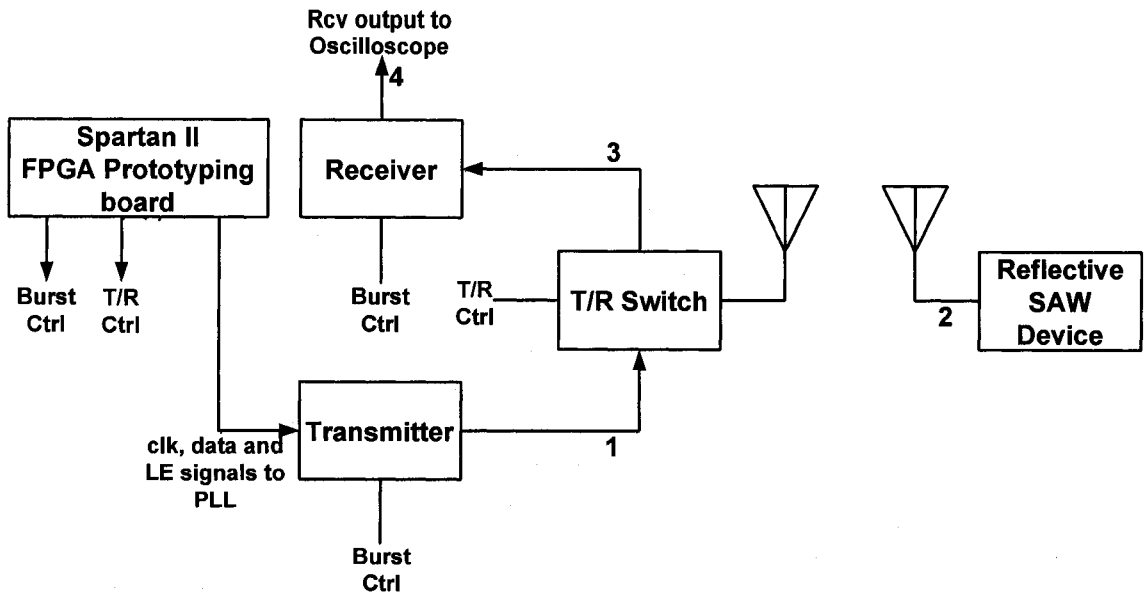

Figure 6.1: Block diagram of the experimental set-up

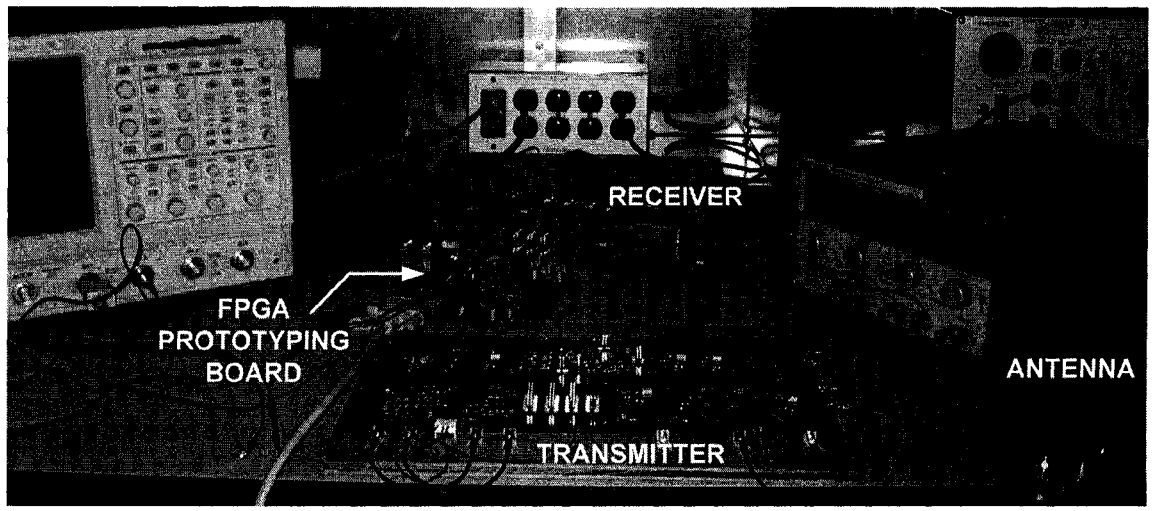

Figure 6.2: Photograph of the experimental set-up

6.3 Results and discussions

Figure 6.3 shows the 800 μs burst signal at the output of the transmitter. The power level of the CW signal at the transmitter output was measured to be 8.2 dBm.

Also, shown in the Figure in Channel 1 is the control signal that was used to generate the burst. The frequency and power level of the signal was measured using the CW signal at the transmitter output to be 434.42 MHz and 8.4 dBm respectively.

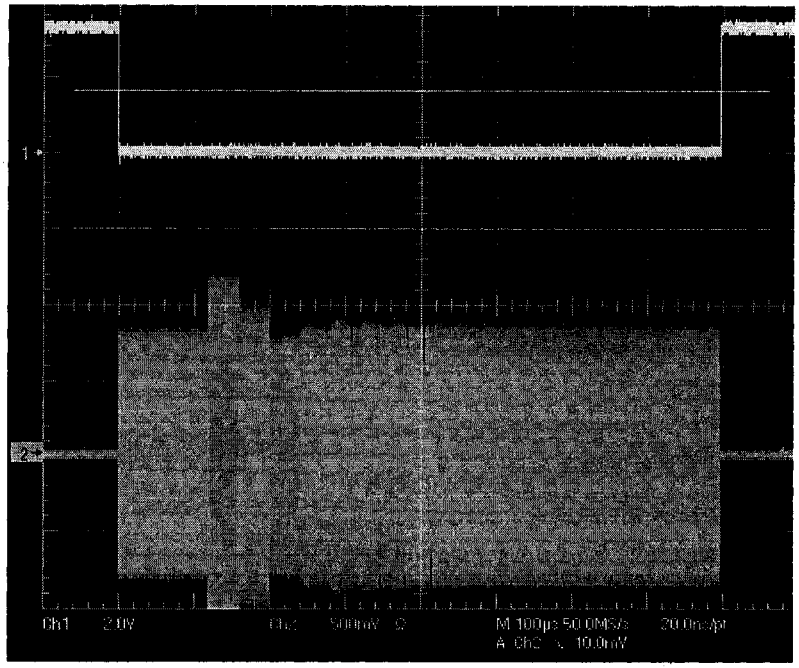

Figure 6.3: 800 μs burst at the transmitter output

Figure 6.4 shows the burst signal at the output of the antenna connected to the sensor side. The power level of the CW signal at the sensor antenna was measured to be -19 dBm. Using the above power levels, the one way path loss was calculated as 27.4 dB which is very close to the expected path loss of 25.2 dB calculated using Frii's equation for a distance of 1m.

Figure 6.5 shows the SAW device response measured at the interrogation unit receiver output. Figure 6.5(a) shows the response of the SAW device when connected directly to the interrogation unit eliminating the wireless path. This was used as a reference to compare the other signal in this figure. Figure 6.5(b) show signals levels observed when the SAW device was placed 1m away from the interrogation unit. The

SAW device consists of uniformly placed reflectors which reflect the incoming acoustic wave back to the input IDT. The multiple lobes observed in the response of Figure 6.5(a) can be attributed to multiple transits of the acoustic wave between the input IDT and the reflectors. Figure 6.5(b) shows similar characteristics except that the signal level is lower due to the path loss between the interrogation unit and the SAW device.

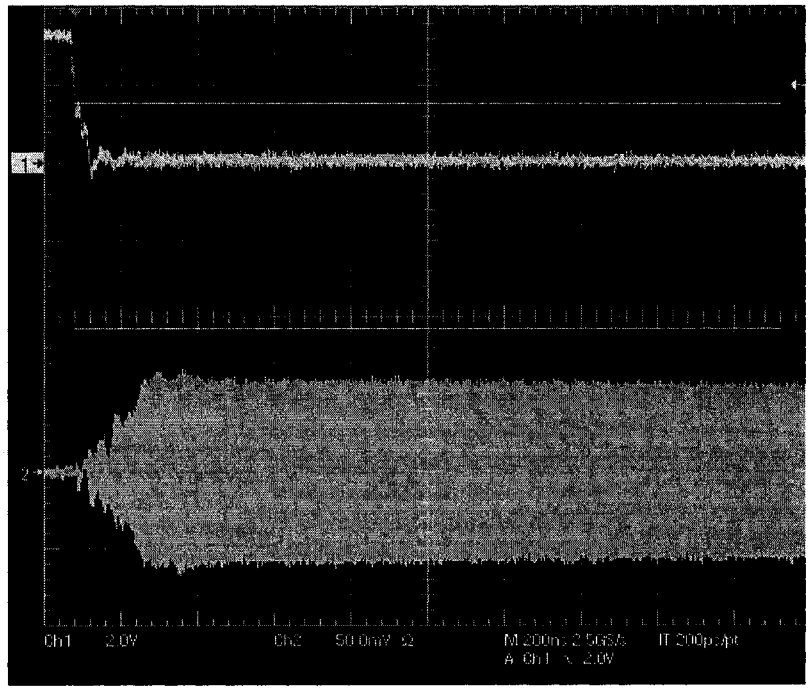

Figure 6.4: Burst signal at the antenna connected to the SAW device

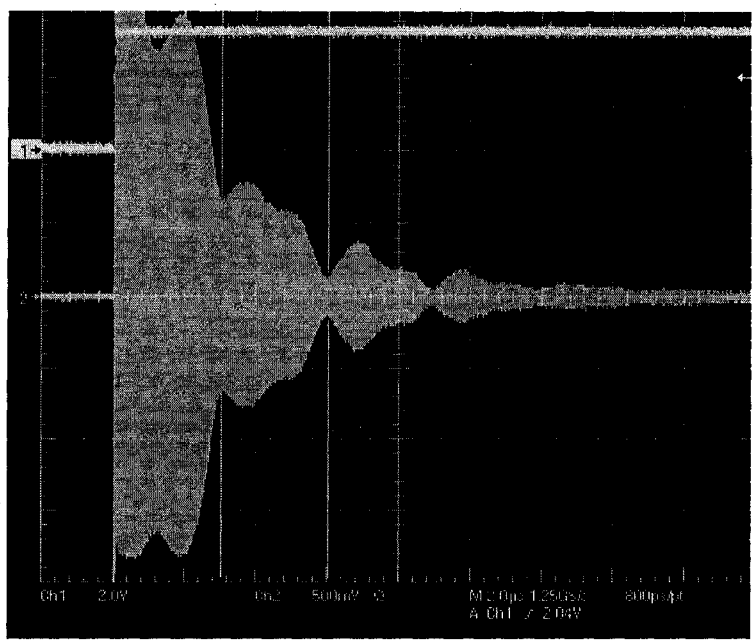

(a)

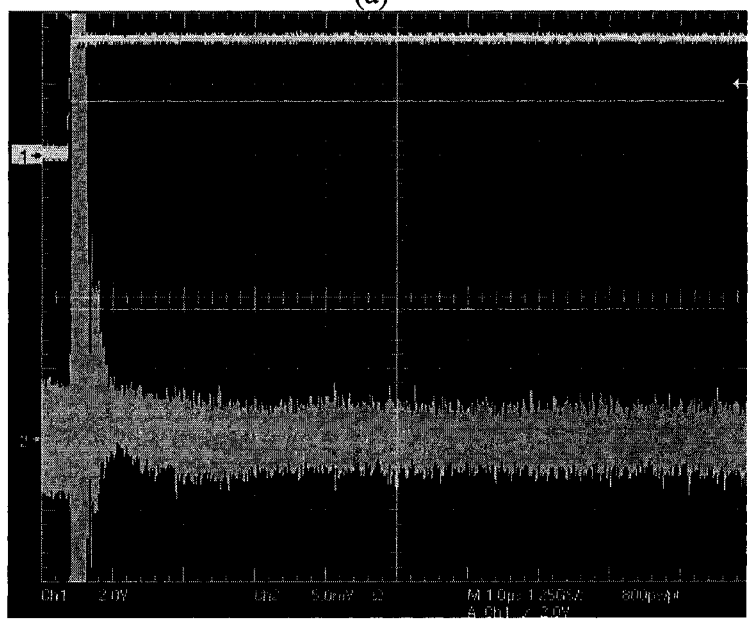

(b)

Figure 6.5: SAW device response at the interrogation unit (a) SAW device response when connected at the output of the interrogation unit without a wireless communication path (used as reference) (b) is the SAW device response measured at the receiver input (c) is the SAW device response measured at the receiver output

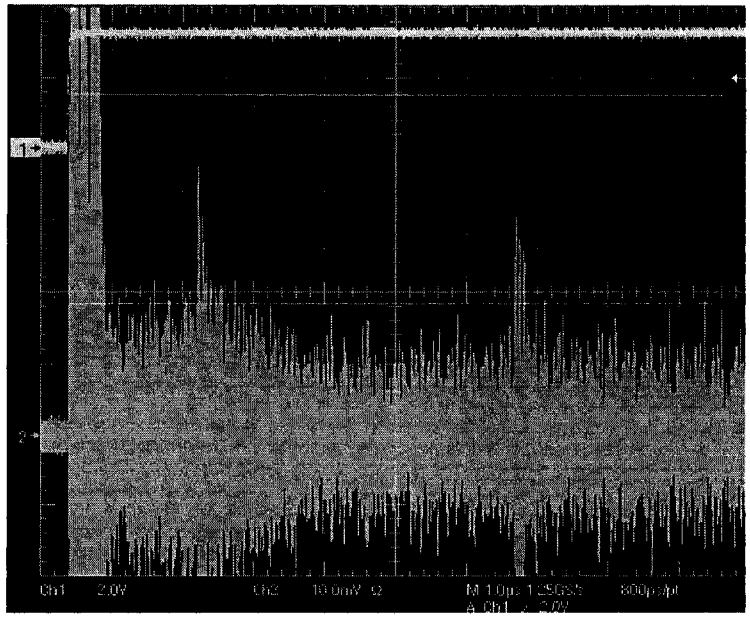

(c)

Figure 6.5-Continued

Table 6.1 shows a comparison between the expected and measured signal powers for the experimental set up shown in Figure 6.1. The stage numbers shown in the table are also marked on the figure for reference. From Figure 3.26, the power level at the output of the transmitter is obtained as +13 dBm. The path loss for a 1m distance was calculated using Equation 3-14 as 25 dB. Based on this the expected power level at the antenna on the sensor side was calculated to be -12 dBm. For a 3 dB device loss, the signal level at the receiver input of the interrogation unit can be calculated to be -40 dBm (=-12-3-25 dBm). Including the +20 dB gain in the receive amplifiers, the signal level at the output of the receive amplifiers can be calculated to be -20 dBm. These power levels were then converted to peak voltages as shown in the table. Also shown in the table are the measured voltage levels at the different stages of the system. The measured values for stages 1 through 4 are taken from Figure 6.3, Figure 6.4, Figure 6.5(b) and Figure 6.5(c) respectively. As is evident from the table, the expected and measured values are in

good agreement with each other.

Table 6.1: Expected and measured signal levels for the wireless system

	(dBm 50 ohm)	(mVpeak)	
Stage	**Exp. Sig. power**	**Expected**	**Measured**
1	13	999	850
2	-12	56	~60
3	-40	2	~2.5
4	-20	22	~20

6.4 Summary

The results obtained from burst tests conducted on the wireless passive SAW system was presented and compared with expected results based on theory. The wireless passive system consists of the interrogation unit and a remote SAW device. The next chapter concludes the dissertation together with some suggestions for future work.

CHAPTER VII

CONCLUSIONS AND FUTURE WORK

7.1 Conclusions

In this work, as a first step, a prototype burst transceiver was built and tested for its functionality and cascaded gain and noise figure tables were obtained. A miniaturized version was then designed and fabricated on a PCB. The overall block diagram and the detailed description of each stage was presented together with measurement results from both continuous wave and burst tests. In addition, cascaded gain and noise figure tables were also presented for the burst transceiver PCB.

SAW delay lines and resonators operating at 100 MHz were designed and fabricated. At the same time, SAW devices were modeled using the finite element method, mason's equivalent circuit and transmission matrix approach in CoventorWare™, Orcad PSpice™ and MATLAB™ respectively. In Orcad PSpice™, the mason's equivalent circuit for each electrode consisted of separate circuits for the free and metallized sections. The equivalent circuit for each electrode was then cascaded to obtain the equivalent circuit for the overall IDT and grating. Similar circuit was also obtained for the delay line and therefore, the overall frequency response of the SAW device was simulated. Similarly, in MATLAB™, the transmission matrices for individual electrode sections were cascaded to obtain the overall response of the SAW device. In both MATLAB™ and Orcad PSpice™, the effect of finger reflections on the frequency response was taken into account in the simulations. The locations of the nulls, the insertion loss and the magnitude of the ripples were successfully simulated in MATLAB™ and Orcad PSpice™. In CoventorWare™, a complete 3-dimensional view of the wave propagation on the structure can be obtained and it allows the user to probe

every single node in the structure to obtain displacement and potential values.

When it comes to modeling, the transmission matrix approach in MATLAB™ requires an in depth understanding of the device physics as well as the mathematics involved. It also requires derivation of the frequency response of the devices using matrix manipulation. Modeling in Orcad PSpice™ is relatively simpler once the values of the tan and cosec elements for each finger are determined. CoventorWare™ modeling is the easiest since only the design parameters have to be known in order to be able to get the 3-dimensional model. However, it requires careful rotation of the model to obtain the required orientation and also optimization of the mesh element sizes in order to be able to compare with the measured responses. In addition, it requires a faster processor and a large memory for the successful completion of the simulations. In terms of computational time, MATLAB™ was observed to be fastest and only takes a few minutes when compared to a few hours for both Orcad PSpice™ and CoventorWare™.

7.2 Suggestions for future work

Some suggestions for future work include:

1. Being able to use CoventorWare™ to successfully model SAW devices in order to get a better agreement between measured and simulated responses.
2. Using the results from these simulations to successfully design and fabricate a second generation of smart SAW sensors with built in signal processing capabilites and integrated antenna whose schematic is shown in Figure 7.1. The power supply unit consists of energy scavenging circuitry which charges a battery. The sensor drive circuitry triggers the SAW sensor and the RF transmitter when an interrogation signal is received. The response of the sensor is therefore amplified in the RF transmitter before being sent back to the interrogation unit. This will extend the operating range of the wireless system.

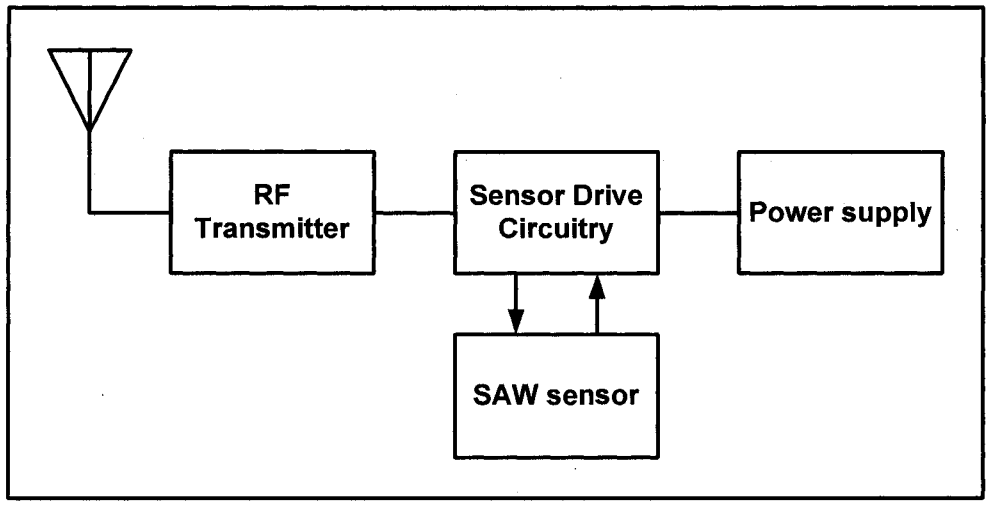

Figure 7.1: Smart sensor schematic with integrated signal processing capabilities

3. Testing the interrogation unit along with the fabricated integrated smart sensor
4. Once the second generation of devices are fabricated and tested, they can be evaluated in a real time sensing scenario.

Appendix A

VHDL Code to Program the PLL and the Burst Switches

The VHDL code that was written to program the PLL and the burst switches in the exact order is given below:

```
library IEEE;
use IEEE.STD_LOGIC_1164.ALL;
use IEEE.STD_LOGIC_ARITH.ALL;
use IEEE.STD_LOGIC_UNSIGNED.ALL;

entity pll is
   Port ( start : in std_logic;
                clk : in std_logic;
          le : out std_logic;
          data : out std_logic;
                                burst1: out std_logic;
                                burst2: out std_logic;
                                led : out std_logic_vector(6 downto 0);
                                clkout : out std_logic);
end pll;

architecture Behavioral of pll is
signal r_cntr: std_logic_vector(23 downto 0):= "000001000000011001000001";
signal   ctrl: std_logic_vector(23 downto 0):= "000011111111000101000100";
signal n_cntr: std_logic_vector(23 downto 0):= "000100001111100000000010";
signal i:integer:=0;
signal done:std_logic;
begin
process(start, clk)
begin

if clk'event and clk='0' then
if start='1' then
if i<=23 then
  done<='1';
  burst1<='1';
  burst2<='1';
  le<='0';
  led<="1111110";
  data<=r_cntr(23-i);  --loading data into the R counter
  i<=i+1;
elsif i=24 then
  le<='1';
  done<='1';
  i<=i+1;
elsif i>24 and i<=48 then
  le<='0';
  led<="1100101";
  done<='1';
  data<=ctrl(48-i);    --loading data into the Control register
```

```
  i<=i+1;
elsif i=49 then
  le<='1';
  done<='1';
  i<=i+1;
elsif i>49 and i<=2000049 then
  le<='0';
  done<='0';
  i<=i+1;
elsif i>2000049 and i<=2000073 then
  led<="1110110";
  data<=n_cntr(2000073-i);  --loading data into the N counter
  done<='1';
  i<=i+1;
elsif i=2000074 then
  le<='1';
  done<='1';
  i<=i+1;
elsif i>2000074 and i<2001674 then
  le<='0';
  done<='0';
  led<="1111111";
  burst1<='0';    --generating the burst after PLL is programmed
  burst2<='0';
  i<=i+1;
elsif i=2001674 then
  le<='0';
  done<='0';
  led<="0011111";  --burst signal is turned OFF
  burst1<='1';
  burst2<='1';
  i<=i+1;
end if;
elsif start='0' then
  i<=0;
  done<='0';
  le<='0';
  burst1<='1';
  burst2<='1';
end if;
end if;
end process;
clkout<=clk and done;
end Behavioral;
```

Appendix B

MATLAB™ Code to Simulate the Frequency Response of SAW Delay Line Using the Transmission Matrix Approach

The MATLAB™ that was written to simulate the frequency response of the SAW delay line using the transmission matrix approach including the effects of metallization on the substrate is given below:

```
%Simulation of the frequency response of SAW delay line using the
%transmission matrix approach.
%Program written by Sridevi Krishnamurthy
clear all;
close all;
Vs=3488; %SAW velocity on the free sections of YZ-LiNbO3 substrate
Vm=3353.0924; %SAW velocity on the metallized sections of YZ-LiNbO3 substrate
%with metallization height 200nm and wavelength 34.88um
Co=4.6e-10; %Capacitance per finger pair per unit length on YZ-LiNbO3 substrate
K2=0.045; %Electromechanical coupling coefficient for YZ-LiNbO3 substrate

lambdao=34.88e-6; %SAW wavelength
fo=Vs/lambdao;
W=80*lambdao; %Acoustic aperture
d=127.75*lambdao; %Length of the delay line


fm=Vm/lambdao;
df=0.125*lambdao;
dm=0.25*lambdao;
Zo=1/(fo*Co*W*K2); %acoustic impedance for the free sections
Zm=1/(fm*Co*W*K2) %acoustic impedance for the metallized sections
%Zm=169.66e3;

Nt1=80; %Number of electrodes in the input IDT
Nt3=30;  %Number of electrodes in the output IDT
h=200e-9;
k11=(0.018+(0.3*h/lambdao))*(2*pi/lambdao); %Self coupling coefficient for YZ-LiNbO3 substrate

i=1;
for f=93.5e6:10e6/799:103.5e6
   lambda=Vs/f;
   omega=2*pi*f;

   %computing the ABCD matrix for a single finger
   thetaf=2*pi*f*df/Vs;
   thetam=2*pi*f*dm/Vm;
   Af=cos(thetaf);
   Bf=sqrt(-1)*Zo*sin(thetaf);
   Cf=sqrt(-1)*sin(thetaf)/Zo;
   Df=cos(thetaf);
   Am=cos(thetam);
   Bm=sqrt(-1)*Zm*sin(thetam);
```

```
Cm=sqrt(-1)*sin(thetam)/Zm;
Dm=cos(thetam);
Afinger=[Af Bf;Cf Df]*[Am Bm;Cm Dm]*[Af Bf;Cf Df];
Ase=Afinger(1,1);
Bse=Afinger(1,2);
Cse=Afinger(2,1);
Dse=Afinger(2,2);
thetae=acos(Ase);
Ze=Bse/(sqrt(-1)*sin(thetae));

%computing the 2x2 matrix for a single finger in the IDT
t11=0.5*(2*Ase+(Bse/Zo)+Zo*Cse);
t12=0.5*(Zo*Cse-(Bse/Zo));
t13=((sqrt(-1)*tan(thetae/2)*(Zo^0.5))/(2*Ze))*(-Ase-1-(Bse/Zo));
t21=-t12;
t22=conj(t11);
t23=sqrt(-1)*tan(thetae/2)*(Zo^0.5)*(1+Ase-(Bse/Zo))/(2*Ze);
t31=2*t13;
t32=-2*t23;
t33=sqrt(-1)*omega*Co*W*0.5+sqrt(-1)*2*(tan(thetae/2)/Ze)-sqrt(-1)*(sin(thetae)*(tan(thetae/2)^2))/Ze;

%computing the 2x2 IDT matrix
t1=[t11 t12;t21 t22]^Nt1;
t3=[t11 t12;t21 t22]^Nt3;


t111=t1(1,1);
t113=t3(1,1);
t121=t1(1,2);
t123=t3(1,2);
t211=t1(2,1);
t213=t3(2,1);
t221=t1(2,2);
t223=t3(2,2);

Bp=[t13;t23]+[t11 t12;t21 t22]*[-t13;-t23];
Cp=[t31 t32]*[t11 t12;t21 t22]+[-t31 -t32];
t33p=2*t33+[t31 t32]*[-t13;-t23];
Tp=[t11 t12;t21 t22]^2;

tauin=[0;0];
tauprimein=[0 0];
tauout=[0;0];
tauprimeout=[0 0];
t333=(Nt3/2)*t33p;
t331=(Nt1/2)*t33p;

%computing t13, t23, t31, t32, t33 values for the overall IDT
for i1=1:(Nt1/2)
   tauin=tauin+(Tp^(i1-1))*Bp;
   tauprimein=tauprimein+Cp*Tp^(i1-1);
   t331=t331+((Nt1/2)-i1)*Cp*Tp^(i1-1)*Bp;
end
for i2=1:(Nt3/2)
   tauout=tauout+(Tp^(i2-1))*Bp;
   tauprimeout=tauprimeout+Cp*Tp^(i2-1);
   t333=t333+((Nt3/2)-i2)*Cp*Tp^(i2-1)*Bp;
end
t131=tauin(1,1);
t133=tauout(1,1);
t231=tauin(2,1);
t233=tauout(2,1);
```

```
    t311=tauprimein(1,1);
    t313=tauprimeout(1,1);
    t321=tauprimein(1,2);
    t323=tauprimeout(1,2);

    %computing the matrix elements for the delay path
    thetad=2*pi*f*d/Vs;
    Ad=cos(thetad);
    Bd=sqrt(-1)*Zo*sin(thetad);
    Cd=sqrt(-1)*sin(thetad)/Zo;
    Dd=cos(thetad);
    thetaed=acos(Ad);
    Ze=Bd/(sqrt(-1)*sin(thetaed));
    d11=0.5*(2*Ad+(Bd/Zo)+Zo*Cd);
    d12=0.5*(Zo*Cd-(Bd/Zo));
    d21=-d12;
    d22=0.5*(2*Ad-(Bd/Zo)-Zo*Cd);
    d2=[d11 d12;d21 d22];

    m=t1*d2*t3;
    k=t1*d2*[t133;t233];
    p=[t311 t321]*d2*t3;
    l=[t311 t321]*d2*[t133;t233];

    %computing y-parameters for the SAW delay line
    y11(i)=t331-(p(1,1)*t131/m(1,1));
    y21(i)=-t313*t131/m(1,1);
    y12(i)=l(1,1)-(p(1,1)*k(1,1)/m(1,1));
    y22(i)=t333-(t313*k(1,1)/m(1,1));

    %computing s21 using the y-parameters
    s21(i)=-2*y21(i)/((1+y11(i))*(1+y22(i))-y12(i)*y21(i));
    s12(i)=-2*y12(i)/((1+y11(i))*(1+y22(i))-y12(i)*y21(i));
    s11(i)=((1-y11(i))*(1+y22(i))+y12(i)*y21(i))/((1+y11(i))*(1+y22(i))-y12(i)*y21(i));
    s22(i)=((1+y11(i))*(1-y22(i))+y12(i)*y21(i))/((1+y11(i))*(1+y22(i))-y12(i)*y21(i));

    z11=((1+s11(i))*(1-s22(i))+s12(i)*s21(i))/((1-s11(i))*(1-s22(i))-s12(i)*s21(i));
    z12=2*s12(i)/((1-s11(i))*(1-s22(i))-s12(i)*s21(i));
    z21=2*s21(i)/((1-s11(i))*(1-s22(i))-s12(i)*s21(i));
    z22=((1-s11(i))*(1+s22(i))+s12(i)*s21(i))/((1-s11(i))*(1-s22(i))-s12(i)*s21(i));

    %modified s-parameter including source and load impedance
    s21new(i)=-50*z12/(z12^2-(z11+50)*(z22+50));
    i=i+1;
end


f=93.5e6:10e6/799:103.5e6;
figure(1);
[ax,h1,h2]=plotyy(f,20*log10(abs(s21new)),f,angle(s21new)*180/pi);
title('Frequency Response of delay line with Np1=50');
xlabel('Frequency (MHz)');
set(h1,'LineWidth',2)
set(h2,'LineWidth',0.5)
set(get(ax(1),'Ylabel'),'String','dB')

        set(get(ax(2),'Ylabel'),'String','Phase angle (degrees)')
```

Appendix C

Procedure to Determine the Component Values of the Tan and Csc Elements in the Mason's Equivalent Circuit for a Single Finger

Consider a delay line with the following specifications for the free section: Z_o=173126Ω, $\phi_n = \frac{\pi\omega}{2\omega_o}$, $\omega_o = 2\pi f_o$, where f_o=100MHz. Let us now derive the component values for the element $jZ_o \tan\left(\frac{\phi_n}{2}\right)$. In terms of the first three poles and zeros, this element can be expressed as

$$Z_{in} = jZ_o \tan\left(\frac{\phi_n}{2}\right) = j\omega H \frac{\left(\omega^2 - \omega_3^2\right)\left(\omega^2 - \omega_5^2\right)}{\left(\omega^2 - \omega_2^2\right)\left(\omega^2 - \omega_4^2\right)\left(\omega^2 - \omega_6^2\right)} \qquad \textbf{Equation C-1}$$

where the zeros are *0*, ω_3, ω_5 and the poles are ω_2, ω_4, ω_6 and H is a scaling factor. The zeros can be determined using the following equation:

$$\frac{\phi_n}{2} = \frac{\pi\omega}{4\omega_o} = n\pi \qquad \textbf{Equation C-2}$$

giving $\omega_3 = 4\omega_o$, $\omega_5 = 8\omega_o$. The poles are obtained as follows:

$$\frac{\phi_n}{2} = \frac{\pi\omega}{4\omega_o} = \frac{n\pi}{2} \qquad \textbf{Equation C-3}$$

where n is odd. This gives $\omega_2 = 2\omega_o$, $\omega_4 = 6\omega_o$, $\omega_6 = 10\omega_o$. Also, we know that at $\omega = \omega_o$, $Z_{in} = jZ_o$. Using this condition the value of H can be obtained using Equation C-1. Now the values of the capacitors are determined using the following relation:

$$C_n = \frac{-j\omega}{Z_{in}\left(\omega^2 - \omega_n^2\right)}, \omega = \omega_n \qquad \textbf{Equation C-4}$$

where n is either 2, 4 or 6. Once the values of capacitors are calculated, the values of inductors are determined using the following equation:

$$L_n = \frac{1}{\omega_n^2 C_n} \qquad \textbf{Equation C-5}$$

For the above delay line design, the values of *Ls* and *Cs* for the element

$jZ_o \tan\left(\frac{\phi_n}{2}\right)$ were calculated to be

L_2= 88.7966149 μH

C_2=1.78288722×10^{-3} pF

L_4=11.5106723 μH

C_4=1.52818904×10^{-3} pF

L_6=7.45891565 μH

C_6=0.848993912×10^{-3} pF

Similarly the values of the csc elements are obtained by adding two tan elements and using the above steps to calculate the value for each tan element.

Appendix D

List of Publications

D.1 Book Chapter

- Massood Z. Atashbar, Sridevi Krishnamurthy, "Surface Acoustic Wave Sensors and their Wireless Applications" in Encyclopedia of Sensors, Vol. 10, Edited by C. A. Grimes, E. C. Dickley, and M. V. Pishko, American Scientific Publishers, 2006.
- M.Z. Atashbar, S. Krishnamurthy "Sensing and sampling strategies", in Comprehensive Sensor Technology, J. Watson and N. Hancock , J. Schwank (ed.), Elsevier (submitted).
- M.Z. Atashbar, S. Krishnamurthy "Basic principles of chemical sensor operation", in Comprehensive Sensor Technology, J. Watson, N. Hancock, and J. Schwank (ed.), Elsevier (submitted).

D.2 Journal Papers

- M. Z. Atashbar, B. J. Bazuin, M. Simpeh and S. Krishnamurthy, "3D FE simulation of H_2 SAW gas sensor", Sensors and Actuators B, Vol. 111-112, pages 213-218, 2005.
- M. Z. Atashbar, B. J. Bazuin and S. Krishnamurthy, "Performance Evaluation of SAW Devices by Simulation", International Journal of Modeling and Simulation, Vol. 24, pages 250-263, 2004.

D.3 Conference Presentations

- S. Krishnamurthy, M. Atashbar and K. Kalantar-Zadeh, "3D modeling and simulation of SH-SAW devices using the Finite Element Method", IEEE Sensors 2007, Atlanta, GA (accepted).

- S. Krishnamurthy, B. J. Bazuin and M. Z. Atashbar, "Wireless SAW sensors reader: architecture and design", Proceedings of the IEEE/EIT Conference, Lincoln, Nebraska, May 22-25, 2005.
- M. Z. Atashbar, B. Bazuin, M. Simpeh and S. Krishnamurthy, "3-Dimensional finite element simulation of acoustic wave propagation in SAW metallic thin film gas sensors", Eurosensors, Rome, Italy, September 13-15, pages 700-701, 2004.
- M. Z. Atashbar, B. J. Bazuin, M. Simpeh and S. Krishnamurthy, "3-D finite element simulation model of SAW Palladium thin film Hydrogen sensors", IEEE Conference on Ultrasonics, Ferroelectrics and Frequency Control, Montreal, Canada, August 23-27, pages 549-553, 2004.
- B. J. Bazuin, M. Z. Atashbar and S. Krishnamurthy, "A Prototype Burst Transceiver for SAW Sensors Interrogation", Proceedings of the International Conference on Intelligent Sensing and Information Processing, Chennai, India, January 4-7, pages 190-195, 2004.
- M. Z. Atashbar, B. J. Bazuin and S. Krishnamurthy, "Design and Simulation of SAW Sensors for Wireless Sensing", Proceedings of the IEEE Sensors Conference, Toronto, Canada, October 21-24, pages 584-589, 2003.
- B. J. Bazuin, M. Z. Atashbar and S. Krishnamurthy, "A Prototype Burst Transceiver for Smart SAW Sensors", Proceedings of the IEEE/EIT Conference, Indianapolis, Indiana, June 5-6, 2003

REFERENCES

[1] Lord Rayleigh, "On Waves Propagating along the Plane Surface of an Elastic Solid", Proceedings of the London Mathematical Society, Vol. 17, pages 4-11, 1885.

[2] Morgan D. P., "History of SAW Devices", Proceedings of the IEEE International Frequency Control Symposium, pages 439-460, 1998.

[3] Mortley W. S., "Pulse Compression by Dispersive Gratings on Crystal Quartz", The Marconi Review, Vol. 159, pages 273-290, 1965.

[4] Mortley W. S., British Patent 988, 102, 1963.

[5] Rowen J. H., U.S. Patent 3, 289, 114, 1963.

[6] White R. M. and Voltmer F. W., "Direct Piezoelectric Coupling to Surface Elastic Waves", Applied Physics Letters, Vol. 7, pages 314-316, 1965.

[7] Tancrell R. H., Schulz M. B., Barrett H. H., Davies L. and Holland M. G., "Dispersive Delay Lines using Ultrasonic Surface Waves", Proceedings of the IEEE, Vol. 57, pages 1211-1213, 1969.

[8] Hartemann P. and Dieulesaint E., Electronics Letters, Vol. 5, pages 657-658, 1969.

[9] Chauvin D., Coussot G. and Dieulesaint E., "Acoustic Surface-Wave Television Filters", Electronics Letters, Vol. 7, pages 491-492, 1971.

[10] Marshall F. G. and Paige E. G. S., Electronics Letters, Vol. 7, pages 460-464, 1971.

[11] Marshall F. G., Newton C. O. and Paige E. G. S., "Surface Acoustic Wave Multistrip components and their Applications", IEEE Transactions on Microwave Theory and Techniques, Vol. 21, pages 216-225, 1973.

[12] Hartmann C. S., "Weighting Interdigital Surface Wave Transducers by Selective Withdrawal of Electrodes", Proceedings of the IEEE Ultrasonics Symposium, pages 423-426, 1973.

[13] Maines J. D., Paige E. G. S., Saunders A. F., and Young A. S., Electronics Letters, Vol.

5, pages 678-689, 1969.

[14] Staples E. J., Schoenwald J. S., Rosenfeld R. C. and Hartmann C. S., "UHF Surface Acoustic Wave Resonators", Proceedings of the IEEE Ultrasonics symposium, pages 245-252, 1974.

[15] Luukkala M. and Kino G. S., "Convolution and Time Inversion using Parametric Interactions of Acoustic Surface Waves", Applied Physics Letters, Vol. 18, pages 393-394, 1971.

[16] Tancrell R. H. and Holland M. G., "Acoustic Surface Wave Filters", Proceedings of the IEEE, Vol. 59, pages 393-409, 1971.

[17] Smith W. R., Gerard H. M., Collins J. H., Reeder T. M. and Shaw H. J., "Analysis of Interdigital Surface Wave Transducers by use of an Equivalent Circuit Model", IEEE Transactions on Microwave Theory and Techniques, Vol. 17, pages 856-864, 1969.

[18] Abbott B. P., Hartmann C. S. and Malocha D. C., "A Coupling-Of-Modes Analysis of Chirped Transducers containing Reflective Electrode Geometries", Proceedings of the IEEE Ultrasonics Symposium, pages 129-134, 1989.

[19] M. Z. Atashbar, B. J. Bazuin and S. Krishnamurthy, "Performance Evaluation of SAW Devices by Simulation", International Journal of Modeling and Simulation, Vol. 24, pages 250-263, 2004.

[20] Milsom R. F., Reilly N. H. C. and Redwood M., "Analysis of Generation and Detection of Surface and Bulk Acoustic Waves by Interdigital Transducers", IEEE Transactions on Sonics and Ultrasonics, Vol. SU-24, No. 3, May 1977.

[21] Peach R. C., "A General Green Function Analysis for SAW Devices", Proceedings of the IEEE Ultrasonics Symposium, pages 221-225, 1995.

[22] Griffiths D. A., Jacoby B., Swain A., Ballantine D. and Newman J. D., "Applications and Markets for Biosensors in the 1990s".

[23] Turner A. P. F. (Editor), "Advances in Biosensors. A Research Annual", Vol. 2, Jai Press Ltd, London, 1992.

[24] Mason W. P., "Measurement of the Viscosity and Shear Elasticity of Liquids by Means of a Torsionally Vibrating Crystal", Proceedings A.S.M.E, pages 359-370, May 1947.

[25] Wohltjen H. and Dessy R., "Surface Acoustic Wave Probe for Chemical Analysis", Analytical Chemistry, Vol. 51, No. 9, 1979.

[26] Wohltjen H., "Surface Acoustic Wave Microsensors", Proceedings of Transducers'87, pages 471-477, 1987.

[27] Vellekoop M. J., "A Smart Lamb-Wave Sensor System for the Determination of Fluid Properties", Ph. D Thesis, Delft University, The Netherlands, 1994.

[28] Grate J. W., Martin S. J. and White R. M., "Acoustic Wave Micro sensors-Part 1", Analytical Chemistry, Vol. 65, No. 21, pages 940A-948A, 1993.

[29] Campbell C. K., "Surface Acoustic Wave Devices for Mobile and Wireless Communications", Academic Press Inc., 1998.

[30] Dill R., Ruile W. and Lewis B., "The Splitfinger Directional Transducer (SFDT): A New Single Phase Unidirectional Transducer", Proceedings of the IEEE Ultrasonics Symposium, pages 147-150, 1994.

[31] Hanma K. and Hunsinger B. J., "A Triple Transit Suppression Technique", Proceedings of the IEEE Ultrasonics Symposium, pages 328-331, 1976.

[32] Wright P. V., "The Natural Single-Phase Unidirectional Transducer: A New Low-Loss SAW Transducer", Proceedings of the IEEE Ultrasonics Symposium, pages 58-63, 1985.

[33] Mitchell R. F., "Spurious Bulk Wave Signals in Acoustic Surface Wave Devices", Proceedings of the IEEE Ultrasonics Symposium, pages 313-320, 1974.

[34] Marshall F. G., Newton C. O. and Paige E. G. S., "Surface Acoustic Wave Multistrip Components and Their Applications", IEEE Transactions on Microwave Theory and Techniques, Vol. 21, No. 4, pages 216-225, 1973.

[35] Naraine P. M., Campbell C. K., "Gigahertz SAW Filters on YZ-Lithium Niobate Without the Use of Sub-Micron Line Widths", Proceedings of the IEEE Ultrasonics Symposium, pages 93-96, 1984.

[36] Naraine P. M., Campbell C. K. and Ye Y., "A SAW Step-Type Delay Line for Efficient High-Order Harmonic Mode Excitation", Proceedings of the IEEE Ultrasonics Symposium, pages 322-325, 1980.

[37] Campbell C. K., Smith P. M., Saw C. B. and Naraine P. M., "Design of a Harmonic-Mode SAW Delay Line with Split-Electrode and Stepped-Finger Geometry", Proceedings of the IEEE Ultrasonics Symposium, Vol. 1, pages 43-46, 1986.

[38] Morgan D. P., "History of SAW Devices", Proceedings of the IEEE International Frequency Control Symposium, pages 439-460, 1998.

[39] Reindl L., Scholl G., Ostertag T., Scherr H., Wolff U. and Schmidt F., "Theory and Application of Passive SAW Radio Transponders as Sensors", IEEE Transactions on Ultrasonics, Ferroelectrics and Frequency Control, Vol. 45, No. 5, pages 1281-1292, 1998.

[40] Bell Jr. D. T. and Li R. C. M., "Surface Acoustic Wave Resonators", Proceedings of the IEEE, Vol. 64, No.5, May 1976.

[41] Wright P. V., "A Review of SAW Resonator Filter Technology", Proceedings of the IEEE Ultrasonics Symposium, pages 29-38, 1992.

[42] Grate J. W., Martin S. J. and White R. M., "Acoustic Wave Micro sensors-Part 1", Analytical Chemistry, Vol. 65, No. 21, pages 940A-948A, 1993.

[43] G. Sauerbrey, Zeitschrift für Physik, Vol. 155, pages 206-222, 1959.

[44] Nanto H., Kondo K., Habara M., Douguchi Y., Waite R.I. and Nakazumi H., "Identification of Aromas from Alcohols Using a Japanese-Lacquer-Film-Coated Quartz Resonator Gas Sensor in Conjunction with Pattern Recognition Analysis", Sensors and Actuators B, 35-36, pages 183-186, 1996.

[45] Saitoh A., Muñoz S. and Moriizumi T., "Characterisation of QCM Odor Sensors Coated with LB Films", Proceedings of the Ninth International Conference on Solid-State Sensors and Actuators, Transducers'97, pages 1351-1354, 1997.

[46] Di Natale C., Macagnano A., Paolesse R., Tarizzo E., D'Amico A., Davide F., Boschi

T., Faccio M., Ferri G., Sinesio F., Bucarelli F. M., Moneta E. and Quaglia G. B., "A Comparison Between an Electronic Nose and Human Olfaction in a Selected Case Study", Proceedings of the Ninth International Conference on Solid-State Sensors and Actuators, Transducers'97, pages 1335-1338, 1997.

[47] Yang M. and Thompson M., "Multiple Chemical Information from the Thickness Shear Mode Acoustic Wave Sensor in the Liquid Phase", Analytical Chemistry, Vol. 65, pages 1158-1168, 1993.

[48] Barnes C., "Development of Quartz Crystal Oscillators for Under-Liquid Sensing", Sensors and Actuators A, Vol. 29, pages 56-69, 1991.

[49] Martin S. J., Cernosek R. W. and Spates J.J., "Sensing Liquid Properties with Shear-Mode Resonator Sensors", Transducers'95-Eurosensors IX, pages 755-757, 1995.

[50] Muramatsu H., Tamiya E. and Karube I., "Computation of Equivalent Circuit Parameters of Quartz Crystal in Contact with Liquids and Study of Liquids Properties", Analytical Chemistry, Vol. 60, pages 2142-2146, 1988.

[51] Ghourchian H.O. and Kamo N., "New Detection Cell for Piezoelectric Quartz Crystals: Frequency Changes Strictly Follow Bruckenstein and Shay's Equation in Very Dilute Non-electrolyte Aqueous Solutions", Analyst, Vol. 120, pages 2737-2740, 1995.

[52] Zhou R., Haimbodi M., Everhart D. and Josse F., "Polymer-coated QCR Sensors for the Detection of Organic Solvents in Water", Sensors and Actuators B, 35-36, pages 176-182, 1996.

[53] Bruckenstein S., Michalski M., Fensore A., Li Z. and Hillman A. R., "Dual Quartz Crystal Microbalance Oscillator Circuit. Minimizing Effects due to Liquid Viscosity, Density and Temperature", Analytical Chemistry, Vol. 66, pages 1847-1852, 1994.

[54] Hammond J. M., Lec R. M., Libby D. G., Zhang X. J. and Prager L. A., "An Acoustic Automotive Engine Oil Quality Sensor", Proceedings of the Ninth International Conference on Solid-State Sensors and Actuators, Transducers'97, pages 1343-1346, 1997.

[55] Lucklum R., Behling C., Hauptmann P., Cernosek R.W. and Martin S.J., "Error Analysis of Quartz Crystal Resonator Applications", Proceedings of the Ninth International Conference on Solid-State Sensors and Actuators, Transducers'97, pages 1347-1350, 1997.

[56] Maupas H., Saby C., Jaffrezic-Renault N., Martelet C., Gabrielli C. and Perrot H., "Direct Detection of Antibody-Antigen Interactions with Gravimetric Measurements: Example of α-Fetoprotein Immunosystem", Proceedings of the Fifth International Meeting on Chemical Sensors, pages 213-216, 1994.

[57] Thompson M., Arthur C. L. and Dhaliwal G. K., "Liquid-Phase Piezoelectric and Acoustic Transmission Studies of Interfacial Immunochemistry", Analytical Chemistry, Vol. 58, pages 1206-1209, 1986.

[58] Rickert J., Weiss T. and Göpel W., "Self-Assembled Monolayers for Chemical Sensors: Molecular Recognition by Immobilised Supramolecular Structures", Sensors and Actuators B, 31, pages 45-50, 1996.

[59] Tessier L., Patat F., Schmitt N., Lethiecq M., Frangin Y. and Guilloteau D., "Significance of Mass and Viscous Loads Discrimination for an AT-Quartz Blood Group Immunosensor", Sensors and Actuators B, 18-19, pages 698-703, 1994.

[60] Kößlinger C., Uttenthaler E., Drost S., Aberl F., Wolf H., Brink G., Stanglmaier A. and Sackmann E., "Comparison of the QCM and the SPR Method for Surface Studies and Immunological Applications", Sensors and Actuators B, 24-25, pages 107-112, 1995.

[61] Rickert J., Weiss T., Kraas W., Jung G. and Göpel W., "A New Affinity Biosensor: Self-Assembled Thiols as Selective Monolayer Coatings of Quartz Microbalances", Transducers'95-Eurosensors IX, pages 528-531, 1995.

[62] Muramatsu H., Kajiwara K., Tamiya E. and Karube I., "Piezoelectric Immuno Sensor for the Detection of Candida albicans Microbes", Analytica Chemica Acta, 188, pages 257-261, 1986.

[63] Calabrese G., Wohltjen H. and Roy M. K., "Surface Acoustic Wave Devices as

Chemical Sensors in Liquids. Evidence Disputing the Importance of Rayleigh Wave Attenuation", Analytical Chemistry, Vol. 59, pages 833-837, 1987.

[64] McCallum J.J., "Piezoelectric Devices for Mass and Chemical Measurements: An Update", Analyst, Vol. 114, pages 1173-1189, 1989.

[65] Ballantine Jr. D. S. and Wohltjen H., "Surface Acoustic Wave Devices for Chemical Analysis", Analytical Chemistry, Vol. 61, No. 11, pages 704A-712A, 1989.

[66] Grate J. W., Martin S. J. and White R. M., "Acoustic Wave Microsensors - Part II", Analytical Chemistry, Vol.65, No.22, pages 987A-996A, 1993.

[67] Khlebarov Z. P., Stoyanova A. I. and Topalova.D. I., "Surface Acoustic Wave Sensors", Sensors and Actuators, Vol. 8B, pages 33-40, 1992.

[68] D'Amico A. and Verona E., "SAW Sensors", Sensors and Actuators, Vol. 17, pages 55-66, 1989.

[69] Atashbar M. Z. and Wlodarski W., "Design, Simulation and Fabrication of Doped TiO_2-Coated Surface Acoustic Wave Oxygen Sensor", Journal of Intelligent Material Systems and Structures, Vol. 8, pages 953-959, 1997.

[70] Varadan V. V., Roh Y. R. and Varadan V. K., "Local/Global SAW Sensors for Turbulence", Proceedings of the IEEE Ultrasonics Symposium, pages 591-594, 1989.

[71] Kondoh J. and Shiokawa S., "Liquid Identification Using SH-SAW Sensors", Transducers'95-Eurosensors IX, pages 716-719, 1995.

[72] Kondoh J. and Shiokawa S., "A Liquid Sensor Based on a Shear Horizontal SAW Device", Electronics and Communications in Japan, Part 2, Vol. 76, No. 2, pages 69-82, 1993.

[73] Campitelli A. P., Wlodarski W. and Hoummady M., "Identification of Natural Spring Water Using Shear Horizontal SAW based Sensors", Sensors and Actuators B., Vol. 49, No. 3, pages 195-201, 1998.

[74] Ricco A. J. and Martin S. J., "Acoustic Wave Viscosity Sensor", Applied Physics Letters, Vol. 50, No. 21, pages 1474-1476, 1987.

[75] Hummady M. and Bastien F., "Acoustic Wave Viscometer", Review of Scientific Instruments, Vol. 62, No. 8, pages 1999-2003, 1991.

[76] Josse F., Shana Z. A., Haworth D. T., Liew S. and Grunze M., "On the use of ZX-$LiNbO_3$ Acoustic Plate Mode Devices as Detectors for Dilute Electrolytes", Sensors and Actuators B, Vol. 9, pages 97-112, 1992.

[77] Gardner J. W., Varadan V. K. and Awadelkarim O. O., "Micro Sensors, MEMS and Smart Devices", John Wiley & Sons, England, 2001.

[78] Hummady M., Hauden D. and Bastien F., "Shear Horizontal Waves Sensors for Analysis of Physical Parameters of Liquids and Their Mixtures", Proceedings of the IEEE Ultrasonics Symposium, pages 303-306, 1991.

[79] Ricco A. J., Martin S. J., Frye G. C. and Niemczyk T. M., "Acoustic Plate Mode Devices as Liquid Phase Sensors", Proceedings of the IEEE Ultrasonics Symposium, pages 23-26, 1988.

[80] Sawaguchi A. and Toda K., "Liquid Viscosity Measurement Using SH Wave Propagation Characteristics on Piezoelectric Ceramic Thin Plate", Japanese Journal of Applied Physics, Vol. 31, Part 1, No. 9B, pages 3094-3097, 1992.

[81] Josse F. and Shana Z., "Acoustoionic Interaction of SH Surface Waves with Dilute Ionic Solutions", IEEE Transactions on Ultrasonics, Ferroelectrics and Frequency Control, Vol. 38, No. 3, pages 297-304, 1991.

[82] Dahint R., Shana Z.A., Josse F., Riedel S.A. and Grunze M., "Identification of Metal Ion Solutions Using Acoustic Plate Mode Devices and Pattern Recognition", IEEE Transactions on Ultrasonics, Ferroelectrics and Frequency Control, Vol. 40, No.2, pages 114-120, 1993.

[83] Andle J. C., Weaver J. T., Vetelino J. F. and McAllister D. J., "Application of Unidirectional Transducers in Acoustic Plate Mode Biosensors", Proceedings of the IEEE Ultrasonics Symposium, pages 331-335, 1993.

[84] Andle J. C., Weaver J. T., Vetelino J. F. and McAllister D. J., "Selective Acoustic Plate

Mode DNA Sensor", Sensors and Actuators B, 24-25, pages 129-133, 1995.

[85] Déjous C., Savart M., Rebière D. and Pistré J., "A Shear-Horizontal Acoustic Plate Mode (SH-APM) Sensor for Biological Media", Sensors and Actuators B, 26-27, pages 452-456, 1995.

[86] Andle J. C., Weaver J. T., McAllister D. J., Josse F. and Vetelino J. F., "Improved Acoustic-Plate-Mode Biosensor", Sensors and Actuators B, 13-14, pages 437-442, 1993.

[87] Schweyer M. G., Andle J. C., McAllister D. J. and Vetelino J. F., "An Acoustic Plate Mode Sensor for Acquous Mercury", Sensors and Actuators B, 35-36, pages 170-175, 1996.

[88] Lucklum R., Rösler S., Hartmann J. and Hauptmann P., "On-line Detection of Organic Pollutants in Water by Thickness Shear Mode Resonators", Sensors and Actuators B, 35-36, pages 103-111, 1996.

[89] Vellekoop M. J., Lubking G. W., Sarro P. M. and Venema A., "A Multi-Purpose Smart Acoustic Lamb Wave Sensor System", Proceedings of the Seventh International Conference on Solid-State Sensors and Actuators, Transducers'93, pages 1052-1055, 1993.

[90] Wu J. and Zhu Z., "Sensitivity of Lamb Wave Sensors in Liquid Sensing", IEEE Transactions on Ultrasonics, Ferroelectrics and Frequency Control, Vol. 43, No. 1, pages 71-72, 1996.

[91] Wenzel S. W. and White R. M., "Flexural Plate-Wave Sensor: Chemical Vapor Sensing and Electrostrictive Excitation", Proceedings of the IEEE Ultrasonics Symposium, pages 595-598, 1989.

[92] Grate J. W., Wenzel S. W. and White R. M., "Flexural Plate Wave Devices for Chemical Analysis", Analytical Chemistry, Vol. 63, pages 1552-1561, 1991.

[93] Tirole N., Choujaa A., Hauden D., Martin G., Blind P., Froelicher M., Pommier J. C. and Cachard A., "Lamb Waves Pressure Sensor Using an AlN/Si Structure", Proceedings of the IEEE Ultrasonics Symposium, pages 371-374, 1993.

[94] Choujaa A., Tirole N., Bonjour C., Martin G., Hauden D., Blind P., Cachard A. and Pommier C., "AlN/Silicon Lamb-Wave Microsensors for Pressure and Gravimetric Measurements", Sensors and Actuators A, pages 179-182, 1995.

[95] Martin S. J., Butler M. A., Spates J. J., Schubert W. K. and Mitchell M. A., "Magnetically-Excited Flexural Plate Wave Resonator", IEEE International Frequency Control Symposium, pages 25-31, 1997.

[96] Vellekoop M. J., Lubking G. W., Sarro P. M. and Venema A., "Integrated-Circuit Compatible Design and Technology of Acoustic-Wave Based Microsensor", Sensors and Actuators A, Vol. 44, pages 249-263, 1994.

[97] Andle J. C. and Vetelino J. F., "Acoustic Wave Biosensors", Sensors and Actuators A, Vol. 44, pages 167-176, 1995.

[98] Wang A. W., Kiwan R., White R. M. and Ceriani R. L., "A Silicon-Based Ultrasonic Immunoassay for Detection of Breast Cancer Antigens", Proceedings of the Ninth International Conference on Solid-State Sensors and Actuators, Transducers'97, pages 191-194, 1997.

[99] Kalantar-zadeh K., Trinchi A., Wlodarski W., Holland A., Atashbar M.Z., "A Novel SAW Love Mode Device with Nanocrystalline ZnO Film for Gas Sensing Applications", IEEE-NANO 2001, Hawaii, Oct. 28^{th}-30^{th}, pp. 556-561, 2001.

[100] Kalantar-Zadeh K., Wlodarski W., Chen Y. Y., Fry B. N. and Galatsis K., "Novel Love Mode surface acoustic wave based immunosensors", Sensors and Actuators B, Vol. 91, pages 143-147, 2003.

[101] Kalantar-Zadeh K., Trinchi A., Wlodarski W. and Holland A., "A Novel Love-Mode Device based on a ZnO/ST-cut Quartz Crystal Structure for Sensing Applications", Sensors and Actuators A, Vol. 100, pages 135-143, 2002.

[102] Bender F., Cernosek R. W. and Josse F., "Love-Wave Biosensors using Cross-Linked Polymer Waveguide on $LiTaO_3$ Substrates", Electronics Letters, Vol. 36, No. 19, 2000.

[103] Haueis R., Vellekoop M. J., Kovacs G., Lubking G. W. and Venema A., "A Love-

Wave Based Oscillator for Sensing in Liquids", Proceedings of the Fifth International Meeting of Chemical Sensors, Vol. 1, pages 126-129, 1994.

[104] Gizeli E., Goddard N. J., Lowe C. R. and Stevenson A. C., "A Love Plate Biosensor Utilising a Polymer Layer", Sensors and Actuators A, Vol. 6, pages 131-137, 1992.

[105] Kovacs G., Vellekoop M. J., Lubking G. W. and Venema A., "A Love Wave Sensor for (Bio)chemical Sensing in Liquids." Proceedings of the Seventh International Conference on Solid-State Sensors and Actuators, pages 510-513, 1993.

[106] Du J., Harding G. L., Ogilvy J. A., Dencher P. R. and Lake M., "A Study of Love-Wave Acoustic Sensors", Sensors and Actuators A, Vol. 56, pages 211-219, 1996.

[107] Kovacs G. and Venema A., "Theoretical Comparison of Sensitivities of Acoustic Shear Wave Modes for (Bio)chemical Sensing in Liquids", Applied Physics Letters, Vol. 61, No. 6, pages 639-641, 1992.

[108] Ricco A. J., Martin S. J. and Zipperian T. E., "Surface Acoustic Wave Gas Sensors Based on Film Conductivity Changes", Sensors and Actuators, Vol. 8, pages 319-333, 1985.

[109] Banda P., Campitelli A., Lee S., Brennan F. and Wlodarski W., "Aspects of Electronic Design for SAW and QCM Based Sensors", Proceedings of the Fifth International Meeting on Chemical Sensors, pages 57-60, 1994.

[110] Hivert B., Hoummady M., Henrioud J. M. and Hauden D., "Feasibility of SAW Sensor Array Processing with Formal Neural-Networks", Sensors and Actuators B, 18-19, pages 645-648, 1994.

[111] Grate J. W., Rose-Pehrsson S. L., Venezky D. L., Klusty M. and Wohltjen H., "Smart Sensor System for Trace Organophosphorus and Organosulfur Vapor Detection employing a Temperature-Controlled Array of Surface Acoustic Wave Sensors, Automated Sample Preconcentration and Pattern Recognition", Analytical Chemistry, Vol. 65, pages 1868-1881, 1993.

[112] Davide F. A. M. and D'Amico A., "Pattern Recognition from Sensor Arrays:

Theoretical Considerations", Sensors and Actuators A, Vol. 32, pages 507-518, 1992.

[113] Hivert B., Hoummady M., Mielle P., Henrioud J. M. and Hauden D., "A Fast and Reproducible Method for Gas Sensor Screening to Flavour Compounds", Sensors and Actuators B, 26-27, pages 242-245, 1995.

[114] Di Natale C., Davide F. A. M. and D'Amico A.. "A Self-Organizing System for Pattern Classification: Time Varying Statistics and Sensor Drift Effects", Sensors and Actuators B, 26-27, pages 237-241, 1995.

[115] McAlernon P., Slater J. M., Lowthian P. and Appleton M., "Interpreting Signals from an Array of Non-Specific Piezoelectric Chemical Sensors", Analyst, Vol. 121, pages 743-748, 1996.

[116] Kavalov D. and Kalinin V., "Neural Network Surface Acoustic Wave RF Signal Processor for Digital Modulation Recognition", IEEE Transactions on Ultrasonics, Ferroelectrics and Frequency Control, Vol. 49, pages 1280-1290, 2002.

[117] Hoummady M., Campitelli A. and Wlodarski W., "Acoustic Wave sensors: design, sensing mechanisms and applications", Smart Materials and Structures, Vol. 6, pages 647-657, 1997.

[118] Hauden D., Jaillet G. and Coquerel R., "Temperature sensor using SAW delay line", Proceedings of the IEEE Ultrasonics Symposium, pages 148-151, 1981.

[119] Bao X. Q., Burkhard W., Varadan V. V. and Varadan V. K., "SAW temperature sensor and remote reading system", Proceedings of the IEEE Ultrasonics Symposium, pages 583-585, 1987.

[120] Puccio D., Malocha D. C., Gallagher D. and Hines J., "SAW sensors using Orthogonal Frequency coding", Proceedings of the 2004 IEEE International Frequency Control Symposium and Exposition, pages 307-310, 2004.

[121] Talbi A., Sarry F., Le Brizoual L., Elmazria O. and Alnot P., "Development of SAW pressure sensor using ZnO/Si structure", Proceedings of the 2004 IEEE International Frequency Control Symposium and Exposition, pages 566-570, 2004.

[122] Schimetta G., Dollinger F., Scholl G. and Weigel R., "Wireless Pressure and Temperature measurement using a SAW Hybrid sensor", Proceedings of the IEEE Ultrasonics Symposium, 2000.

[123] Vlassov Yu. N., Kozlov A. S., Pashchin N. S. and Yakovkin I. B., "Precision SAW Pressure Sensors", Proceedings of the IEEE International Frequency Control Symposium, pages 665-669, 1993.

[124] Buff W., Rusko M., Vandahl T., Goroll M. and Moller F., "A Differential Measurement SAW Device for Passive Remote Sensoring", Proceedings of the IEEE Ultrasonics Symposium, pages 343-346, 1996.

[125] Martin S. J., Ricco A. J., Niemczyk T. M. and Frye G. C., "Characterization of SH Acoustic Plate Mode Liquid Sensors", Sensors and Actuators, Vol. 20, No. 3, pages 253-268, 1989.

[126] White R. M. and Wenzel S. W., "Fluid Loading of a Lamb-Wave Sensor", Applied Physics Letters, Vol. 52, No. 20, page 1653, 1988.

[127] Schmidt F., Sczesny O., Reindl L. and Magori V., "Remote sensing of physical parameters by means of passive Surface Acoustic Wave Devices ("ID-Tag"), Proceedings of the Ultrasonics Symposium, pages 589-592, 1994.

[128] Buff W., Plath F., Schmeckebier O., Rusko M., Vandahl T., Luck H., Moller F. and Malocha D. C., "Remote sensor system using passive SAW sensors", Proceedings of the Ultrasonics Symposium, pages 585-588, 1994.

[129] Hausleitner Ch., Steindl R., Pohl A. and Seifert F., "Low cost radio interrogation systems for passive SAW sensors and transponders", Proceedings of the IEEE, pages 847-850, 2001.

[130] B. J. Bazuin, M. Z. Atashbar and S. Krishnamurthy, "A Prototype Burst Transceiver for Smart SAW Sensors", Proceedings of the IEEE/EIT Conference, Indianapolis, Indiana, June 5-6, 2003.

[131] Ludwig R. and Bretchko P., "RF Circuit Design: Theory and Applications", Prentice

Hall Inc., Upper Saddle River, New Jersey.

[132] Van Valkenburg M. E., "Analog Filter Design", Oxford University Press, June 1995.

[133] Campbell C. K., "Surface acoustic wave devices for mobile and wireless communications", Elsevier Science, USA, 1998.

[134] Cross P. S., "Properties of reflective arrays for Surface Acoustic resonators", IEEE Transactions on Sonics and Ultrasonics, Vol. SU-23, No. 4, pages 255-262, 1976.

[135] CoventorWare Documentation, "CoventorWare designer reference Version 2006".

[136] Auld B. A., "Acoustic fields and waves in solids", Vol. I, Krieger Publishing Company, Florida, 1973.

[137] Xu G., "Direct finite-element analysis of the frequency response of a Y-Z lithium niobate SAW filter", Smart Materials and Structures, Vol. 9, pages 973-980, 2000.

[138] Campbell C. K., "Surface acoustic wave devices for mobile and wireless communications", Elsevier Science, USA, 1998.

[139] Tung H. –Y. and Ro R., "Frequency responses of Surface-Acoustic-Wave Filters with two-track slanted finger interdigital transducers", Japanese journal of Applied Physics, Vol. 44, No. 6A, pages 4025-4031, 2005.

[140] Ro R., Tung H. –Y. and Wu S. –J., "Design of two-track Surface Acoustic Wave Filters with Width-controlled reflectors", Japanese journal of Applied Physics, Vol. 43, No. 2, pages 688-694, 2004.

[141] Moulic J. R., "A broadband surface-wave filter with -50 dB stopbands and 1-dB passband ripple", Proceedings of the Ultrasonics Symposium, pages 673-674, 1977.

[142] Bhattacharya A. B., Tuli S. and Majumdar S., "SPICE simulation of Surface Acoustic Wave Interdigital Transducers", IEEE Transactions on Ultrasonics, Ferroelectrics and Frequency Control, Vol. 42, No. 4, pages 784-786, 1995.

[143] Smith W. R., Gerard H. M. and Jones W. R., "Analysis and Design of Dispersive Interdigital Surface-Wave Transducers", IEEE Transactions on Microwave Theory and Techniques, Vol. MTT-20, No. 7, pages 458-471, 1972.

[144] Ryder J. D., "Networks, Lines and Fields", Asia Publishing House, pages 80-88, 1964.